

# **PEMFC performance improvement through oxygen starvation prevention, modeling, and diagnosis of hydrogen leakage**

by

**Sasan Ebrahimi**

M.Sc., Sharif University of Technology, 2013  
B.Sc., University of Tehran, 2011

Thesis Submitted in Partial Fulfillment of the  
Requirements for the Degree of  
Doctor of Philosophy

in the

School of Mechatronic Systems Engineering  
Faculty of Applied Sciences

© Sasan Ebrahimi 2020

SIMON FRASER UNIVERSITY

Fall 2020

Copyright in this work rests with the author. Please ensure that any reproduction or re-use is done in accordance with the relevant national copyright legislation.

## Declaration of Committee

**Name:** Sasan Ebrahimi

**Degree:** Doctor of Philosophy

**Thesis Title:** PEMFC performance improvement through oxygen starvation prevention, modeling, and diagnosis of hydrogen leakage

**Examining Committee:**

**Chair:** Ramtin Rakhsha  
Lecturer, Mechatronic Systems Engineering

**Krishna Vijayaraghavan**  
Supervisor  
Associate Professor, Mechatronic Systems Engineering

**Michael Eikerling**  
Committee Member  
Professor, Chemistry

**Flavio Firmani**  
Committee Member  
Senior lecturer, Mechatronic Systems Engineering

**Jiacheng (Jason) Wang**  
Examiner  
Associate Professor, Mechatronic Systems Engineering

**Mina Hoorfar**  
External Examiner  
Professor  
School of Engineering  
University of British Columbia

## Abstract

Catalyst degradation results in emerging pinholes in Proton Exchange Membrane Fuel Cells (PEMFCs) and subsequently hydrogen leakage. Oxygen starvation resulting from hydrogen leaks is one of the primary life-limiting factors in PEMFCs. Voltage reduces, and the cell performance deteriorates. Starved PEMFCs also work as a hydrogen pump, increasing the amount of hydrogen on the cathode side, resulting in hydrogen emissions. Therefore, it is important to delay the occurrence of oxygen starvation while simultaneously be able to diagnose the hydrogen crossover through the pinholes. In this work, first, we focus on catalyst configuration as a novel method to prevent oxygen starvation. It is hypothesized that the redistribution of the platinum catalyst can increase the maximum current density and prevent oxygen starvation and catalyst degradation. A multi-objective optimization problem is defined to maximize fuel cell efficiency and to prevent oxygen starvation in the PEMFC. Results indicate that the maximum current density rises about eight percent, while the maximum PEMFC power density increases by twelve percent. In the next step, a previously developed pseudo two-dimensional model is used to simulate fuel cell behavior in the normal and the starvation mode. This model is developed further to capture the effect of the hydrogen pumping and to measure the amount of hydrogen in the outlet of the cathode channel. The results obtained from the model are compared with the experimental data, and validation shows that the proposed model is fast and precise. Next, Machine Learning (ML) estimators are used to first detect whether there is a hydrogen crossover in the fuel cell and second to capture the amount of hydrogen cross over. K Nearest Neighbour (KNN) and Artificial Neural Network (ANN) estimators are chosen for leakage detection and classification. Eventually, a pair of ANN classifier-regressor is chosen to first isolate leaky PEMFCs and then quantify the amount of leakage. The classifier and regressor are both trained on the datasets that are generated by the pseudo two-dimensional model. This ML diagnosis algorithm can be employed as an onboard diagnosis system that can be used to detect and possibly prevent cell reversal failures.

**Keywords:** Oxygen starvation, hydrogen pumping, diagnosis, leakage detection, leakage quantification, classifier and regressor, ANN, KNN

## Dedication

*To my love Elly, my dear parents,  
and my brothers for their  
unconditional support, love, and  
encouragement. I love you more  
than anything in the world*

## Acknowledgements

I would like to express my gratitude towards all the amazing people who made accomplishing this dissertation possible and enjoyable for me. My special thanks go to my senior supervisor at Simon Fraser University (SFU), Dr. Vijayaraghavan, for his great support and guidance throughout my Ph.D. studies. I am also very grateful to my colleagues and friends at the “Advance nonlinear control laboratory for clean energy technology”.

I would like to thank my committee members, Dr. Eikerling and Dr. Firmani, for their valuable comments and suggestions on my candidacy report and their guidance on the final thesis draft. I would also like to thank my examiners, Dr. Hoorfar and Dr. Wang, for evaluating my thesis and providing me with their valuable comments.

I would like to thank Ballard corporation for providing us with experimental data and technical information. I would like to thank our co-op students at SFU: Wes Romey and Harnit Singh Sudan, for assisting me in the dataset generation of the machine learning part of this work.

Finally, I would like to express my gratitude to my parents, who always supported me in all stages of my personal life and professional career, and to my lovely wife (Elly), who always believed in me and supported me with her love and encouragement. I would like to thank my brothers, Dr. Khosrow Ebrahimi and Dr. Khashayar Ebrahimi, for their mentorship and endless support.

# Table of Contents

Declaration of Committee .....	ii
Abstract.....	iii
Dedication .....	v
Acknowledgements .....	vi
Table of Contents.....	vii
List of Tables.....	ix
List of Figures.....	x
List of Acronyms.....	xiii
List of Parameters .....	xv
<b>Chapter 1. Introduction .....</b>	<b>1</b>
1.1. Basic of PEMFCs .....	6
1.2. Leaky PEMFCs and Hydrogen Pumping .....	9
1.3. Objectives.....	11
1.4. Research Roadmap.....	12
1.5. Scholarly Contributions.....	14
1.5.1. Contributions Related to Thesis .....	14
1.5.2. Other Contributions .....	14
<b>Chapter 2. Literature Review .....</b>	<b>16</b>
2.1. PEMFC Modeling Approaches.....	16
2.2. Oxygen Starvation .....	17
2.3. Non-uniform Catalyst Distribution .....	24
2.4. Leakage Diagnosis in PEMFC .....	25
2.5. Gap in Literature.....	31
2.6. Research Motivation.....	33
<b>Chapter 3. Optimal Catalyst Distribution as a Method to Enhance Performance and Durability .....</b>	<b>34</b>
3.1. Mathematical Modeling.....	34
3.1.1. Governing Equations .....	36
3.1.2. Boundary Conditions: .....	43
3.1.3. Numerical Approach .....	45
3.1.4. Model Validation and Grid Independency .....	47
3.2. Catalyst Distribution Modeling .....	50
3.3. Effect of Non-Uniform Catalyst Distribution.....	52
3.4. Optimization of Catalyst Distribution .....	57
3.5. Chapter Summary .....	65
<b>Chapter 4. Developing a Base Model for Leakage Diagnosis .....</b>	<b>66</b>
4.1. Mathematical Model .....	66
4.1.1. Effective Reactant Concentration at CCL and ACL .....	68
4.1.2. Governing Equations for PEMFC in Driving Mode [15] .....	73

4.1.3.	Governing Equations for PEMFC in the Driven Mode [15] .....	74
4.1.4.	Species Concentration Along the CCH .....	76
4.2.	Numerical Algorithm .....	78
4.3.	Model Validation .....	81
4.4.	Experimental Observations of Oxygen Starvation and Comparisons with Model .....	83
4.4.1.	Steady-State Model Validation for a Leak in a Single Cell of the First Commercial Fuel Cell Stack, a 9-Cell Short Stack .....	84
4.4.2.	Transient Model Validation for a Leak in a Single Cell of the First Commercial Fuel Cell Stack, a 9-Cell Short Stack .....	88
4.4.3.	Steady-State Model Validation for a Leak in the Entire Stack of a Second Commercial Fuel Cell Stack, a 10-Cell Short Stack .....	89
4.4.4.	Test on a Real MEA Transfer Leak in the Second Commercial Fuel Cell Stack Model .....	91
4.4.5.	Starvation Point Determination on a Third Commercial Fuel Cell Stack .....	92
4.5.	Chapter Conclusion .....	93
<b>Chapter 5.</b>	<b>Leakage Diagnosis and Quantification .....</b>	<b>96</b>
5.1.	Approach Principle .....	97
5.2.	Dataset Generation in Steady-State .....	98
5.3.	Preprocessing and Data Cleaning in Steady-State .....	102
5.4.	Training/Testing Process in Steady-State .....	103
5.4.1.	Classification (Leakage Detection) .....	104
5.4.2.	Regression (Leakage Quantification) .....	110
5.4.3.	Leakage Detection and Quantification Case Study .....	114
5.4.4.	Hydrogen Pumping Prediction .....	116
5.5.	Chapter Summary .....	117
<b>Chapter 6.</b>	<b>Conclusion and Future Work .....</b>	<b>119</b>
6.1.	Part One: Non-Uniform Catalyst Distribution .....	119
6.2.	Part Two: Pseudo Two-Dimensional Modeling of a PEMFC .....	120
6.3.	Part Three: Leakage Diagnosis, Quantification, and Hydrogen Pumping Prediction in Steady-State .....	121
<b>References</b> .....		<b>123</b>
<b>Appendix A. SIMPLE Method and Hybrid Scheme</b> .....		<b>131</b>
<b>Appendix B. GA Algorithm</b> .....		<b>140</b>
<b>Appendix C. KNN Estimator</b> .....		<b>142</b>
<b>Appendix D. ANN Estimator</b> .....		<b>144</b>
<b>Appendix E. Classifier and Regressor Performance Indexes</b> .....		<b>151</b>



## List of Tables

Table 1-1. Fuel cell categories [6].....	3
Table 1-2. PEMFC components [7] .....	7
Table 2-1. Reactant starvation reactions .....	18
Table 2-2. Literature on hydrogen starvation .....	19
Table 2-3. Literature review on oxygen starvation .....	21
Table 2-4. An investigation of non-model based fault diagnosis models [53] .....	28
Table 3-1. Mixture properties equations, k denotes liquid and gas phases [67,71,73,74] .....	39
Table 3-2. Supporting equations for the two-dimensional, two-phase cathode model....	47
Table 3-3. The grid independence test .....	49
Table 3-4. Optimization algorithm parameters .....	59
Table 3-5. Optimal catalyst distribution functions and improvement percentages .....	61
Table 4-1. Model parameters [68].....	81
Table 4-2. Experimental steady-state tests parameters for hydrogen injection in just one cell .....	84
Table 4-3. Experimental steady-state tests parameters for hydrogen injection in the whole stack .....	89
Table 5-1. Range of different features used for generating the basic dataset .....	99
Table 5-2. Sample of scaled data .....	102
Table 5-3. Performance indexes for KNN classifier .....	105
Table 5-4. Performance indexes for ANN classifier .....	110
Table 5-5. Performance indexes for KNN regressor .....	112
Table 5-6. Performance indexes for ANN regressor .....	114

## List of Figures

Figure 1-1. Cumulative emissions of CO <sub>2</sub> projection [3].....	2
Figure 1-2. PEMFC projection cost [9].....	4
Figure 1-3. Fuel cell schematic.....	6
Figure 1-4. Different losses on the polarization curve.....	9
Figure 1-5. Schematic of a leaky PEMFC in hydrogen pumping mode.....	11
Figure 1-6. Thesis roadmap.....	13
Figure 2-1. PEMFC failure diagnosis approaches.....	26
Figure 2-2. General algorithm of combined fault diagnosis approach.....	29
Figure 3-1. Numerical domain.....	35
Figure 3-2. Numerical algorithm.....	46
Figure 3-3. Validation of the two-phase model.....	48
Figure 3-4. Effect of mesh size on current density distribution at the CGDL/CCL interface at $\eta=0.33\text{ V}$ .....	49
Figure 3-5. Oxygen mass fraction distribution for uniform catalyst distribution at $\eta=0.33\text{ V}$ .....	52
Figure 3-6. Oxygen mass fraction distribution for non-uniform catalyst distribution at $\eta=0.33\text{ V}$ .....	53
Figure 3-7. Comparison of oxygen distributions at CCL for two cases of catalyst distributions ( $\eta = 0.33\text{ V}$ ).....	54
Figure 3-8. Current density distributions at CCL for two cases of catalyst distributions ( $\eta = 0.33\text{ V}$ ).....	54
Figure 3-9. current density distributions Comparison between two cases of catalyst distributions ( $\eta = 0.33\text{ V}$ ).....	55
Figure 3-10. Temperature distributions Comparison between two cases of catalyst distributions ( $\eta = 0.33\text{ V}$ ).....	56
Figure 3-11. Optimization procedure to find the optimal catalyst distribution.....	58
Figure 3-12. Optimal catalyst distributions.....	62
Figure 3-13. Comparison of current distribution between uniform and optimal catalyst distributions at $\eta = 0.33\text{ V}$ .....	63
Figure 3-14. Comparison of oxygen mass fraction distributions between uniform and optimal catalyst distributions at $\eta = 0.33\text{ V}$ .....	63
Figure 3-15. Comparison between polarization curves between uniform and optimal catalyst distribution cases.....	64
Figure 3-16. Comparison between polarization curves between uniform and optimal catalyst distribution cases.....	64
Figure 4-1. Numerical domain of the pseudo two-dimensional model developed for diagnosis purposes.....	67
Figure 4-2. Mesh type used the pseudo, two-dimensional model developed for diagnosis purposes.....	79

Figure 4-3. Numerical algorithm of the pseudo, two-dimensional model developed for diagnosis purposes .....	80
Figure 4-4. Validation of pseudo, two-dimensional model based on the polarization curve .....	82
Figure 4-5. Validation of pseudo, two-dimensional models based on the transient response to a step-change in current from 5 A to 10 A.....	82
Figure 4-6. Schematic of the setup used for testing first commercial fuel cell stack, a 9-cell short stack .....	85
Figure 4-7. Voltage and hydrogen emission versus hydrogen injection at 10 A in a leaky single cell of 9-cell short stack.....	86
Figure 4-8. Voltage and hydrogen emission versus hydrogen injection at 20 A in a leaky single cell of 9-cell short stack.....	86
Figure 4-9. Hydrogen emission versus hydrogen leak rate at 10 A.....	87
Figure 4-10. Hydrogen emission versus hydrogen leak rate at 20 A.....	87
Figure 4-11. Hydrogen pumping triggering leak at different currents in the entire stack of the 10-cell short stack .....	88
Figure 4-12. Transient model validation for a sudden increase in a leak in a single cell of a 9-cell short stack. ....	89
Figure 4-13. Schematic of the setup used for testing first commercial fuel cell stack, a 9-cell short stack .....	90
Figure 4-14. Voltage and hydrogen emission response under hydrogen injection at 6.73 slm airflow and 0 A for a leak in the entire stack of the 10-cell short stack .....	90
Figure 4-15. Voltage and hydrogen emission response under hydrogen injection at 6.73 slm airflow and 8 A for a leak in the entire stack of the 10-cell short stack .....	91
Figure 4-16. Voltage and hydrogen emission response hydrogen injection at 60 slm airflow and 0 A for a leak in the entire stack of the 10-cell short stack ....	91
Figure 4-17. Actual hydrogen transfer leak test simulated by different differential pressure.....	92
Figure 4-18. Full starvation model results on the third commercial fuel cell stack .....	93
Figure 5-1. ML types [81] .....	97
Figure 5-2. Diagnosis methodology [81] .....	98
Figure 5-3. Dataset formation for ML estimators.....	100
Figure 5-4. Leakage detection quantification, and hydrogen pumping prediction roadmap in steady-state.....	101
Figure 5-5. Cross-validation scheme .....	104
Figure 5-6. Confusion matrix for KNN classifier .....	105
Figure 5-7. Learning curve for KNN classifier .....	106
Figure 5-8. Neural network schematic .....	107
Figure 5-9. Accuracy of ANN classifier based on the number of neurons in each hidden layer .....	107
Figure 5-10. ANN classification metric plots .....	109

Figure 5-11. Confusion matrix for ANN classifier .....	110
Figure 5-12. Learning curve for KNN regressor .....	111
Figure 5-13. MSE of ANN regressor based on the number of neurons in each layer for leakage quantification .....	112
Figure 5-14. Training and validation loss plots for ANN regressor .....	114
Figure 5-15. Customized leakage profile .....	115
Figure 5-16. Voltage response to the customized leakage pattern at $I = 10$ A .....	115
Figure 5-17. Comparison of the introduced leakage values and the predicted leakage values .....	116
Figure 5-18. Hydrogen pumping prediction algorithm .....	117

## List of Acronyms

ACH	Anode channel
ACL	Anode catalyst layer
AFC	Alkaline fuel cell
AGDL	Anode gas diffusion layer
ANN	Artificial neural network
CCH	Cathode channel
CCL	Cathode catalyst layer
CFD	Computational fluid dynamics
CGDL	Cathode gas diffusion layer
CL	Catalyst layer
CV	Cyclic voltammetry
DL	Double layer
DMFC	Direct methanol fuel cell
EIS	Electrochemical impedance spectroscopy
FR	Flow rate
FN	False negative
FP	False positive
GA	Genetic algorithm
GDL	Gas diffusion layer
KNN	K nearest neighbors
LSV	Load specific variations
MAE	Mean absolute error
MCFC	Molten carbonate fuel cell
MEA	Membrane electrode assembly
ML	Machine learning
MSE	Mean squared error
NSE	Navier-Stokes equations
ORR	Oxygen reduction reaction
PAFC	Phosphoric acid fuel cell
PC	Personal computer
PEM	Polymer electrolyte membrane
PEMFC	Polymer electrolyte membrane fuel cell

PFSA	Perfluorosulfonic acid
ReLU	Rectified linear unit
SEM	Scanning electron microscopy
SOFC	Solid oxide fuel cell
TDMA	Tridiagonal matrix algorithm
TN	True negative
TP	True positive

## List of Parameters

$a_s$	Total catalyst surface area per unit volume [ $\frac{1}{\text{cm}}$ ]
$a_0$	Total catalyst surface area per unit mass [ $\frac{\text{cm}^2}{\text{gr}}$ ]
$B_{\text{conc}}$	Effective concentration coefficient in Equation (4-37)
$C$	Species mass fraction
$C_{\text{DL}}$	Double-layer capacitance [F]
$D$	Diffusion coefficient [ $\frac{\text{cm}^2}{\text{s}}$ ]
$f_i, i = 0, 1, \dots, n$	Catalyst distribution function coefficients
$F$	Faraday constant [ $96493 \frac{\text{A}}{\text{s}}$ ]
$\text{FR}$	Volume flow rate [slm or sccm]
$\text{FR}_{\text{Cathode\_before\_injection}}$	Cathode volume flow rate before hydrogen injection [slm or sccm]
$\text{FR}_{\text{injected\_hydrogen}}$	Injected hydrogen volume flow rate [slm or sccm]
$G$	Gibbs free energy [J]
$h$	Enthalpy [ $\frac{\text{J}}{\text{kg}}$ ]
$h_{\text{fg}}$	Phase change enthalpy [ $\frac{\text{J}}{\text{kg}}$ ]
$h_p$	High pass filter
$h(\bar{x})$	Catalyst distribution function
$I$	Current [A]
$J$	Current density [ $\frac{\text{A}}{\text{cm}^2}$ ]
$J_{\text{lim}}$	Limiting current density [ $\frac{\text{A}}{\text{cm}^2}$ ]
$J_{\text{A}}^{\text{ref}}$	Anode exchange current density [ $\frac{\text{A}}{\text{cm}^2}$ ]
$J_{\text{C}}^{\text{ref}}$	Cathode exchange current density [ $\frac{\text{A}}{\text{cm}^2}$ ]
$J(s_1)$	Capillary pressure function
$\vec{j}$	Diffusive mass flux [ $\frac{\text{kg}}{\text{m}^2 \text{s}}$ ]
$J_{\text{Ract}}$	Current density through the resistive component

	of activation loss [ $\frac{A}{cm^2}$ ]
$\dot{m}_{fg}$	Mass rate of phase change [ $\frac{kg}{s}$ ]
$m_{pt}$	Platinum catalyst loading [ $\frac{mg}{cm^2}$ ]
$M$	Molecular weight [ $\frac{kg}{mol}$ ]
$n$	Number of electrons
$N_{ele}$	Number of elements along the flow direction in the pseudo two-dimensional model
$\dot{N}$	Molar flux rate [ $\frac{mol}{cm^2s}$ ] or mass flux rate [ $\frac{gr}{cm^2s}$ ]
$\dot{N}_{B,C}$	Molar flow rate of non-participating gas on cathode side [ $\frac{mol}{cm^2s}$ ]
$\dot{N}_{B,A}$	Molar flow rate of non-participating gas on anode side [ $\frac{mol}{cm^2s}$ ]
$\dot{N}_{air}^{inlet}$	Molar flow rate of air at the inlet on cathode side [ $\frac{mol}{cm^2s}$ ]
$\dot{N}_{H_2}^{inlet}$	Molar flow rate of hydrogen at the inlet on anode side [ $\frac{mol}{cm^2s}$ ]
$P$	Power density [ $\frac{W}{cm^2}$ ] or pressure [Pa]
$P_c$	Capillary pressure [Pa]
$P_{sat}$	Saturation pressure [Pa]
$q''$	Heat flux [ $\frac{J}{m^2s}$ ]
$\dot{q}$	Volumetric heat generation [ $\frac{J}{m^3s}$ ]
$R$	Universal gas constant [ $\frac{J}{mol\ K}$ ]
$R_{A-film}$	The magnitude of maximum oxygen concentration drop across water film in Equation (4-31)
$R_{B-film}$	The current scaling factor in the sigmoid function in Equation (4-31)
$R_{ohm}$	Ohmic resistance [ $\Omega\ cm^2$ ]
$s$	Phase saturation or Laplace variable



$T$	Temperature [K]
$t$	Time [s]
$\vec{u}$	Velocity vector [ $\frac{m}{s}$ ]
$u$	Horizontal component of velocity [ $\frac{m}{s}$ ]
$v$	Vertical component of velocity [ $\frac{m}{s}$ ]
$V$	Voltage [V]
$V_{oc}$	Open circuit voltage [V]
$w_1$	Constant activation overpotential term in Equation (4-40)
$w_2$	Temperature dependence activation overpotential coefficient in Equation (4-40)
$w_3$	Current density dependent activation overpotential coefficient in Equation (4-40)
$w_4$	Anode activation coefficient in Equation (4-48)
$x, y, z$	Cartesian coordinates [cm]
$\bar{x}$	Dimensionless length
$X$	Input array to the classifier/regressor
$y$	Real/true outcome array of classifier/regressor problem
$\hat{y}$	Outcome array estimated by classifier/regressor

#### Greek Symbols

$\alpha$	Charge transfer coefficient
$\alpha$	Water transport coefficient
$\rho$	Density [ $\frac{kg}{m^3}$ ]
$K$	Permeability [ $m^2$ ]
$K_r$	Relative permeability
$\mu$	Dynamic Viscosity [ $\frac{Ns}{m^2}$ ]
$\nu$	Kinematic viscosity [ $\frac{m^2}{s}$ ]
$V$	Volume [ $cm^3$ ]
$V_{pore}$	Pore volume [ $cm^3$ ]

$V_{\text{total}}$	Total volume [ $\text{cm}^3$ ]
$\lambda$	Individual mobility
$\varepsilon$	Porosity
$\tau$	Time constant [s]
$\phi_{\text{H}_2}$	Hydrogen concentration [ $\frac{\text{mol}}{\text{cm}^3}$ ]
$\phi_{\text{H}_2,\text{ACH}}$	Hydrogen concentration at anode channel [ $\frac{\text{mol}}{\text{cm}^3}$ ]
$\phi_{\text{H}_2,\text{ACL}}$	Hydrogen concentration at the anode catalyst layer [ $\frac{\text{mol}}{\text{cm}^3}$ ]
$\phi_{\text{O}_2}$	Oxygen concentration [ $\frac{\text{mol}}{\text{cm}^3}$ ]
$\phi_{\text{O}_2,\text{ACH}}$	Oxygen concentration at cathode channel [ $\frac{\text{mol}}{\text{cm}^3}$ ]
$\phi_{\text{O}_2,\text{ACL}}$	Oxygen concentration at the cathode catalyst layer [ $\frac{\text{mol}}{\text{cm}^3}$ ]
$\phi_{\text{Normal}}$	Normal oxygen concentration [ $\frac{\text{mol}}{\text{cm}^3}$ ]
$\phi_{\text{O}_2,\text{film}}$	Reduced oxygen concentration due to water film formation [ $\frac{\text{mol}}{\text{cm}^3}$ ]
$\chi$	Mole fraction of species
$\chi_{\text{H}_2,\text{leak}}$	Leakage mole fraction
$\eta$	Overpotential [V]
$\eta_{\text{ohm}}$	Ohmic overpotential [V]
$\eta_{\text{act}}$	Activation overpotential [V]
$\eta_{\text{act},0}$	Activation potential loss coefficient [V]
$\eta_{\text{act},\text{DL}}$	Activation overpotential across double-layer [V]
$\rho_{\text{I}}$	Current density dependent coefficient in ohmic resistance formula in Equation (4-38)
$\rho_0$	Constant term in ohmic resistance formula in Equation (4-38)
$\rho_{\text{T}}$	Temperature dependent coefficient in ohmic resistance formula in Equation (4-38)

## Subscripts and superscripts

A	Anode
C	Cathode
eff	Effective
g	Gas
l	Liquid
r	Relative
H <sub>2</sub>	Hydrogen
O <sub>2</sub>	Oxygen
N <sub>2</sub>	Nitrogen
H <sub>2</sub> O	Water
0	Reference or standard condition
req	Required
sat	Saturation

# Chapter 1.

## Introduction

Fuel Cells are energy conversion devices that convert chemical energy in the input fuels directly to electricity. Fuel cells are not restricted by Carnot efficiency and hence have higher efficiency compared to internal combustion engines [1]. Fuel cells have zero-emissions and are suitable for both portable and stationary applications [1]. Moving towards alternative energy technologies and specifically fuel cells has been accelerated within the last decades due to several reasons summarized as follows:

- Scarcity of fossil fuels: it is necessary to note that nearly seventy percent of today's electricity is produced through fossil fuel combustion technologies [2]. Thus, it is critical to lower our dependence on fossil fuels by moving towards renewable and novel energy technologies.
- Rise in pollution level: greenhouse gas emissions have been increasing dramatically within the last decades. For instance, the cumulative amount of CO<sub>2</sub>, which forms 84% of the total emissions has been increased from 50,000 million tonnes in 1940 to nearly 280,000 million tonnes in 2000 [3]. The projected trend for cumulative emissions of CO<sub>2</sub> is provided in Figure 1-1. This figure illustrates the steep growth of CO<sub>2</sub> exhaust. Utilizing fuel cells could reduce the major amount of pollutants by 90% since this technology potentially produces no exhaust [3].

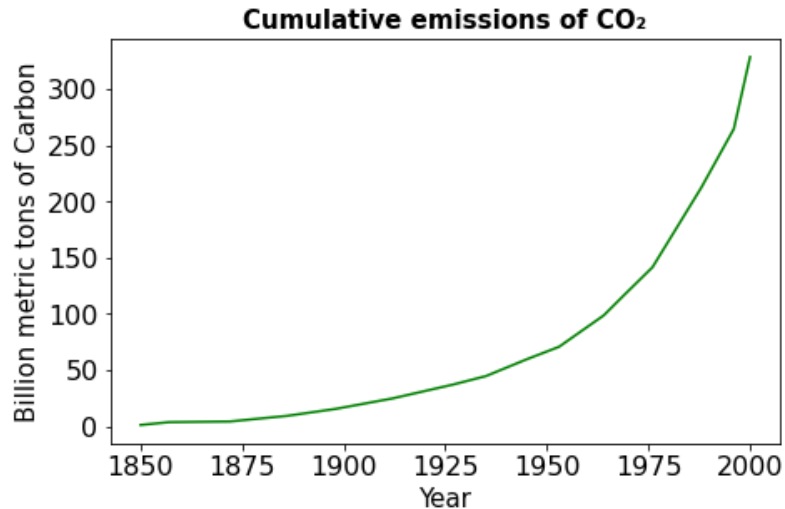


Figure 1-1. Cumulative emissions of CO<sub>2</sub> projection [3]

- Need for higher efficiency for economic advancement: Since there is no mechanical component involved in converting chemical energy to electricity, the efficiency of fuel cells is much higher than conventional internal combustion engines with an average of 20% efficiency [1,4].

Fuel cell has a multilayer structure with fuel and oxidizer stream into anode and cathode sides through flow channels. Reactants move and reach the catalyst layer surface at the interface of the electrode/membrane. At the Anode Catalyst Layer (ACL), fuel is oxidized and converts into ions and electrons. Membrane electrolyte is chosen to only allow the flow of ions. Ions move through the membrane and reach the Cathode Catalyst Layer (CCL), while electrons are transferred to CCL through an external circuit to provide the electric work. At the CCL, electrons, ions, and reactants participate in the reduction reaction and complete the cell reaction. The products of the complete cell reaction are electrical work, chemicals, and released heat [1,5].

Fuel cells are usually categorized based on the material used as an electrolyte and the operating temperature. These categories are summarized in Table 1-1.

Table 1-1. Fuel cell categories [6]

Fuel cell Types	Electrolyte	Operating Temperature
Alkaline Fuel Cell (AFC)	Potassium hydroxide solution	Room temperature to 90°C
Proton Exchange Membrane Fuel Cell (PEMFC)	Flexible solid perfluorosulfonic acid (PFSA) polymeric membrane	Room temperature to 80°C
Direct Methanol Fuel Cell (DMFC)	Solid, hydrated sheets of sulfonated fluoropolymers polymeric membrane	Room temperature to 130°C
Phosphoric Acid Fuel Cell (PAFC)	Solution of phosphoric acid in porous silicon carbide matrix	160°C – 220°C
Molten Carbonate Fuel Cell (MCFC)	Alkali metal (Li/K or Li/Na) carbonates in a porous ceramic matrix	620°C – 660°C
Solid Oxide Fuel Cell (SOFC)	Solid ceramic oxide electrolyte (Yttria (Y <sub>2</sub> O <sub>3</sub> ) stabilized zirconia (ZrO <sub>2</sub> ))	880°C – 1000°C

Among different types of fuel cells, Polymer Electrolyte Membrane fuel cells (PEMFCs) possess a compact and scalar design, work at low temperatures, and lack any corrosive fluids [7]. Therefore, PEMFCs are desirable for all automobile, transport, and stationary applications [2,7]. However, the high cost of ownership resulting from high initial cost and low durability has limited PEMFCs from becoming commercially viable alternatives. There have been significant efforts to reduce the price and increase the lifetime and durability of fuel cells. However, expectations have not been met yet [8]. Figure 1-2 shows the projection of a PEMFC cost from 2006 to 2020.

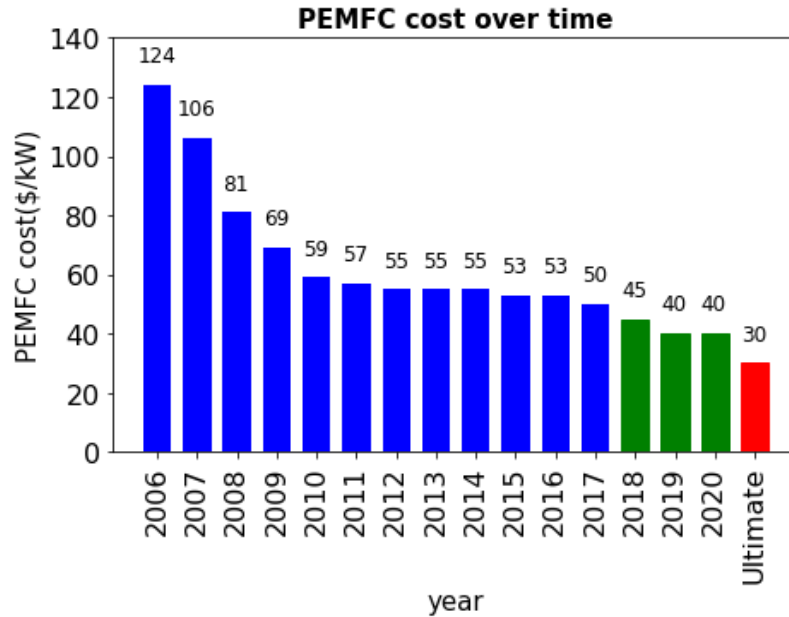


Figure 1-2. PEMFC projection cost [9]

Based on the data that was released by the Department of Energy (DOE) in 2017, the expected final price of the fuel cell for 2020 is \$40/kW [9], which used to be a target for 2017 [10]. The difference between these two prices emphasizes the development of novel methods to enhance PEMFC performance and to reduce the final cost per each kilowatt.

However, the final price is not the only issue with PEMFCs and an adequate lifetime is vital to commercialize PEMFCs in both stationary and mobile applications. For instance, a minimum of 40,000 and 5000 hours are required for residential and vehicle PEMFCs to make them viable options for these applications [11]. In practice, the actual lifetime of PEMFCs is not sufficient due to durability and degradation issues, including various types of faults [8]. These faults must be detected early and sometimes needed to be estimated and accommodated to ensure durability and efficient performance. Hence, to assure the safe operation of the PEMFC systems, it is necessary to use diagnosis techniques to detect and isolate faults. Leakage is one of the primary faults that reduces the operating voltage and accelerates MEA degradation. Hydrogen leaks rise as a result of local starvation, where platinum catalyst degrades. Pinhole and hydrogen leaks appear in the MEA, and hydrogen molecules cross over to the cathode side and consume available oxygen molecules. As a result, hydrogen leaks intensify oxygen starvation and could result in more pinholes and larger amounts of leakages. Furthermore, hydrogen leaks not only accelerate oxygen starvation in the cathode side but also can result in the generation of

hydrogen molecules in case of full oxygen starvation [12–15]. In this case, PEMFC works as a hydrogen pump and consumes power rather than producing it. As a result, voltage drops, and PEMFC performance deteriorates.

Thus, developing novel methods to enhance PEMFC efficiency, prevent oxygen starvation, and diagnosing the leakage is of importance. This work presents catalyst layer reconfiguration as a method to enhance PEMFC performance while delaying the inception of oxygen starvation. Redistribution of the catalyst could result in the higher maximum PEMFC power density with the same amount of platinum catalyst. This aspect of the catalyst reconfiguration would result in a lower cost per kilowatt and would accelerate the movement towards a \$30/kW price where PEMFC can compete with other energy technologies. The other purpose of catalyst reconfiguration is to provide more uniform reactant distribution at the catalyst layer, which would result in a delay in the inception of oxygen starvation and MEA degradation. This aspect of the catalyst reconfiguration would result in higher durability of PEMFCs. To prevent further MEA degradation, a combined model-based and non model-based diagnosis algorithm is developed to diagnose hydrogen leakage and quantify the amount of hydrogen leakage flow rate, which would result in higher durability of PEMFCs.



## 1.1. Basic of PEMFCs

A schematic of a PEMFC is provided in Figure 1-3. As shown in this figure, hydrogen is the fuel in the anode side, and oxygen or air is the oxidizer streaming into the fuel cell in the cathode side.

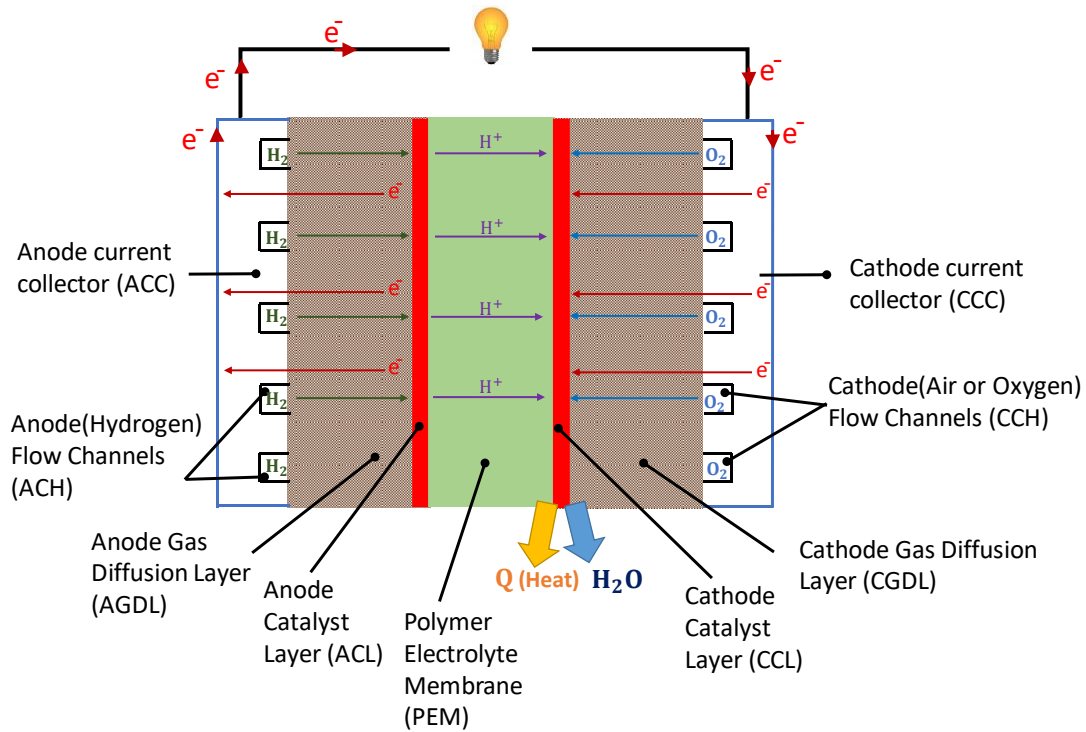


Figure 1-3. Fuel cell schematic

The main components of PEMFCs are provided in Table 1-2. The material used for each component, as well as the role of each component, is briefly explained as follows:

Table 1-2. PEMFC components [7]

Component	Description	Common Types
Proton Exchange Membrane (PEM)	Enables hydrogen ions to travel from the anode to the cathode.	Persulfonic acid membrane (Nafion 112, 115, 117)
Catalyst Layers (CLs)	Breaks the fuel into protons and electrons. The protons combine with the oxidant to form water at the fuel cell cathode. The electrons travel to the load.	Platinum/carbon catalyst
Gas Diffusion Layers (GDL)	Allows fuel/oxidant to travel through the porous layer while collecting electrons	Carbon cloth or Toray paper
Flow Field Plates	Distributes the fuel and oxidant to the gas diffusion layer	Graphite, stainless steel
Gaskets	Prevent fuel leakage and helps to distribute pressure evenly	Silicon, Teflon
End Plates	Holds stack layers in place	Stainless steel, graphite, polyethylene, PVC

Figure 1-3 shows how PEMFC operates. Hydrogen enters into the ACH and is absorbed onto the anode surface, where it is catalytically broken down into protons and electrons. Protons diffuse across the membrane, while electrons are driven through an external load. Protons and electrons meet again at the cathode, where they react with oxygen to produce water and heat. Following reactions occur in a fuel cell in normal operating conditions [1]:



The kinetics of this reaction is determined by the amount of available catalyst. Combining these reactions would result in the following global reaction:



From this reaction, by calculating the difference between Gibbs free energy of the product (water) and reactants (hydrogen and oxygen gasses) as  $\Delta G$ , we can calculate the maximum electrical energy. Therefore, the ideal voltage of the PEMFC could be calculated from the following equation [1]:

$$V_{oc} = \frac{-\Delta G}{2F} \quad (1-1)$$

F in Equation (1-1) corresponds to Faraday's constant.  $\Delta G$  also depends on species' pressures and concentrations and can be derived from Equation (1-2) [1,5].

$$\Delta G = \Delta G_f^0 - RT \ln \left( \frac{P_{H_2} \cdot P_{O_2}^{0.5}}{P_{H_2O}} \right) \quad (1-2)$$

T is the temperature, and R is the universal constant.  $P_{O_2}$ ,  $P_{H_2}$ , and  $P_{H_2O}$  correspond to species partial pressures. Dividing both sides of equation (1-2) by  $nF$ , we can derive the open-circuit voltage of PEMFC [1,5].

$$V_{oc} = V_0 + \frac{RT}{nF} \ln \left( \frac{P_{H_2} \cdot P_{O_2}^{0.5}}{P_{H_2O}} \right) \quad (1-3)$$

$V_{oc}$  is the open-circuit voltage and its value is about 1.2 V for low-temperature PEMFCs (under 100 °C). However, the operating voltage of a PEMFC is lower than this amount due to available voltage losses. These losses are usually categorized into the followings:

- Activation losses: This is a voltage loss that drives the electrochemical reaction, and the value of this drop depends on the catalyst material and the micro-structure of MEA. Activation losses are mostly shown by a sudden drop on the open-circuit voltage at very low current densities.
- Ohmic losses: This loss is associated with the resistance to charge transportation caused by electrodes and the electrolyte. Hydrogen ions flow through electrolyte, and electrons flow through the solid parts of the electrodes. The resistance to the movement of these charges is the ohmic loss, which is proportional to the current value, and the coefficient corresponds to ohmic resistance.
- Concentration losses: These drops correspond to mass transport losses due to the reactant activity, structure of electrodes, and current density.

The effect of these losses on the polarization curve is shown in Figure 1-4.

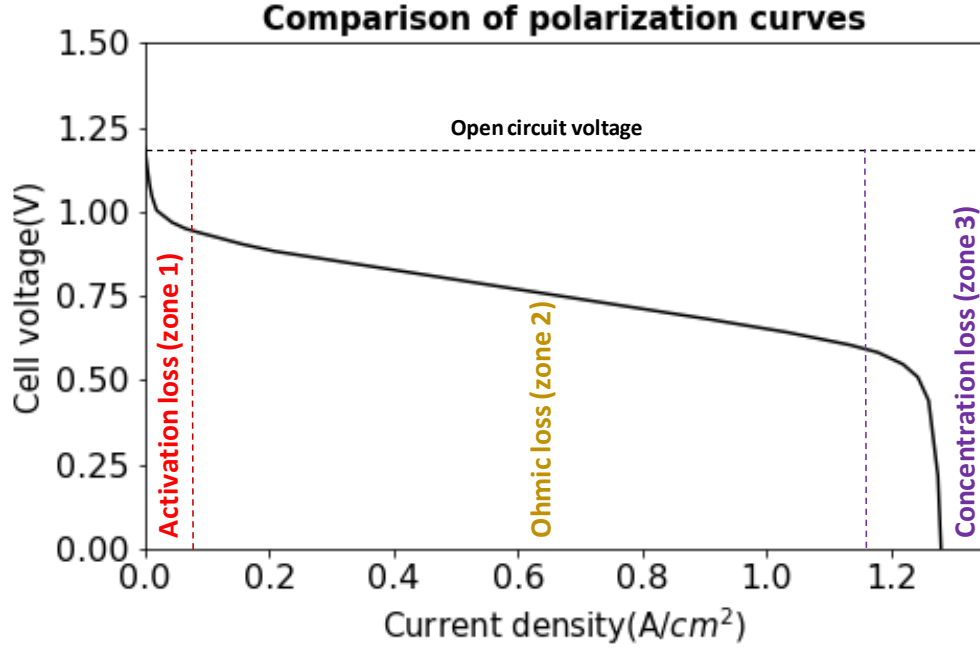


Figure 1-4. Different losses on the polarization curve

By considering the PEMFC losses, PEMFC operating voltage, and PEMFC power density can be obtained from Equation (1-4) and Equation (1-5).

$$V = V_{oc} - \eta_{act} - \eta_{ohm} - \eta_{conc} \quad (1-4)$$

$$P = VI = (V_{oc} - \eta_{act} - \eta_{ohm} - \eta_{conc})I \quad (1-5)$$

## 1.2. Leaky PEMFCs and Hydrogen Pumping

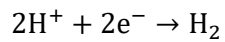
Leaks emerge in the fuel cell membrane as a result of many processes such as MEA degradation, mechanical and chemical degradation, variable load changes, continual start-up and shut-down, operation under low humidity condition, and oxygen starvation [12–15]. The hydrogen leaking into the cathode results in the direct combination of  $H_2$  and  $O_2$  as follows:



Reaction (3) does not refer to the combined reaction of the anode and cathode in the normal operating mode. In fact, this reaction represents the direct combustion of oxygen and hydrogen that leaked to the cathode side and consumed the useful oxygen. This

reaction does not generate any current and conversely results in lower PEMFC performance since it lowers the amount of oxygen at the catalyst layer and accelerates oxygen starvation. In other words, hydrogen ions need to compete with hydrogen molecules to participate in the Oxygen Reduction Reaction (ORR).

There is another interesting reaction that could happen because of hydrogen leakage and oxygen starvation, which is called hydrogen pumping [12–15]. Hydrogen pumping happens when PEMFC works under oxygen starvation conditions. In this mode, first, all available oxygen combines with the hydrogen ions passing through the membrane. While the cell becomes fully starved and the current is further increased, the hydrogen ions recombine with the electrons flowing through the electrical circuit and form hydrogen molecules in the cathode (Reaction 4). Hydrogen pumping could also happen in the case of high currents and small leaks [12–15].



(Reaction 4) Cathode Reaction

In addition, if cells are connected in series in a fuel cell stack, hydrogen will be accumulated over all the cells and would be a higher amount at the cathode outlet. In this case, the cell essentially acts as a hydrogen pump, which results in hydrogen emissions in the cathode outlet. This phenomenon is called hydrogen pumping, and the cell consumes power instead of producing it. The schematic of leaky fuel cell operation is provided in Figure 1-5. It is really important to understand the difference between the hydrogen leak versus hydrogen pumping. Through this thesis, leak and leak transfer corresponds to hydrogen crossover from anode to cathode side through pinholes. On the other hand, hydrogen pumping or pumped hydrogen corresponds to the direct reaction of hydrogen ions and electrons, which would result in hydrogen generation in the cathode side in case of full starvation. It is also necessary to mention that hydrogen pumping occurs mainly as a result of hydrogen leakage in a stack where cells competing with each other over the oxygen or airflow to produce current. However, the extremely high currents could result in full starvation or hydrogen pumping. This phenomenon rarely happens since employing a controller and adjusting the stoichiometry ratio of reactants would prevent this fault.

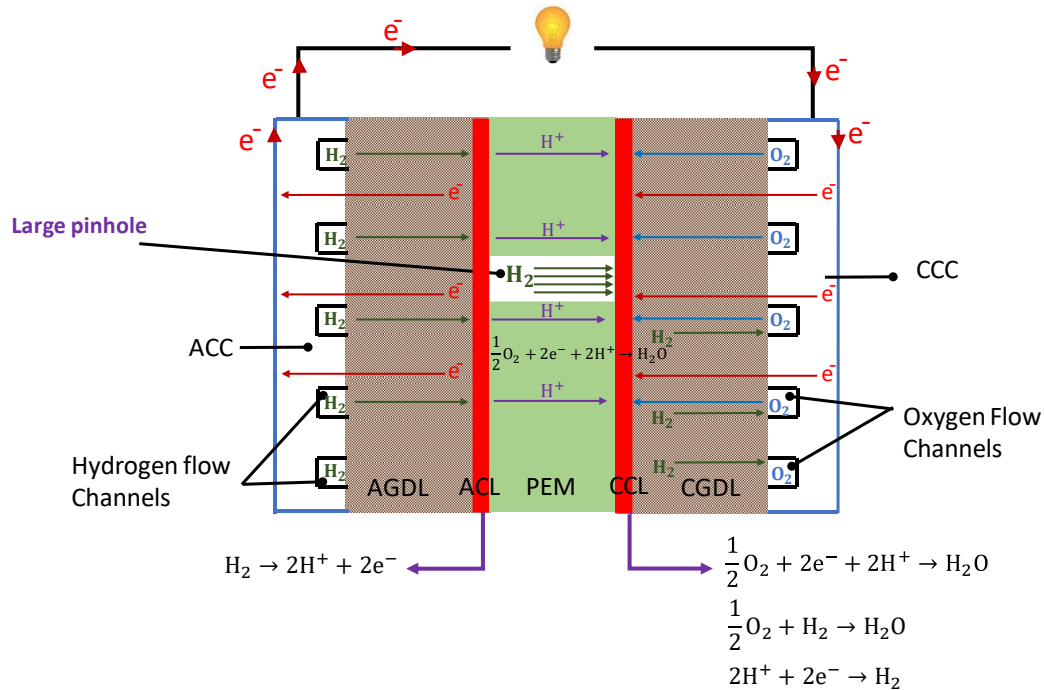


Figure 1-5. Schematic of a leaky PEMFC in hydrogen pumping mode

### 1.3. Objectives

The primary goal of this project is to facilitate the process of PEMFC commercialization by reducing the cost of ownership and improving the durability of PEMFCs. These objectives are realized in two phases; the first one is to find the effect of catalyst distribution on the performance and the inception of oxygen starvation in steady-state mode. The second one is to develop a diagnosis tool, which acts as a virtual hydrogen sensor. There are several steps defined to reach the main objectives. Research objectives are provided as follows:

- Finding the effect of catalyst distribution on PEMFC performance as well as oxygen starvation initiation
- Finding the optimal catalyst distribution which results in maximum performance and maximum delay in starvation initiation
- Developing a fast, simple pseudo two-dimensional model to simulate steady-state and transient PEMFC behavior for both healthy and leaky cells by accounting for the effect of the hydrogen pumping

- Comparing the results of the pseudo two-dimensional model with experimental data, the comparison with experimental data illustrates the level of model precision.
- Subjecting the pseudo two-dimensional model to different operating conditions and creating a dataset
- Data training and building ML classifiers and regressors to detect and quantify the leakage

## 1.4. Research Roadmap

A roadmap, shown in Figure 1-6, was prepared to achieve the goals of this research. The roadmap consisted of the following main steps:

- Developing a two-dimensional, two-phase, finite volume PEMFC computational fluid dynamic (CFD) model to investigate the effect of the catalyst layer distribution on PEMFC power density and oxygen starvation
- Validation of the CFD model versus the experimental data
- Multi-objective optimization of PEMFC maximum power density and minimum oxygen concentration along CCL to ensure the higher performance of the system and to delay the inception of oxygen starvation. Genetic Algorithm (GA) is used for the optimization purpose.
- Developing a simple two-dimensional pseudo numerical model to simulate PEMFC performance under normal and starvation operating modes. The model must be fairly fast and precise to simulate PEMFC voltage response and hydrogen emissions under different current loads. The model is built on the model presented by Vijayaraghavan et al. [15] and includes hydrogen pumping.
- The model is run for several operating conditions in the steady-state mode for different leakage amounts. Voltage values are recorded for each simulation to form a dataset.

- ANN and KNN classifiers are trained and tested on the built datasets to classify cells into healthy or leaky cells. The performance of these classifiers is evaluated based on classifier performance indexes.
- ANN and KNN regressors are trained and tested on the built datasets to quantify hydrogen leakage in the leaky cells. The performance of these regressors is evaluated based on regressor performance indexes.
- Presenting the final hydrogen leakage diagnosis tool and discussing future works

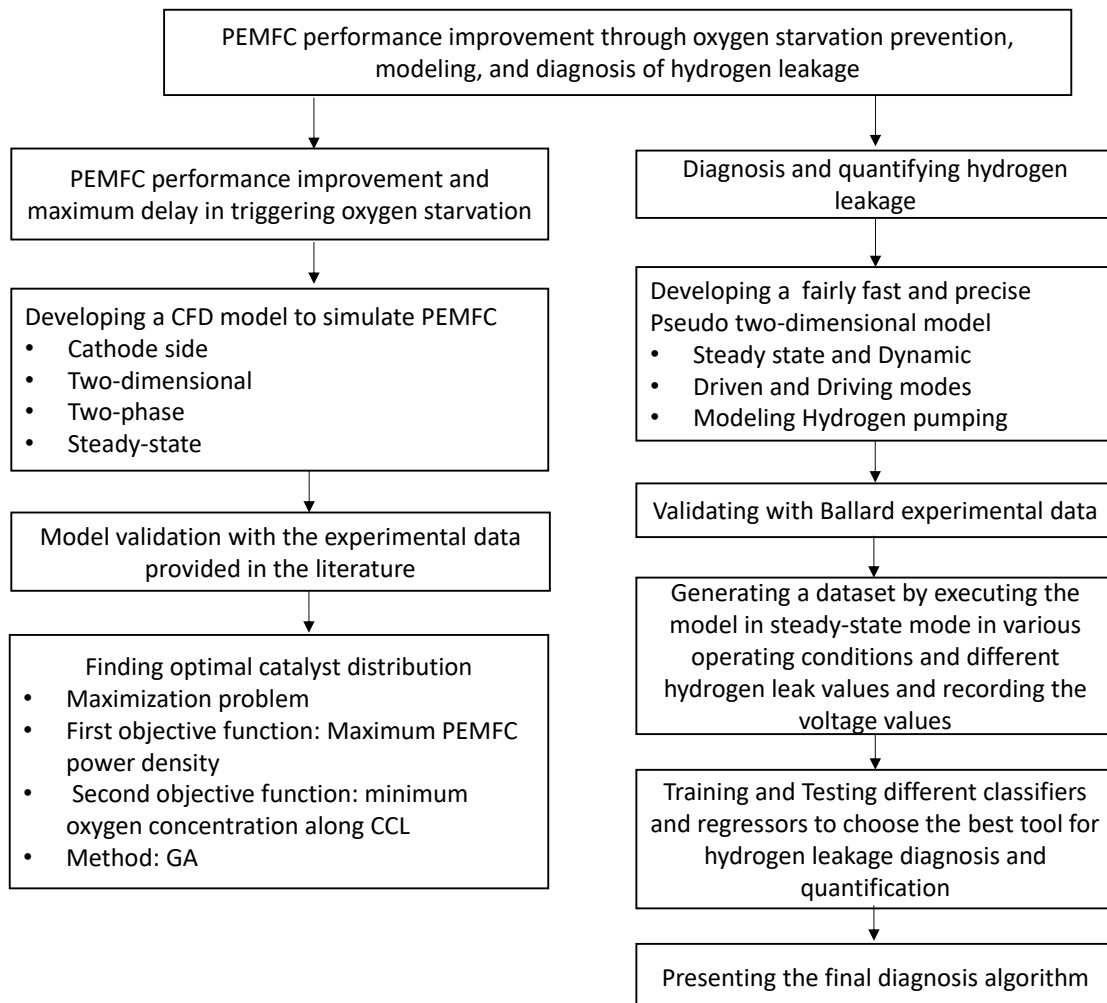


Figure 1-6. Thesis roadmap



## **1.5. Scholarly Contributions**

### **1.5.1. Contributions Related to Thesis**

- S. Ebrahimi, J. Devaal, M. Narimani, K. Vijayaraghavan, "Transient model of oxygen-starved proton exchange membrane fuel cell for predicting voltages and hydrogen emissions", *Int. J. Hydrogen Energy*. 42 (2017) 21177–21190. doi:10.1016/j.ijhydene.2017.05.209.
- S. Ebrahimi, B. Ghorbani, K. Vijayaraghavan, "Optimization of catalyst distribution along PEMFC channel through a numerical two-phase model and genetic algorithm Catalyst Layer", *Renew. Energy*. 113 (2017) 846–854. doi:10.1016/j.renene.2017.06.067.
- S. Ebrahimi, R. Roshandel, K. Vijayaraghavan, "Power density optimization of PEMFC cathode with non-uniform catalyst layer by Simplex method and numerical simulation", *Int. J. Hydrogen Energy*. 41 (2016) 22260–22273. doi:10.1016/j.ijhydene.2016.07.247.
- K. Vijayaraghavan, S. Ebrahimi, Jake DeVaal, "Transient Model of Oxygen Starved PEMFC for Predicting Voltages and Hydrogen Emissions", Poster presented in 3rd International Zing Conference, Cancun, Mexico, December 2015

### **1.5.2. Other Contributions**

- B. Ghorbani, S. Ebrahimi, K. Vijayaraghavan, "CFD modeling and sensitivity analysis of heat transfer enhancement of a ferrofluid flow in the presence of a magnetic field", *Int J Heat Mass Transf* 2018;127:544–52. doi:10.1016/j.ijheatmasstransfer.2018.06.050.
- B. Ghorbani, MA. Akhavan-Behabadi, S. Ebrahimi, K. Vijayaraghavan, "Experimental investigation of condensation heat transfer of R600a/POE/CuO nano-refrigerant in flattened tubes", *Int Commun Heat Mass Transf* 2017;88:236–44. doi:10.1016/j.icheatmasstransfer.2017.09.011.

- B. Ghorbani, F. Kowsary, S. Ebrahimi, K. Vijayaraghavan, "CFD modeling and optimization of a latent heat storage unit for running a solar assisted single effect Li-Br absorption chiller using multi-objective genetic algorithm", *Sustain Cities Soc* 2017;34:321–34. doi: 10.1016/j.scs.2017.05.023.
- MS. Ferdoues, S. Ebrahimi, K. Vijayaraghavan, "Multi-objective optimization of the design and operating point of a new external axis wind turbine", *Energy* 2017;125:643–53. doi:10.1016/j.energy.2017.01.070.
- MS. Ferdoues, S. Ebrahimi, K. Vijayaraghavan, "Optimization of Power and Operation Characteristics of a New External Axis Wind Turbine", *ASME 2016 International Design Engineering Technical Conferences and Computers and Information in Engineering Conference*, Volume 2A: 42nd Design Automation Conference, Charlotte, North Carolina, USA, August 21–24, 2016, doi: 10.1115/DETC2016-60480

## **Chapter 2. Literature Review**

This chapter aims to summarize the current literature in six sections. In the first section (Section 2.1), different approaches for PEMFC modeling are explained. Section 2.2 provides a summary of the works on starvation and specifically oxygen starvation. Section 2.3 provides a summary of the literature on non-uniform catalyst distribution. Section 2.4 provides a summary of the works that focused on hydrogen leakage diagnosis. Section 2.5 explains the gap in the literature, our contributions, and the novelty of the current work. The chapter ends with Section 2.6, where the research motivations are stated.

### **2.1. PEMFC Modeling Approaches**

PEMFC modeling has received huge attention over the last twenty years, and different types of models were developed for different purposes. For instance, parametric studies enable scientists and researchers to investigate the effect of different parameters such as material properties, operating conditions, and geometric parameters on the system, while experimental studies are employed to understand when physical phenomena are not well understood or difficult to model. On the other hand, analytical and lump models are more suitable for control purposes where computational cost matters.

Analytical models are developed by making major assumptions and simplifying variable distributions so that equations can be solved analytically. As one of the early works, Standaert et al. [16] developed a general fuel cell model in both isothermal and temperature-variant modes. Although analytical models are very easy to use and can provide an approximation of the expected outcome, they are not beneficial in capturing transport phenomena in different layers of PEMFCs [17]

Semi-empirical and empirical models utilize experimental tests to derive algebraic and differential equations. However, empirical and semi-empirical models require time-consuming experiments and might not be able to provide an adequate physical understanding of phenomena. Therefore, mechanistic models have been developed by deriving differential and algebraic equations based on the physical and electrochemical phenomena that occur in PEMFCs. Computational and numerical solution algorithms are then employed to solve the derived sets of equations. Mechanistic models could be divided into two categories; multi-domain and single domain. Single domain models are

mainly used for numerical domains with the same governing equations, while multi-domain models couple different governing equations for different regions and solve them numerically [17].

Mechanistic models can be further subcategorized into fully numerical and pseudo numerical models. Early mechanistic numerical PEMFC models [18–20] were one-dimensional, steady-state, and isothermal [18–20]. More complex two-dimensional [21,22] and three-dimensional models [23,24] have been developed over time. Many of these models are CFD models to capture details of reactant transport, water management, and heat management in fuel cells. However, there is always a trade-off between accuracy and level of details with computational cost and resources. The computational intensity of CFD models resulted in the development of pseudo numerical models for online-monitoring and control applications. Pseudo numerical models utilize bulk simplification or other assumptions to simplify the numerical procedure and to lower the computational cost. As an example, Vijayaraghavan et al. [15] assumed that voltage is constant across the cell and also used an analytical equation to calculate the concentration at the catalyst layer.

It is important to note that the choice of a PEMFC model depends on the application. In our work, two PEMFC models are developed. The first model is two-dimensional, steady-state, and two-phase. The purpose of this model is to simulate the effect of catalyst layer distribution on PEMFC performance and the inception of oxygen starvation. Therefore, the model is needed to be detailed enough to capture major transport and electrochemical phenomena that occur in the fuel cell.

The second model is used for leakage diagnosis and online-monitoring purposes. Therefore, it should be fast and efficient and simulate PEMFC behavior in both starved and normal operating modes.

## **2.2. Oxygen Starvation**

Starvation occurs when the catalyst layer is depleted out of reactants. Starvation can be divided into fuel starvation and oxidizer starvation. In PEMFC, fuel starvation is the same as hydrogen starvation and happens when the concentration of hydrogen reaches zero at

some or entire ACL. Similarly, oxidizer starvation refers to oxygen starvation when oxygen concentration reaches zero at some part or entire CCL. Starvation can be subcategorized into local starvation and complete starvation. Local starvation occurs due to the lack of reactants at some parts of the CL, whereas in complete starvation, the entire catalyst layer completely is depleted out of reactants. Starvation usually happens due to the following reasons [25]:

- Non-uniform reactant distribution in the flow field due to design deficiency
- Dynamic loads and sudden start-up/shut down procedures
- Improper stoichiometry ratio of input fuel/oxidizer
- Water management issues; a thin layer of water formed at the catalyst layer could block reactants from reaching the catalyst layer
- Compressor control failures
- Hydrogen crossover due to MEA degradation

Fuel starvation and oxidizer starvation could result in the generation of oxygen and hydrogen in the anode and cathode, respectively. The latter case is named hydrogen pumping and was explained in Section 1.2, whereas the former one is water electrolysis [26]. The related chemical reactions are provided in Table 2-1.

Table 2-1. Reactant starvation reactions

Electrochemical reactions	Type of starvation	Location
$2\text{H}_2\text{O} \rightarrow \text{O}_2 + 4\text{H}^+ + 4\text{e}^-$ (water electrolysis)	Fuel (hydrogen) starvation	Anode
$\text{C} + 2\text{H}_2\text{O} \rightarrow \text{CO}_2 + 4\text{H}^+ + 4\text{e}^-$	Fuel (hydrogen) starvation	Anode
$\text{O}_2 + 4\text{e}^- + 4\text{H}^+ \rightarrow 2\text{H}_2\text{O}$	Oxidizer (oxygen) starvation	Cathode
$2\text{H}^+ + 2\text{e}^- \rightarrow \text{H}_2$ (hydrogen pumping)	Oxidizer (oxygen) starvation	Cathode

Most of the literature [27–33] has mainly focused on fuel starvation and its effect on MEA degradation. Table 2-2 provides a summary of these works as follows:

Table 2-2. Literature on hydrogen starvation

Reference	Methodology	Findings
Meyers et al. [27]	Modeling	They developed a one-dimensional model to simulate fuel starvation in PEMFCs. They inferred that the reverse current occurs in the fuel-starved area where current flows from cathode to anode. They further concluded that localized fuel starvation could induce permanent damages to the cathode by accelerating degradation mechanisms such as carbon corrosion. They suggested the implementation of the uniform fuel distribution along the catalyst layer through designing control systems to handle transient start-up and shut-down conditions.
Ohs et al. [28]	Modeling	They developed a two-dimensional, steady-state model. Hydrogen was diluted with nitrogen, and Comsol was used to perform CFD simulation. Their model accounted for carbon corrosion by using a simplified Butler-Volmer approach, and their results fit very well with the experimental data. They inferred that hydrogen starvation could result in a high cathode potential gradient.
Resier et al. [29]	Experimental	Their experimental setup included two connected electrodes. The anode of the first cell was supplied with hydrogen, and the second anode was fed with oxygen to simulate hydrogen starvation. They noticed that fuel starvation could result in MEA damages.
Liang et al. [30]	Experimental	They characterized important parameters such as current distribution, anode and cathode potentials, and the voltage response. Their observations include water electrolysis, current reversal, and non-uniform current distribution. The highly non-uniform current density distribution led to the temperature increase of the

		upstream zone of ACL, which resulted in a degradation of the platinum particles and platinum agglomeration. They noticed severe carbon corrosion in extreme hydrogen starvation conditions.
Tang et al. [31]	Experimental	They studied the effect of PEMFC cathode carbon corrosion under hydrogen starvation. They inferred that the formation of the hydrogen/air boundary at ACL could accelerate the loss of active surface area of CCL
Knights et al. [32]	Experimental	Knights et al. [32] studied PEMFC behavior under complete hydrogen starvation. They used the polarization curve to investigate the effect of complete starvation under different humidification levels and different temperatures. They noticed drops in voltage values due to the rise of anode potential. They also confirmed oxygen generation from water electrolysis when voltage became smaller than -0.55.
Huang et al. [33]	Experimental	MEA was tested under the vehicle operating condition, and the effect of the hydrogen flow rate was investigated on performance. Scanning Electron Microscope (SEM) was employed to study the structure of MEA, and an increase in the average size of anode and cathode catalyst particles was observed. Hydrogen starvation caused carbon corrosion, which led to high surface energy agglomerate formation that consequently resulted in the performance drop.

The majority of the publications [27–33] have focused on hydrogen starvation, while fewer works studied oxygen starvation [34–39]. Most of these works employed experimental methods to first confirm oxygen starvation and hydrogen pumping, and second, to

investigate how oxygen starvation degrades MEA. A summary of these works provided in Table 2-3.

Table 2-3. Literature review on oxygen starvation

Reference	Methodology	Findings
N. Yousfi-Steiner et al. [35]	Review on catalyst degradation works	Oxygen starvation could cause platinum dissolution and carbon corrosion in the catalyst layer. They furthermore concluded that catalyst degradation accelerates MEA degradation, which would eventually result in the formation of holes in the MEA. They inferred that adjusting the stoichiometry ratios would prevent catalyst degradation.
Rao et al. [36]	Modeling / Experiment	They performed a transient study and inferred that it is not possible to prevent oxygen starvation by only adjusting the oxygen excess ratio. Based on their results, since the oxygen distribution is highly non-uniform at high current densities, oxygen concentration could become zero adjacent to the outlet, and therefore oxygen starvation is inevitable. Feeding more oxygen may alleviate starvation, but oxygen starvation is still inevitable in case of dynamic changes due to the lag in the response time. They concluded that designing a non-linear controller is required to prevent oxygen starvation.
Mousa et al. [37]	Modeling / Experiment	Mousa et al. [37] noticed that in the case of hydrogen cross-over leaks, fuel cell performance drops since hydrogen molecules directly react with oxygen molecules and produce water. Recombination of reactants would reduce the amount of oxygen at the catalyst layer on the cathode side, and oxygen starvation occurs subsequently. Also, a thin layer of water formed adjacent to the membrane blocks



		oxygen molecules from reaching the reaction site and intensifies oxygen starvation. They noticed hydrogen presence in the cathode outlet in case of oxygen starvation and confirmed the hydrogen pumping effect.
Taniguchi et al. [38]	Experimental	They used in situ cyclic voltammetry to measure the active surface area of the catalyst layer and noticed a noticeable reduction. They also used Transmission electron microscopy (TEM) to image the CCL before and after the cell reversal experiment for two hours. Significant degradation in the outlet area and dissolution in catalyst particles were among their findings. The loss of platinum surface area was considered as a result of sintering or recrystallization within the porous cathode
Bodner et al. [34]	Experimental	Different area sizes of PEMFC are tested under accelerated stress tests. Different cycles (10 and 60-second cycles) are chosen to investigate the effect of oxygen starvation on the system. Voltage response at the anode and cathode inlet and outlets were recorded. Negative voltage values were observed during a long starvation period. However, within a short cycle of starvation, the available air present in the gas phase and the gas lining compensated the negative voltage and sustained the cell. Thus, only small voltage fluctuations were observed under short cycles. Also, the highly non-uniform current distribution was observed due to oxygen starvation at some parts of CCL. The temperature gradient was changed, and hydrogen was detected at the cathode outlet during the high starvation cycle. Computed tomography was

		employed to study the effect of oxygen starvation on MEA degradation, and carbon corrosion and catalyst agglomeration were observed.
Inaba et al. [39]	Experimental	Inaba et al. [39] studied the effect of hydrogen crossover on MEA degradation. Heat generation, hydrogen peroxide formation, and catalytic combustion were accounted for MEA degradation. They also inferred that reactive oxygen radicals could form in the presence of minor impurities. These radicals could expedite the process of membrane degradation

Liu et al. [40] developed a model to back up their observations on the effect of reactant starvation on PEMFC performance. They simply deducted a constant term from inlet reactant concentrations to model reactant starvation. They used CFD-ACE+ V2003 to simulate PEMFC under steady-state operating conditions. Concentration and current density distributions for anode and cathode starvations were derived and discussed. However, the experimental tests illustrated more interesting results. Twelve embedded current collectors are employed to record the current distribution. The current for each segment was measured with a series of 10mΩ resistances. The voltage share of each resistance was calculated by a computer. Polarization curves showed how subcells close to the outlets became starved very fast at lower current densities. For the same subcells, the shape of polarization curves was significantly different for oxygen starvation and hydrogen starvation. For hydrogen starvation, outlet subcells current densities dropped to zero as a result of voltage drop. Middle subcells' current densities became zero at lower cell voltage, while inlet subcells seemed to be impacted less. The authors concluded that hydrogen starvation would significantly affect the catalyst layer's outlet area while having less impact on the rest of the catalyst layer. On the contrary, they noticed that oxygen starvation would affect the current generated in the entire catalyst layer. Therefore, the highly non-uniform current density in hydrogen starvation is inevitable, while the current distribution in the case of oxygen distribution is less heterogeneous.

By discussing the literature provided in this section, we can infer that both anode and cathode starvations could cause severe degradation damages to the MEA structure.

These damages can be summarized as carbon corrosion, platinum dissolution, catalyst agglomeration, catalyst combustion, catalyst poisoning, reduction in MEA thickness, catalyst sintering, and other chemical degradations. It is also inferred that providing a uniform reactant distribution at the catalyst layer could result in a delay in oxygen starvation and improve the durability of PEMFCs. Also, there is a need to model hydrogen pumping to track the amount of hydrogen generated in the cathode side as a result of oxygen starvation. Eventually, developing a virtual hydrogen sensor to prevent further degradation of MEA due to hydrogen leakage is vital to improve the lifetime of PEMFCs.

### **2.3. Non-uniform Catalyst Distribution**

Oxygen distribution in the catalyst layer is highly non-uniform, which can lead to inefficient use of platinum within the catalyst layer. This may lead to oxygen starvation in the cathode side at high current densities. Therefore, developing a novel method that could increase the maximum current density while improving PEMFC performance is interesting and of importance. The idea of conducting non-uniform catalyst distribution could result in the realization of both defined milestones.

The idea of non-uniform catalyst distribution was first presented by Kulikovsky [41]. He developed a simple analytical model and showed that non-uniform catalyst distribution could improve the fuel cell performance noticeably. Several other studies also focused on performance improvement by applying non-uniform catalyst distribution and efficient use of platinum. For instance, Srinivasarao et al. [42] considered multiple ultra-thin layers instead of a single layer for the PEMFC catalyst layer. In their work, the effect of catalyst loading gradient across fuel cell layers was investigated while keeping the whole catalyst amount constant. They concluded that the performance of multiple catalyst layers was superior to that of a single catalyst layer. Roshandel et al. [43] evaluated the effect of catalyst loading gradient in the catalyst layer. They considered different variations of catalyst loading in two directions, “across the layer” from the membrane/catalyst layer interface to GDL and “in catalyst plane” under the channels and land areas. After comparing six cases of non-uniform catalyst loading distribution, they concluded that using non-uniform catalyst distribution could either improve or aggravate the whole performance of a cell. They also concluded that loading more catalysts under the channel would improve fuel cell efficiency. Zhang et al. [44] managed to perform variable catalyst loading to improve the uniformity of local current density. In their simulation, they divided CCL into

three different parts with different mass catalyst loading while keeping the total amount of catalyst constant. They considered mass catalyst loading as three-step functions. Employing the Nelder-Mead Simplex method, they managed to find optimum values for these three-step functions. They also performed experimental tests to back up their theoretical findings.

In another interesting study, Mathieu-Potvin et al. [45] developed a numerical single-phase model to study the effects of catalyst layer topology and catalyst layer thickness on PEMFC performance. In the first step, they managed to find optimum ACL and CCL thicknesses under two main assumptions, which are constant catalyst density and the fixed amount of catalyst. In the second step, they used a gradient-based method to find the optimum catalyst distribution in the CCL. They concluded that PEMFC power density increases by inserting more catalyst close to the membrane.

Although finding the optimum catalyst distribution can improve fuel cell efficiency, it can also provide uniform reactant distribution at the catalyst layer. Depositing more platinum at the CCH entrance and less at the CCH outlet would result in lower oxygen concentration at the cathode inlet and higher at the outlet comparing to the case of uniform catalyst distribution. Generally, oxygen starvation triggers close to the CCH outlet, where the oxygen concentration is the lowest. Therefore, non-uniform catalyst distributions that could result in less oxygen consumption in the CCH outlet might be able to delay the oxygen starvation. Some literature [35,46,47] found that heterogeneous current distribution caused by negative currents produced in the starved area of the catalyst layer could be used as an indicator for the inception of complete starvation. However, they did not investigate the effect of non-uniform catalyst distribution. As a part of this research, a novel algorithm based on the combination of a two-dimensional fuel cell model and an optimization method will be developed to find the optimal catalyst distribution, which generates the maximum PEMFC power density and results in the maximum delay in starvation initiation.

## **2.4. Leakage Diagnosis in PEMFC**

It is important to understand different methods of failure diagnosis before discussing the leakage related literature. Fault diagnosis is a very important component in various industries and mainly defined in the following categories [48]

- Fault detection: In this case, the purpose of the diagnosis tool is to detect the

inception of the fault before it could cause significant damages.

- Fault isolation: Different faults are localized and isolated.
- Fault identification or fault analysis: The type of the fault and its magnitude and its causes are determined.

PEMFC has a multicomponent and multiphasic structure, and therefore many types of faults could happen in PEMFC. Dry membrane, platinum dissolution, carbon corrosion, insufficient hydrogen feed, GDL crack, pinhole formation in the membrane, and hydrogen leakage are some examples of the faults that could occur in PEMFC. Therefore, fault diagnosis could help us adjust the operating condition to assure healthy performance. In the case of severe damage, the defected component or cell could be replaced to prevent the complete and hazardous breakdown of the system.

In general, fault diagnosis methods in PEMFCs are divided into two categories; model-based and non-model based. Figure 2-1 categorized different failure approaches in either model-based or non-model based diagnosis methods.

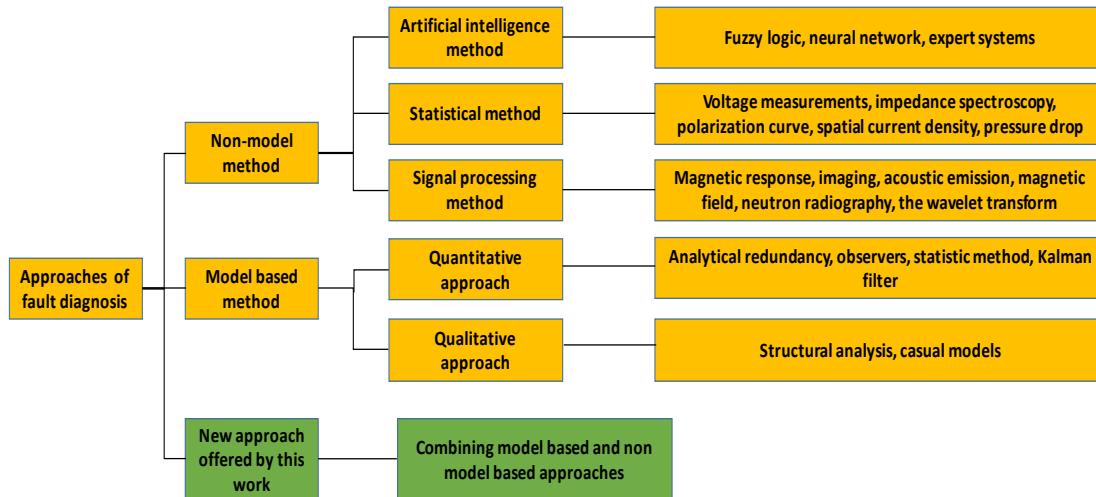


Figure 2-1. PEMFC failure diagnosis approaches

In the model-based approach, a model is required to provide a deep understanding of the cell and its internal phenomena. Due to the complicated and multi-physics structure of PEMFCs, relations between different natures (thermodynamic, electrical, electrochemical, and fluidic) must be derived and modeled. Model-based approaches work based on an online comparison between the monitored data and the data derived from precise dynamic simulations of the system. Here, a single residual or multiple residuals are calculated based on the difference between the real data and the simulated data. Large residual(s) would be attributed to the presence of fault/faults. These approaches are categorized into

two categories; quantitative and qualitative models. In the quantitative case, analytical models or observers are employed to predict the performance of the system and calculate the residual, whereas, in the qualitative methods (Black-box models), the physics of the system is not investigated and instead, black-box models such as neural networks and fuzzy algorithms are employed to simulate the system performance and eventually calculate the residual. The problem with black-box models is that the residual may not be able to classify the type of faults. For instance, let's assume a neural network is trained based on temperature, current, and anode and cathode pressures to simulate the voltage response. Therefore, the simulated voltage does not change with a fault if that fault does not significantly change the mentioned parameters. However, the role of AI methods in fault diagnosis is inevitable. The methods provided in each sub-layer of Figure 2-1 are introduced and explained in detail in [35,49–52].

On the other hand, non-model based methods work mainly based on historical data and a decision-making process. Therefore, there is a need for a large amount of data that can mainly be derived through experimental tests. This category is called non-model based since there is no mathematical model derived for each component and their interactions. The data is mainly collected through experimental tests such as voltage measurements, electrochemical impedance spectroscopy (EIS), cyclic voltammetry (CV), polarization curve, spatial current density, and pressure drop measurements.

Zhongliang Li [53] categorized these methods based on the cost and whether they can be used for online/offline diagnosis. Table 2-4 provides a summary of this investigation. In-depth explanations of non-model based approaches are provided in [35,49–52].

Table 2-4. An investigation of non-model based fault diagnosis models [53]

Measurement type	Variable	Online/Offline	Cost
Regular measurement	Cell/stack voltage	Online	Low/Medium
	Current	Online	Low
	Temperatures	Online	Low
	Pressures	Online	Medium
	Flow rates	Online	High
	Humidifies	Online	Medium
Special measurement	Polarization curve	Offline	Low
	EIS (Traditional)	Offline	High
	LSV	Offline	Medium
	CV	Offline	Medium

Figure 2-1 introduces a third category of models that are based on the combination of model-based and non-model based methods. The data is collected through fairly simple and fast analytical or pseudo numerical models rather than through experimental tools in this category. The difference between this category and model-based approaches is in the level of details captured by the model. Models in the third category must capture and simulate the effect of different faults on PEMFC performance. These models do not compare the residue of normal performance and the online response to determine the fault type. Instead, the models in this category are subjected to different types of faults, and PEMFC characteristics are recorded under different operating conditions. The purpose of this part is to create a big dataset based on a fairly fast and precise model. The data further will be analyzed through artificial intelligence, signal processing, or ML methods to move backward and diagnose the fault. This method is not model-based since the model is not detailed enough for each component, and the fault is not detected by comparing the output of the model with the online PEMFC data. Also, it is not a non-model based method since there is a simple model that generates a dataset rather than expensive, time-consuming experimental tests or variable observations. A simple schematic of the third category of data is shown in Figure 2-2.

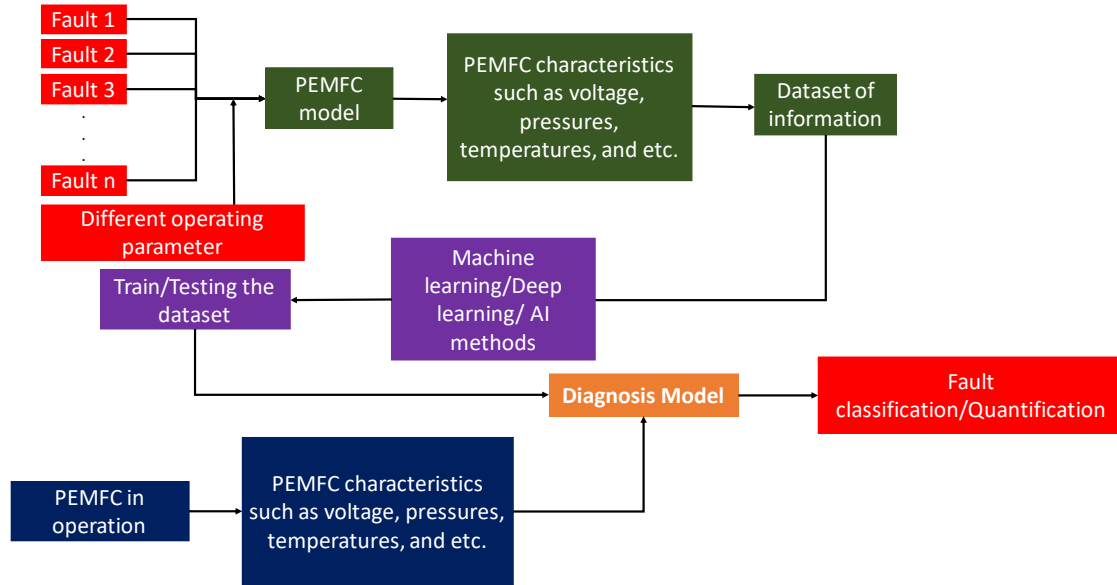


Figure 2-2. General algorithm of combined fault diagnosis approach

Most of the works [54–57] that tried to identify oxygen starvation/hydrogen pumping and hydrogen crossover studied the dynamic behavior of PEMFC parameters such as voltage, current, temperature, and pressure. These works showed that voltage could drop to negative values during sudden dynamic changes (start-up and shut down). This is more identifiable when a cell is extremely starved, or there is a big leak in the MEA, and at high current densities. Tian et al. [54] supplied two PEMFC stacks with some electrical signals and measured the open-circuit voltages at different reactants' supply flow rates and pressures. The voltage pattern of healthy cells was compared with the ones with fault to investigate the abnormality of the response. In order to highlight the presence of leakage in the membrane, the anode compartment is pressurized with nitrogen, and the cathode compartment is sealed at ambient pressure. They monitored the pressure, and the pressure increase in the cathode side was attributed to the presence of leakage. They also fed stack with hydrogen and air for ten seconds and then suddenly stopped the gas flow. They monitored OCV and noticed that healthy cells could operate at high voltage (close to 0.9) for around one minute and then experience a drop in voltage while the leaky cell voltage drops much earlier comparing to the healthy ones. They justified their observations by suggesting that the buffer volumes of hydrogen are consumed much faster in the defected cell, which results in a fast decrease of hydrogen partial pressure at the reaction site. The fast hydrogen consumption at the anode could be due to hydrogen leak through a hole or crack in the membrane, and if that is that the case, combustion may be possibly diagnosed by temperature measurement at the stack outlet. Eventually, they



attributed a high deviation of voltage behavior to the presence of hydrogen leakage. It is necessary to mention that hydrogen pumping and starvation as a result of high current density are not discussed in their work. Also, the method presented by Tian et al. [54] is not suitable for the online monitoring of PEMFC when PEMFC is in operation. In fact, there is a need to detach the stack and conduct several tests to possibly diagnose whether the cell/stack is faulty or not. A very similar study is carried out by Khorasani et al. [55]. Niroumand et al. [56] conducted an experimental study and presented a method for research and development applications. In their work, the anode and cathode are supplied with hydrogen and nitrogen, while anode overpressure is preserved. They managed to identify the hydrogen leakage rate in a cell by measurement and analysis of pressure, temperature, humidity, flow, and OCV. Although the proposed method does not require any change in the stack structure, it is only limited to research and development applications and cannot be used for online diagnosis. In another study, Niroumand et al. [57] suggested that cathode output pressure oscillation around 0.14 Hz could be used as a diagnosis tool. PEMFC is supplied with cathode air supply step changes and pressure oscillation was observed in the voltage and cathode pressure. However, the type of fault is not discussed and error in experiment is not considered as a source of oscillation. Also, this method is not suitable for online failure diagnosis.

Recently Electrochemical Impedance Spectroscopy (EIS) signature analysis has been found to be useful for modeling and diagnoses of PEMFC faults [58]. Yan et al. [59] used EIS signature analysis methods to capture the transient behavior of a PEMFC by analyzing both voltage and current responses to a step-change in a resistive load. Mousa et al. [37] used EIS signatures for the first time to measure the amount of hydrogen crossover leakage in a commercial MEA at differential pressures between the anode and cathode. The oxygen starvation in the cathode side was detected by analyzing the effects of two datasets on the impedance signature. This EIS method has been extended to different multi-cell stack configurations to find the relationship between the hydrogen leak rate and reduced oxygen concentrations [60]. Eventually, Mousa [61] developed an ANN to obtain the amount of reduced oxygen to quantify hydrogen leakage.

All explained works [37,54–61] utilized non-model based methods to diagnose faulty cells since experimental observation/measurement/experiments were involved. There are a few works [62–65] that used ML methods to diagnose different types of faults in PEMFCs. However, to the best of knowledge, there are only two works [62,64] that attempted to diagnose hydrogen leakage and crossover from anode to cathode side. Liu

et al. [62] utilized a discrete hidden Markov model based on K-means clustering to diagnose six types of faults, including hydrogen leakage. They [62] used 150 kW Fcvelocity-HD6 PEMFC stack of Ballard Power Systems Inc. to conduct experiments and build the dataset, which is needed for K-means clustering. The only work that utilized “the combined model-based and non-model based approach” is conducted by Shao et al. [64]. They developed a dynamic model and validated their model with the experimental data in the literature. They used four ANNs with different configurations to diagnose four types of faults, including hydrogen crossover. It is necessary to mention that hydrogen crossover is modeled by a drop in oxygen level or, equivalently, a drop in current density. However, the ANN accuracies are low, and the leakage is not quantified in their work. In our work, we employed KNN and ANN estimators to detect and quantify the hydrogen leakage. These estimators are explained in Appendix C and Appendix D, respectively. Also, performance metrics for evaluating these estimators are explained in Appendix E.

## **2.5. Gap in Literature**

Sections 2.1 to 2.4 provided a literature review on related work to the thesis. Section 2.1 provided a review of different PEMFC modeling methodologies and explained that different models are developed for different purposes and different applications. Section 2.1 provided an understanding of why two models are developed in this work. One model is a CFD model, which is two-dimensional, steady-state, two-phase, and is used in an optimization process to obtain the optimal catalyst distribution. This model is not novel itself, but the combination with the optimization method is rather novel. The second model is a pseudo two-dimensional numerical model that can simulate fuel cell behavior in both driven and driving cases. The model is a continuation of the work developed by Vijayaraghavan et al. [15] and can model hydrogen pumping as a result of starvation for the first time in literature. This has the utmost importance and is a big step towards developing a diagnosis tool that not only can capture the hydrogen leakage but is able to quantify the hydrogen leakage and predict the hydrogen pumping occurrence.

Section 2.2 provided a summary of the literature on starvation with a focus on oxygen starvation. This section explained conditions that trigger starvation and discussed different degradation damages it could cause. The provided literature is mainly based on experimental tests that investigated the different categories of possible degradations. Section 2.2 provided an understanding of why it is important to prevent and diagnose

starvation faults in PEMFCs.

Section 2.3 provided a literature review on non-uniform catalyst distribution and the effect on PEMFC power density. So far, most of the models have investigated a few non-uniform cases and suggested that non-uniform catalyst distribution could improve PEMFC performance and efficiency. Most of the works in this realm only have focused on the effect of non-uniform catalyst distribution on PEMFC power density, while reactant distributions at the catalyst layer are not discussed. Therefore, there is a gap in the literature that should be covered. This work investigates the optimal catalyst distribution along the CCH that maximizes PEMFC power density and maximizes the minimum oxygen concentration along the catalyst layer. This optimization is conducted for the first time to not only maximize the power but delay the inception of oxygen starvation in the steady-state conditions.

Section 2.4 provides a literature summary of the works that have attempted to capture hydrogen crossover and hydrogen transfer leaks. A new category of failure diagnosis was introduced, which is based on the combination of model-based and non-model based methods. Almost all the literature in this area utilized experimental tests to measure and record the PEMFC characteristics in different operating conditions. The diagnosis models are mostly based on the observations of negative voltage or sudden intense voltage drop due to PEMFC being subjected to a sudden change in current, anode/cathode pressures, or fuel stoichiometry ratios. Some works conducted the same experiments but tried to attribute an impedance signature to hydrogen crossover fault. All these works require to physically detach stack and cells and conduct experimental tests to observe a faulty behavior or provide measurements to develop an impedance signature. However, in our work, and for the first time, a new category of models is introduced (the combination of model-based and non-model based) to provide an online diagnosis tool that can capture and quantify hydrogen leak transfer from anode to cathode. Our pseudo numerical model is employed to generate a dataset of steady-state responses of healthy/leaky cells. The dataset could be further expanded to dynamic data. The model is validated with data provided by Ballard corporation and could be used to accelerate the process of dataset creation. Besides, for the first time, hydrogen pumping is considered in the diagnosis tool, and the different ML methods are investigated to choose the most accurate method. The developed virtual hydrogen sensor not only could detect the presence of hydrogen leak in the cathode outlet but is able to quantify it. Developing a virtual sensor is a significant step towards the durability improvement of PEMFCs.

To summarize, the gap in literature are listed as follows:

- A relatively fast and precise steady-state and dynamic model that could simulate PEMFC behavior under the driving and driven modes by accounting for the hydrogen pumped to the cathode side
- Deriving optimal catalyst distribution with two objective functions (maximum performance and maximum delay in the inception of oxygen starvation)
- A novel hydrogen leak transfer diagnosis tool based on the combination of model-based and non-model based approaches
- Application of ML in capturing and quantifying the hydrogen leak transfer by considering the hydrogen pumping phenomenon

## **2.6. Research Motivation**

The main motivation of this thesis is to offer novel solutions that could remove or alleviate some of the current barriers, including the high cost of the ownership as well as insufficient lifetime and durability. The present study aims to address the gap in the literature listed in Section 2.5. by offering two solutions. The first solution is catalyst reconfiguration that could improve PEMFC performance and delay the oxygen starvation, and the second solution is to develop a combined model-based and non-model based virtual hydrogen sensor that detects the advent of a significant hydrogen leak causing potentially flammable emissions or smaller crossover leak levels to inform service staff that repairs are needed. Right now, it is possible to detect hydrogen leak transfer by placing a specific type of hydrogen sensor (e.g., KI Instruments Model FHD-752 (0–4%) hydrogen concentration sensor) in the cathode outlet. However, this sensor is expensive and is not reliable for long term use [61]. The big picture of this work is to build an add-on system for PEMFC devices to perform online monitoring of the system and to alarm the user in case of any fault, including hydrogen leakage. That would allow the user to change the defected cell and prevent further cell degradation and increase the lifetime of the fuel cell.

## Chapter 3.

### Optimal Catalyst Distribution as a Method to Enhance Performance and Durability

The power density of PEMFCs is affected by many parameters such as porosity, catalyst loading, liquid saturation, and operating conditions such as anode and cathode pressures, temperatures, fuel and oxidizer flow rates, and oxygen distribution along the active layer. The amount of available oxygen at the CCL is one of the key factors that determine the performance of the PEMFCs since oxygen molecules participate in ORR reaction and complete the electrochemical reactions, i.e., water generation. The oxygen distribution along the CCL is non-uniform due to the limitation of mass transfer mechanisms. At the CCH inlet, the oxygen concentration is higher, and a higher amount of oxygen molecules can diffuse through the CGDL and reach the CCL while the concentration of oxygen at the CCH outlet is lower and, therefore, a lower amount of oxygen molecules reach the CCL. Catalyst loading is another key factor that affects the ORR rate. Higher catalyst areas would result in a higher ORR rate while the less surface area would result in lower performance. Hence it would be possible to obtain the optimal catalyst distribution that could improve PEMFC power density while increasing the minimum oxygen concentration along the CCL through multi-objective optimization. This chapter starts with a two-dimensional, steady-state CFD model of the PEMFC cathode to calculate PEMFC power density and oxygen distribution along CCL. This model will be used in an optimization process to calculate the optimal catalyst distribution. The comparison indicates that non-uniform catalyst distribution could improve PEMFC power density.

#### 3.1. Mathematical Modeling

The numerical domain is shown in Figure 3-1. The numerical domain includes CCH, CGDL, and CCL. The humidified air enters the CCH from boundary AD with a constant velocity ( $u_{in}$ ) and reactant gasses leave the numerical domain from boundary BC.

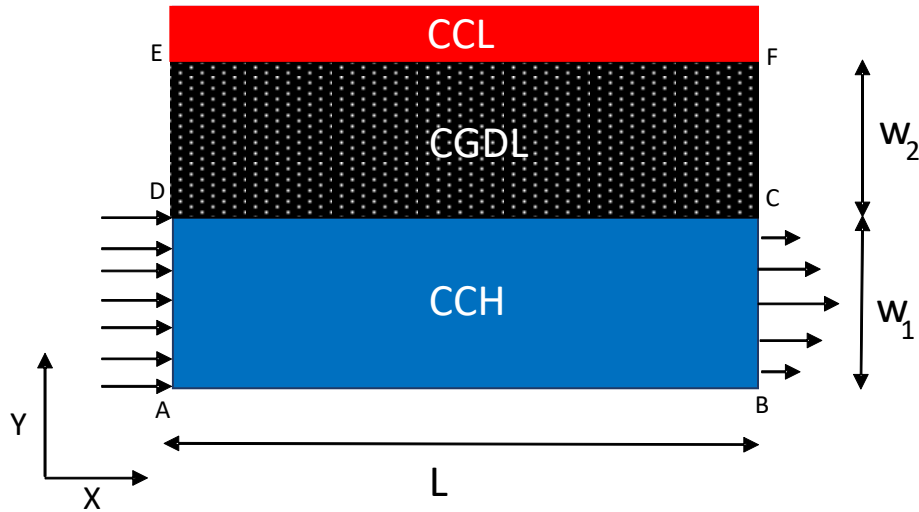


Figure 3-1. Numerical domain

Oxygen from the air diffuses through the CGDL to reach CCL. At the CCL, oxygen reacts with hydrogen ions coming from the anode side and produces water. This water is transported back through the CGDL. As the production of water increases, there is a potential for the water to saturate CGDL. Thus, the oxygen transfer resistance rise, and the electrochemical reaction rate drops. Hence the thesis uses a two-phase flow model to calculate PEMFC power density and oxygen distribution along the CCL. The multiphase mixture method is used to model the two-phase flow where the main idea is to model the mixture as a whole, rather than modeling each phase separately. Multiphase flow can be modeled by mass-averaging the mixture velocity and diffusive flux. The diffusive flux represents the difference between each phase velocity and the mass-averaged mixture velocity [66–69]. The model is developed based on the following assumptions:

- Anode side voltage losses are considered negligible comparing to the cathode side.
- Owing to the low velocity and low Reynolds number, the flow is laminar.
- The fuel cell is assumed to be in a steady-state condition.
- The catalyst layer is considered as an ultra-thin layer and only acts as a source/sink term in the electrochemical reaction.
- CGDL is considered as isotropic media.
- Half of the heat generated in CCL is transferred to the cathode side, while the other half is transferred to the anode side.

### 3.1.1. Governing Equations

In this section, the mathematical formulation of the multiphase mixture model will be discussed. In a multiphase mixture, a control volume contains both phases, and flow is modeled by a mass average mixture velocity and a diffusive flux. This kind of modeling offers several benefits, including [68,69]:

- The model is very similar to the single-phase theory, which would result in easier handling of both analytical and numerical solutions.
- The model requires fewer non-linear differential equations.
- In this model, equations are not developed for each phase separately. Therefore, there is no need to track the phase change interfaces.
- This model is very suitable for PEMFCs since equations in different layers are highly coupled.

We start the mathematical modeling by providing equations in each domain.

#### 3.1.1.1. CCH Equations:

The continuity equation is provided as follows [70]:

$$\varepsilon \frac{\partial \rho}{\partial t} + \nabla \cdot (\rho \vec{u}) = 0 \quad (3-1)$$

Any reduction in the mass due to condensation is nearly equal to the increase in the liquid phase mass. Therefore, there is no source/sink term required in Equation (3-1). Since the model is developed for steady-state mode,  $\partial \rho / \partial t = 0$ , and the continuity equation reduces as follow [70]:

$$\nabla \cdot (\rho \vec{u}) = 0 \quad (3-2)$$

The Navier-Stokes equation in the CCH is presented as follows [70]:

$$\frac{\partial (\rho \vec{u})}{\partial t} + \vec{u} \cdot \nabla (\rho \vec{u}) = -\nabla P + \nabla \cdot (\nabla \mu \vec{u}) \quad (3-3)$$

Once again, the transient term  $\partial (\rho \vec{u}) / \partial t = 0$ . Hence Equation (3-3) becomes:

$$\vec{u} \cdot \nabla(\rho \vec{u}) = -\nabla P + \nabla \cdot (\nabla \mu \vec{u}) \quad (3-4)$$

Here,  $\vec{u} \cdot \nabla(\rho \vec{u})$  represents the convection term. On the right-hand side,  $\nabla P$  represents the pressure gradient and  $\nabla \cdot (\nabla \mu \vec{u})$  represents the viscous term. It is important to note that  $\rho$  is the mixture density and  $\vec{u}$  is the mixture velocity vector.

### 3.1.1.2. CGDL Equations:

The continuity equation for CGDL is the same as the CCH and is expressed by Equation (3-2). A generalized Darcy's law [71] is used for the momentum conservation in the CGDL and is expressed by the following equation:

$$\frac{\partial(\rho \vec{u})}{\partial t} + \vec{u} \cdot \nabla(\rho \vec{u}) = -\nabla P + \nabla \cdot (\nabla \mu \vec{u}) - \frac{\mu}{K}(\epsilon \vec{u}) \quad (3-5)$$

In the steady-state, the equation becomes:

$$\vec{u} \cdot \nabla(\rho \vec{u}) = -\nabla P + \nabla \cdot (\nabla \mu \vec{u}) - \frac{\mu}{K}(\epsilon \vec{u}) \quad (3-6)$$

### 3.1.1.3. Species conservation Equations:

In order to obtain multiphase mixture equations, it is assumed that the control volume includes liquid, solid, and gaseous phases. The following parameters are used to derived unified conservation equations for all the domains [66,67].

$$\epsilon = \frac{V_{\text{pore}}}{V_{\text{total}}} \quad (3-7)$$

$$s_l = \frac{V_l}{V_{\text{pore}}} \quad (3-8)$$

$$s_g = \frac{V_g}{V_{\text{pore}}} \quad (3-9)$$

$$V_{\text{tot}} = V_{\text{pore}} + V_{\text{solid}} \quad (3-10)$$

$V_{\text{total}}$  is the volume of the control volume.  $V_{\text{pore}}$  is the void volume that can be filled by liquid and gaseous phases.  $V_l$  and  $V_g$  are the volume of the pore that is filled with liquid and gas phases respectively.  $\epsilon$  is porosity and defined as the ratio of pore volume the total



volume of the control volume. Liquid and gas saturations correspond to the volume ratio of the pore that is filled with liquid and gas, respectively. Mixture properties could be obtained from these parameters, as explained in Table 3-1.

You [72] utilized the parameters in Table 3-1 and derived the following equation for species conservation in the steady-state:

$$\begin{aligned} \nabla \cdot (\gamma \rho \vec{u} C) = & \nabla \cdot (\epsilon \rho D \nabla C) \\ & + \nabla \cdot \epsilon [(\rho_l s_l D_l (\nabla C_l - \nabla C) + (\rho_g s_g D_g (\nabla C_g - \nabla C))] \\ & - \nabla \cdot [C_l \vec{j}_l + C_g \vec{j}_g] \end{aligned} \quad (3-11)$$

Equation (3-11) must be written for oxygen, nitrogen, and water. In this equation,  $\gamma$  is the correction factor that modifies the species velocity by changing it from  $\vec{u}$  to  $\gamma \vec{u}$ .  $\gamma$  is calculated from the following equation [71,73,74]:

$$\gamma = \frac{\rho \sum_k \lambda_k C_k}{\sum_k \rho_k s_k C_k} \quad (3-12)$$

Table 3-1. Mixture properties equations, k denotes liquid and gas phases [67,71,73,74]

Mixture density	$\rho = \sum_k \rho_k s_k$	(3-13)
Mixture concentration (mass concentration)	$C = \frac{\sum_k \rho_k s_k C_k}{\rho}$	(3-14)
Mixture velocity	$\vec{u} = \frac{\sum_k \rho_k \vec{u}_k}{\rho}$	(3-15)
Mixture enthalpy	$h = \frac{\sum_k \rho_k s_k h_k}{\rho}$	(3-16)
Liquid enthalpy	$h_l = c_{pl} T$	(3-17)
Gas enthalpy	$h_g = c_{pg} T$	(3-18)
Effective conductivity	$K_{eff} = (1 - \varepsilon) K_{solid} + \varepsilon K_l + \varepsilon(1 - s) K_g$	(3-19)
Mixture diffusion coefficient	$D = \frac{\sum_k \rho_k s_k D_k^\alpha}{\rho}$	(3-20)
Mixture viscosity	$\nu = \frac{\nu_l \nu_g}{K_{rl} \nu_g + K_{rl} \nu_l}$	(3-21)
Liquid phase mobility	$\lambda_l = \frac{K_{rl} \nu_g}{K_{rl} \nu_g + K_{rl} \nu_l}$	(3-22)
Gas phase mobility	$\lambda_g = \frac{K_{rg} \nu_l}{K_{rl} \nu_g + K_{rl} \nu_l}$	(3-23)
Relative liquid phase permeability	$K_{rl} = s_l^3$	(3-24)
Relative gas phase permeability	$K_{rg} = s_g^3$	(3-25)

$j_k$  is diffusive max flux of phase (k) and can be formulated based on the traditional mixture theory that is provided as follows:

$$\rho_g \vec{u}_g = \vec{j}_g + \lambda_g \rho \vec{u} \quad (3-26)$$

$$\rho_l \vec{u}_l = \vec{j}_l + \lambda_l \rho \vec{u} \quad (3-27)$$

Also  $\vec{j}_l$  can be expressed as a function of capillary pressure [66,67]:

$$\vec{j}_l = K \frac{\lambda_l \cdot \lambda_g}{v} (\nabla P_c) \quad (3-28)$$

Capillary pressure is a difference between gaseous pressure and liquid pressure and can be expressed as an empirical function of saturation as follows [66,67]:

$$P_c = \sigma \cos(\theta_c) \left( \frac{\varepsilon}{K} \right)^{0.5} J(s_l) \quad (3-29)$$

where  $K$  is absolute permeability and  $J(s_l)$  is Leverett function [66,67]:

$$J(s_l) = \begin{cases} 1.147s_g - 2.12s_g^2 + 1.263s_g^3 & \theta_c < 90 \\ 1.147s_l - 2.12s_l^2 + 1.263s_l^3 & \theta_c > 90 \end{cases} \quad (3-30)$$

where  $\theta_c$  is the contact angle.

Now that all the parameters in Equation (3-11) are explained, we can write this equation for each species separately. We assume that the only liquid phase comes from water and the liquid mass fraction of water is one [66,67].

$$C_l^{O_2} = 0 \quad (3-31)$$

$$C_l^{N_2} = 0 \quad (3-32)$$

$$C_l^{H_2O} = 1 \quad (3-33)$$

Substituting Equation (3-31), Equation (3-32), and Equation (3-33) into Equation (3-11), we can derive the following equations for oxygen, nitrogen, and water conservation.

$$\nabla \cdot (\gamma_{O_2} \rho \vec{u} C^{O_2}) = \nabla \cdot (\epsilon \rho D_g^{O_2} \nabla C^{O_2}) - \nabla \cdot [C_g^{O_2} \vec{j}_g] \quad (3-34)$$

$$\nabla \cdot (\gamma_{N_2} \rho \vec{u} C^{N_2}) = \nabla \cdot (\epsilon \rho D_g^{N_2} \nabla C^{N_2}) - \nabla \cdot [C_g^{N_2} \vec{j}_g] \quad (3-35)$$

$$\begin{aligned} \nabla \cdot (\gamma_{H_2O} \rho \vec{u} C^{H_2O}) & \quad (3-36) \\ &= \nabla \cdot (\epsilon \rho D^{H_2O} \nabla C^{H_2O}) \\ &+ \nabla \cdot [\epsilon \rho_1 s_1 D_1^{H_2O} (-\nabla C^{H_2O}) + \epsilon \rho_g s_g D_g^{H_2O} (\nabla C_g^{H_2O} - \nabla C^{H_2O})] \\ &- \nabla \cdot [-\vec{j}_g + C_g^{H_2O} \vec{j}_g] \end{aligned}$$

We can simplify these equations further by investigating the gas-liquid phase equilibrium. Water condenses when the vapor partial pressure exceeds the saturation pressure at the specific temperature. The saturation pressure could be obtained as follows [72]:

$$\log_{10} P_{\text{sat}} = -2.1794 + 0.02953T - 9.1837 \times 10^{-5}T^2 + 1.4445 \times 10^{-7}T^3 \quad (3-37)$$

Based on the saturation pressure, different cases can be defined. If the water pressure is smaller than saturation pressure, water only exists in gaseous form. Phase change occurs when water pressure exceeds the saturation pressure. The summary of all cases are provided as follows:

$$s_1 = 0 \quad \text{if } P_{H_2O} < P_{\text{sat}} \quad (3-38)$$

$$C^{H_2O} = C_g^{H_2O} \quad \text{if } P_{H_2O} < P_{\text{sat}} \quad (3-39)$$

$$s_1 = \frac{\rho C^{H_2O} - \rho_g C_g^{H_2O}}{\rho_l - \rho_g C_g^{H_2O}} \quad \text{if } P_{H_2O} > P_{\text{sat}} \quad (3-40)$$

$$\rho C^{H_2O} = \rho_g (1 - s_1) C_g^{H_2O} + \rho_l s_1 \quad \text{if } P_{H_2O} > P_{\text{sat}} \quad (3-41)$$

and since  $C_1^{O_2} = C_1^{N_2} = 0$ , oxygen, and nitrogen concentrations could be derived as follows:

$$\rho C^{O_2} = \rho_g s_g C_g^{O_2} \quad (3-42)$$

$$\rho C^{N_2} = \rho_g s_g C_g^{N_2} \quad (3-43)$$

Using Equation (3-37)-Equation (3-43), we can simplify Equation (3-34)-Equation (3-36) for the two-phase flow as follows [72]:

$$\nabla \cdot (\gamma_{O_2} \rho \vec{u} C^{O_2}) = \nabla \cdot (\epsilon \rho D_g^{O_2} \nabla C^{O_2}) - \nabla \cdot \left[ \frac{\rho}{\rho_g s_g} C^{O_2} \vec{j}_g \right] \quad (3-44)$$

$$\nabla \cdot (\gamma_{N_2} \rho \vec{u} C^{N_2}) = \nabla \cdot (\epsilon \rho D_g^{N_2} \nabla C^{N_2}) - \nabla \cdot \left[ \frac{\rho}{\rho_g s_g} C^{N_2} \vec{j}_g \right] \quad (3-45)$$

$$\begin{aligned} \nabla \cdot (\gamma_{H_2O} \rho \vec{u} C^{H_2O}) &= \nabla \cdot (\epsilon \rho D_g^{H_2O} \nabla C^{H_2O}) - \nabla \cdot (\epsilon \rho_l D_g^{H_2O} \nabla s_l) \\ &\quad - \nabla \cdot \left[ \left( \frac{\rho_v^{H_2O}}{\rho_g} - 1 \right) \vec{j}_g \right] \end{aligned} \quad (3-46)$$

where the gas mixture density is

$$\rho_g = \frac{PM_g}{RT} \quad (3-47)$$

#### 3.1.1.4. Energy Equation:

The energy equation is provided as follows [75]:

$$\nabla \cdot (\gamma_h \rho \vec{u} h) = \nabla \cdot (K_{eff} \nabla T) + \nabla \cdot \left[ \sum_k (h_k \vec{j}_k) \right] + \dot{q} \quad (3-48)$$

$\gamma_h$  is the correction factor for energy advection and is defined as [75]:

$$\gamma_h = \frac{\rho \sum_k \lambda_k h_k}{\sum_k \rho_k s_k h_k} \quad (3-49)$$

$\dot{q}$  describes the heat release or adsorption due to phase change (i.e., condensation or evaporation) and is given by:

$$\dot{q} = h_{fg} \dot{m}_{fg} = h_{fg} \nabla \cdot (\rho_l \vec{u}_l) \quad (3-50)$$

$h$  and  $K_{eff}$  are given from Equation (3-16)-Equation (3-19).

### 3.1.1.5. Electrochemical equations:

The electrochemical current density is modeled through the traditional Butler-Volmer equation as follows [76–78]:

$$J = (1 - s_l) a_s J_C^{ref} \left( \frac{C^{O_2}}{C_{ref}^{O_2}} \right) \left[ e^{\frac{\alpha_c n F \eta}{RT}} - e^{-\frac{(1-\alpha_c) n F \eta}{RT}} \right] \quad (3-51)$$

where  $C^{O_2}$  is the oxygen concentration at the catalyst layer interface and  $C_{ref}^{O_2}$  is the reference oxygen concentration.  $(1 - s_l)$  represents part of the pore that is filled with liquid, and  $\eta$  represents overpotential. Output voltage ( $V$ ) and open-circuit voltage ( $V_{oc}$ ) are calculated as followings:

$$V = V_{oc} - R_{ohm} J - \eta \quad (3-52)$$

$$V_{oc} = 1.23 + \frac{RT}{4F} \ln \left( \frac{P_{H_2} P_{O_2}^{0.5}}{P_{H_2O}} \right) \quad (3-53)$$

### 3.1.2. Boundary Conditions:

Boundary AD is the cathode flow inlet, and velocities, temperature, and concentrations are known. These boundaries are listed as follows:

$$\begin{aligned} u = u_{in}, \quad v = 0, \quad T = T_0, \quad C^{H_2O} = C_{in}^{H_2O}, \quad C^{O_2} = C_{in}^{O_2}, \\ C^{N_2} = C_{in}^{N_2} \end{aligned} \quad (3-54)$$

Boundary BC is the cathode flow outlet, and outlet flow conditions are specified.

$$\frac{\partial u}{\partial x} = 0, \quad \frac{\partial v}{\partial x} = 0, \quad P = P_{\text{ref}}, \quad T = T_0, \quad \frac{\partial C^{O_2}}{\partial x} = 0, \quad \frac{\partial C^{H_2O}}{\partial x} = 0 \quad (3-55)$$

Boundaries DE and FC are walls. No-slip and symmetry boundary conditions are chosen. It is assumed that all the walls are kept in constant temperature, and the mass fluxes are equal to zero.

$$u = v = 0, \quad T = T_0, \quad \frac{\partial C^{H_2O}}{\partial x} = \frac{\partial C^{O_2}}{\partial x} = 0 \quad (3-56)$$

Similar boundary conditions are set for boundary AB (the horizontal wall)

$$u = v = 0, \quad T = T_0, \quad \frac{\partial C^{H_2O}}{\partial y} = \frac{\partial C^{O_2}}{\partial y} = 0 \quad (3-57)$$

Continuous boundary conditions are chosen between CGDL and CCH. At boundary EF, the horizontal component of velocity is assumed to be zero ( $u = 0$ ), and oxygen and water mass fluxes are calculated based on the current generated at the catalyst layer. These fluxes can be calculated as follows:

$$\dot{N}_{O_2} = \frac{M_{O_2}}{4F} J \quad (3-58)$$

$$\dot{N}_{H_2O} = \frac{-M_{H_2O}(1 + 2\alpha)}{4F} J \quad (3-59)$$

$\alpha$  is the water transfer coefficient and is taken as  $\alpha = 0.25$  [74]. The mixture vertical velocity can be calculated as follows:

$$\rho \epsilon v = \dot{N}_{O_2} + \dot{N}_{H_2O} \quad (3-60)$$

The species concentration gradient can be calculated as follows [74]:

$$-D \frac{\partial(\rho C_{O_2})}{\partial y} = \dot{N}_{O_2} - \gamma \rho \epsilon v C_{O_2} \quad (3-61)$$

$$-D \frac{\partial(\rho C_{H_2O})}{\partial y} = \dot{N}_{H_2O} - \gamma \rho \epsilon v C_{H_2O} \quad (3-62)$$

With regards to the thermal boundary condition, it is assumed that half of the heat generated due to voltage losses is transferred from the cathode to the anode side.

$$K_{eff} \frac{dT}{dy} = \frac{1}{2} (V_{oc} - V) J \quad (3-63)$$

### 3.1.3. Numerical Approach

The governing equations for continuity, momentum, and species equations were discretized by the finite volume method (FVM) [70]. The SIMPLE algorithm, TDMA solver, and the hybrid scheme [70] were employed to couple the gas mixture pressure-velocity equations. A two-dimensional C++ code is developed to conduct the simulations. Governing equations are then solved iteratively to satisfy the convergence criteria and to find the average current density and voltage. By changing the overpotential incrementally, different current densities and the polarization curve is obtained. A staggered grid is used to eliminate any unphysical oscillation in the pressure and velocity field. A mesh size with 21,600 cells (240\*90 in x-y directions) is selected. Appendix A provides more information about the solution method and explains the SIMPLE algorithm and the hybrid scheme. The numerical algorithm is provided in Figure 3-2.



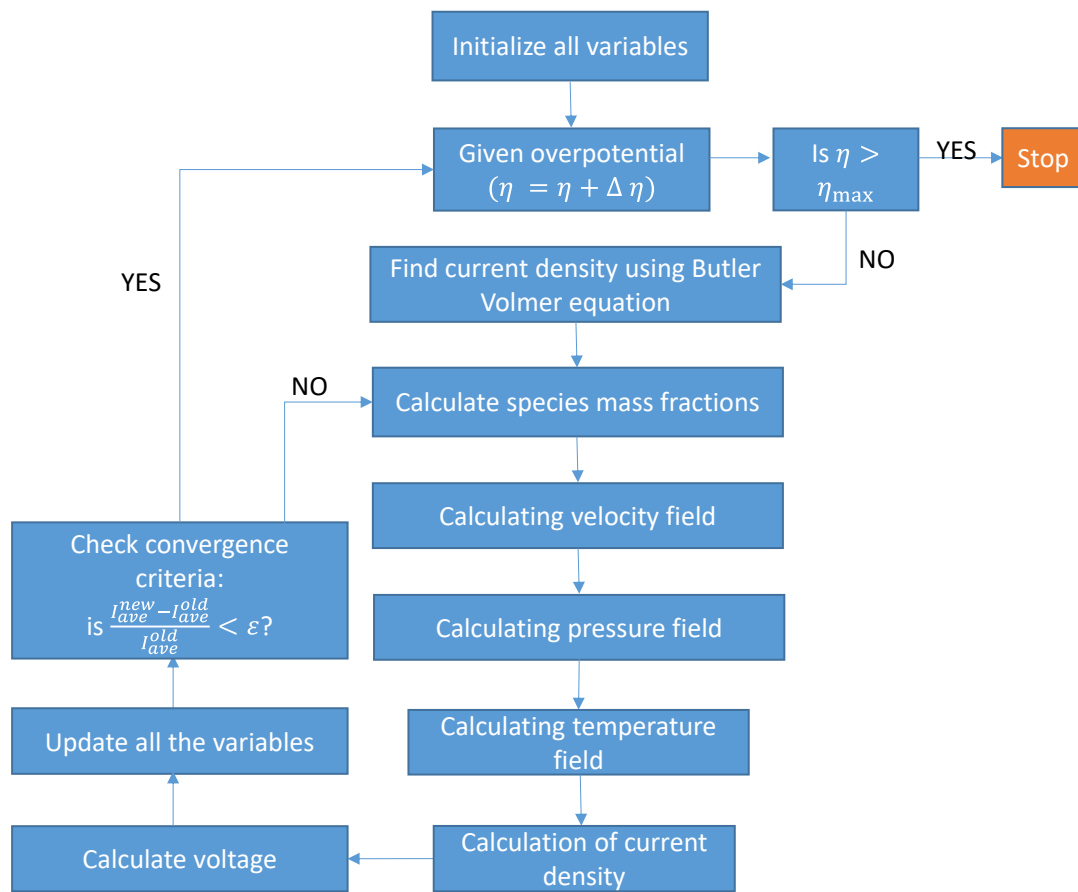


Figure 3-2. Numerical algorithm

Table 3-2. Supporting equations for the two-dimensional, two-phase cathode model

CCH length (cm)	7
CCH width (cm)	0.1
CGDL thickness (cm)	0.03
Gas diffuser porosity	0.4
Air velocity (m/s)	0.35
Air pressure (kPa)	304
Hydrogen pressure (KPa)	101
Catalyst surface area ( $\text{cm}^{-1}$ )	$1.4 \times 10^5$
Exchange current density ( $\text{A cm}^{-2}$ )	$4.84 \times 10^{-8}$
Cathode transfer coefficient	0.5
Ohmic resistance ( $\Omega$ )	0.115

#### 3.1.4. Model Validation and Grid Independency

Model validation is performed by comparing the polarization curve with the experimental data derived by You et al. [67].

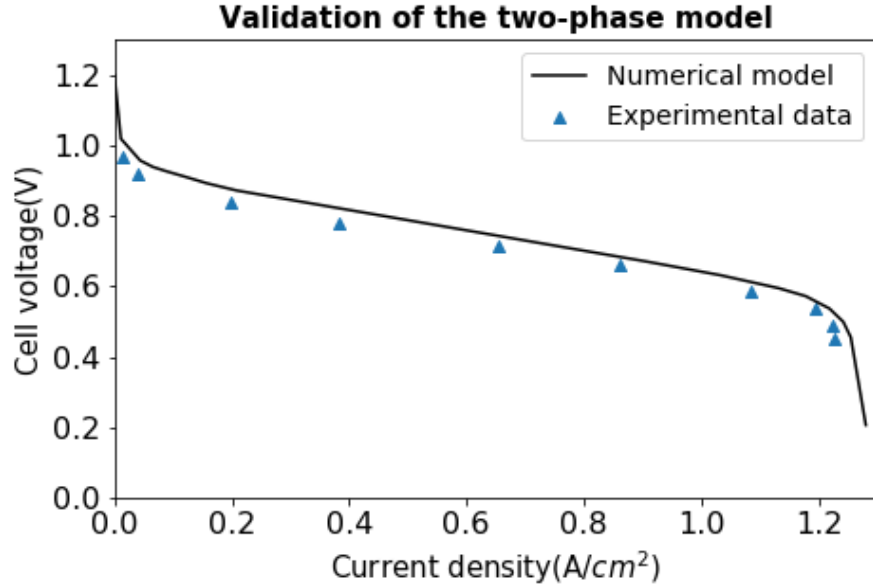


Figure 3-3. Validation of the two-phase model

As Figure 3-3 shows, the model is in good agreement with the experimental data. The difference between the model and the experimental data has several sources. For instance, the anode side is not modeled, and anode losses are not considered. Also, membrane and water transport in the membrane are not modeled, and the value of net water transport  $\alpha$  is assumed rather than be calculated. Nonetheless, the model is able to predict the PEMFC behavior with good precision. In addition, the simulation is conducted on different mesh sizes to assure that that the results are grid-independent. Figure 3-4 depicts current density distribution along the CGDL/CCL interface for different mesh sizes. As it is shown in this figure, by changing the grid size from 240\*90 to 480\*128, the results do not change, and the red line lies on the blue line. In addition, it has been seen that by changing the mesh size from 240×90 grid to 480 ×128 grid, the maximum power density is changed by less than 0.1%. Table 3-3 provides the grid independency analysis for different overpotential values. The values for current density and power densities are provided and compared.

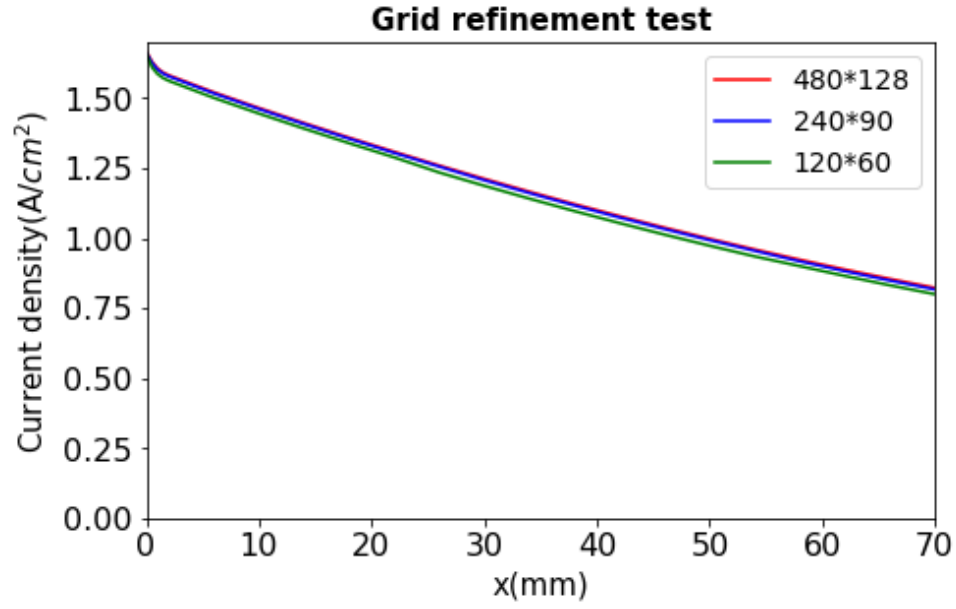


Figure 3-4. Effect of mesh size on current density distribution at the CGDL/CCL interface at  $\eta=0.33$  V

Table 3-3. The grid independence test

Grid size	120×60	240×90	480 ×128
$\eta=0.2$ V	$J=0.0011 \frac{A}{cm^2}$	$J=0.011 \frac{A}{cm^2}$	$J=0.011 \frac{A}{cm^2}$
	$P=0.011 \frac{W}{cm^2}$	$P=0.011 \frac{W}{cm^2}$	$P=0.011 \frac{W}{cm^2}$
$\eta=0.4$ V	$J=1.139 \frac{A}{cm^2}$	$J=1.241 \frac{A}{cm^2}$	$J=1.242 \frac{A}{cm^2}$
	$P=0.618 \frac{W}{cm^2}$	$P=0.620 \frac{W}{cm^2}$	$P=0.621 \frac{W}{cm^2}$
$\eta=0.8$ V	$J=1.281 \frac{A}{cm^2}$	$J=1.284 \frac{A}{cm^2}$	$J=0.285 \frac{A}{cm^2}$
	$P=0.266 \frac{W}{cm^2}$	$P=0.267 \frac{W}{cm^2}$	$P=0.267 \frac{W}{cm^2}$

### 3.2. Catalyst Distribution Modeling

Now that the model is validated, it can be used to investigate the effect of non-uniform catalyst distribution on oxygen distribution and the generated power density. In order to model the effect of non-uniform distribution, a nonlinear term will be added to the Butler-Volmer equation, i.e., Equation (3-51). In this equation,  $a_s$  represents the total catalyst surface area per unit volume of cathode CCL. This value is related to catalyst loading ( $m_{pt}$ ), which is the amount of platinum used in the area unit. The relation between  $a_s$  and  $m_{pt}$  is provided as follows:

$$a_s = a_0 m_{pt} \quad (3-64)$$

In Equation (3-64),  $a_0$  represents the total catalyst surface area per unit mass of catalyst. Replacing Equation (3-64) into Equation (3-51), Equation (3-65) is derived.

$$J_C = (1 - s_l) a_0 m_{pt} j_C^{ref} \left( \frac{C_{O_2}}{C_{ref}^{O_2}} \right) \left[ e^{\frac{\alpha_C n F \eta}{RT}} - e^{\frac{-(1-\alpha_C) n F \eta}{RT}} \right] \quad (3-65)$$

It is assumed that the catalyst loading is proportionally related to the amount of platinum used in the catalyst layer. Therefore, the non-uniform catalyst loading is modeled by multiplying catalyst loading in a non-linear function ( $h(\bar{x})$ ). Therefore, Equation (3-65) can be written as follows:

$$J_C = (1 - s_l) a_0 m_{pt} h(\bar{x}) j_C^{ref} \left( \frac{C_{O_2}}{C_{ref}^{O_2}} \right) \left[ e^{\frac{\alpha_C n F \eta}{RT}} - e^{\frac{-(1-\alpha_C) n F \eta}{RT}} \right] \quad (3-66)$$

where  $\bar{x}$  is the dimensionless length and can be obtained as follows:

$$\bar{x} = \frac{x}{l} \quad (3-67)$$

$l$  is the length of the CCH and is equal to 70mm in the model. The distribution function is assumed as a polynomial function and can be written as:

$$h(\bar{x}) = f_n \bar{x}^n + f_{n-1} \bar{x}^{n-1} + \dots + f_1 \bar{x} + f_0 \quad (3-68)$$

In the case of uniform catalyst distribution,  $f_0 = 1$  and  $f_i = 0$  for  $i > 0$ . There are two constraints on the distribution function that are stated as follows:

- The fixed total amount of catalyst; in order to compare the effect of non-uniform catalyst distribution, it is important to fix the total amount of catalyst. This constraint can be modeled as follows:

$$\int_0^1 h(\bar{x}) dx = 1 \quad (3-69)$$

Equation (3-69) assures that the total amount of catalyst loading is kept constant. Substituting  $h(\bar{x})$  from Equation (3-68) into Equation (3-69) would give us the following equation:

$$\int_0^1 (f_n \bar{x}^n + f_{n-1} \bar{x}^{n-1} + \dots + f_1 \bar{x} + f_0) dx = 1 \quad (3-70)$$

This yields the following relationship:

$$f_0 = \sum_{k=1}^n \frac{-f_k}{k+1} \quad (3-71)$$

- Positive catalyst distribution; negative catalyst distribution does not have any physical meaning and therefore:

$$h(\bar{x}) \geq 0 \quad (3-72)$$

### 3.3. Effect of Non-Uniform Catalyst Distribution

In this part, the effect of non-uniform catalyst distribution for two cases is investigated. The purpose of this investigation is to see how non-uniform catalyst distribution could affect oxygen concentration and current density distributions. The main idea is based on the fact that the oxygen concentration distribution along the CCH is non-uniform, and since the oxygen concentration is higher at the CCH input, loading more catalysts at the flow inlet and less at the outlet could improve efficiency and also increase the minimum oxygen concentration. As a result, the non-uniform catalyst distribution could increase the maximum current density and delay oxygen starvation. At low current densities, the species mass transfer losses are not highly remarkable. However, at high current densities, concentration reduction along the CCH is higher, and the loss is more noticeable. The first case is the uniform catalyst distribution where  $h(\bar{x}) = 1$  and the second case is the linear function where  $h(\bar{x}) = 1.5 - \bar{x}$  which indicates more catalyst loading at the entrance and less at the outlet. Figure 3-5 and Figure 3-6 provided the oxygen distribution contours for uniform and non-uniform catalyst distribution cases, respectively. The activation overpotential for both cases is  $\eta=0.33$ .

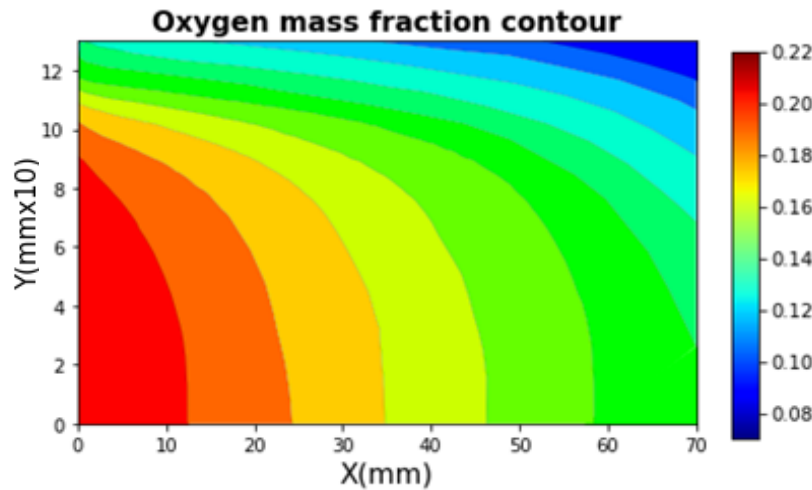


Figure 3-5. Oxygen mass fraction distribution for uniform catalyst distribution at  $\eta=0.33$  V

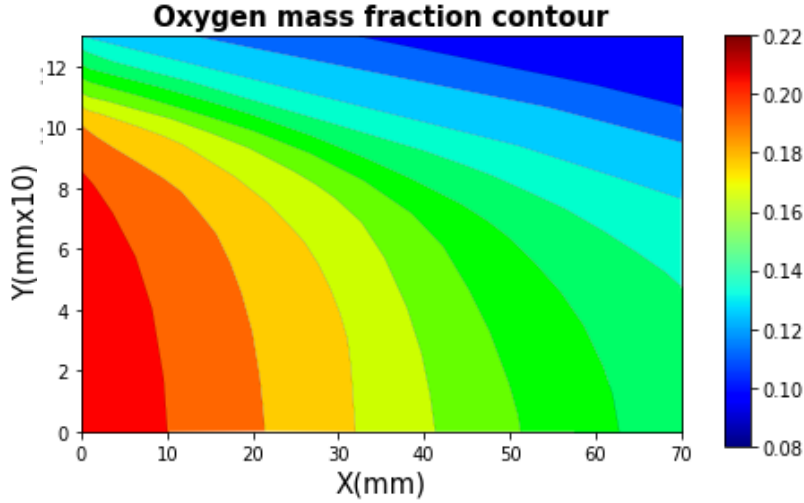


Figure 3-6. Oxygen mass fraction distribution for non-uniform catalyst distribution at  $\eta=0.33$  V

Figure 3-5 shows that even in uniform catalyst distribution, oxygen distribution at CCL/CGDL is non-uniform, and the mass fraction changes from about 0.14 to 0.07. The oxygen concentration distribution is a decreasing function due to mass transfer limitations. Since the oxygen concentration is higher at the CCH inlet, it is easier for oxygen particles to diffuse through CGDL and reach CCL. Figure 3-6 shows a different oxygen distribution at the CCL. The distribution is less non-uniform, with a maximum of 0.125 at the CCH inlet and a minimum of 0.08 at the outlet. That is because loading more catalysts at the CCH inlet results in more oxygen participating in ORR, and therefore the concentration drops from 0.14 to 0.125 while at the outlet, less oxygen participates in ORR and therefore the less oxygen is consumed and the minimum oxygen mass fraction increases from 0.07 to 0.08. Figure 3-7 provides a comparison between oxygen profiles at the catalyst layer for both cases as follows:



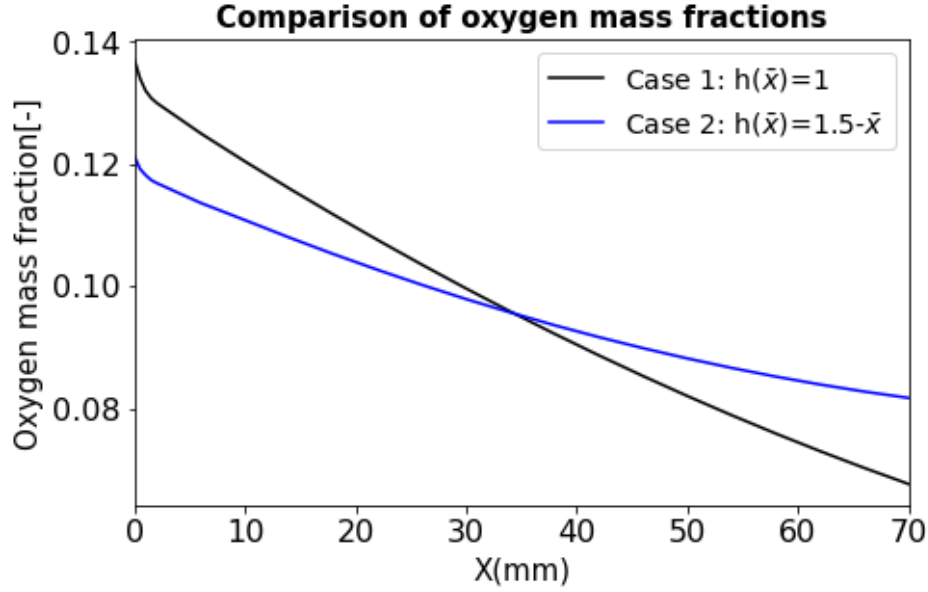


Figure 3-7. Comparison of oxygen distributions at CCL for two cases of catalyst distributions ( $\eta = 0.33 \text{ V}$ )

Looking at Figure 3-7, the average oxygen mass fraction along the CCL is lower for the non-uniform case; however, the minimum oxygen mass fraction is increased. Figure 3-8 provides a comparison between the current density distributions between these two cases:

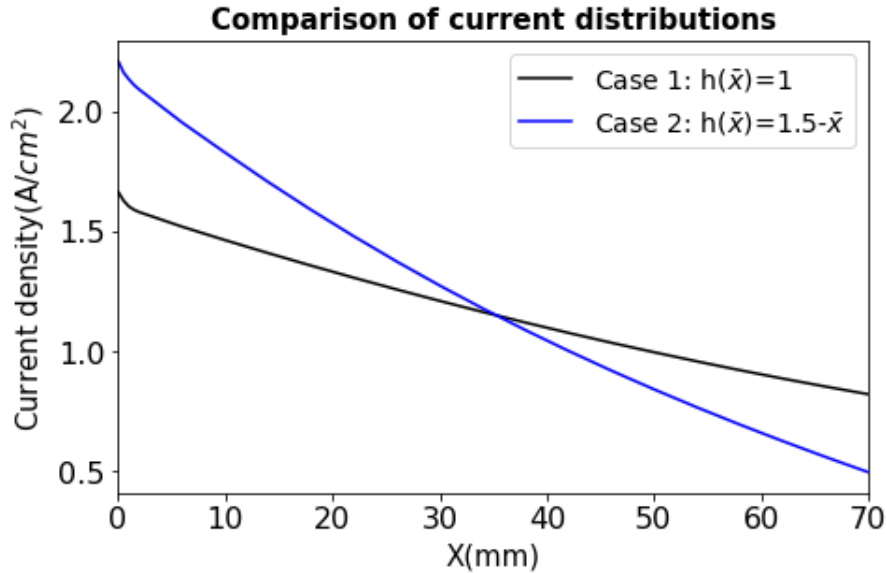


Figure 3-8. Current density distributions at CCL for two cases of catalyst distributions ( $\eta = 0.33 \text{ V}$ )

In this figure, the average current density for non-uniform catalyst distribution is  $1.27 \frac{\text{A}}{\text{cm}^2}$  and is higher than the average current density for the uniform catalyst distribution

( $1.18 \frac{A}{cm^2}$ ). In fact, we can compare the average current densities by comparing the area under each curve. Figure 3-9 shades three different areas to illustrate a comparison between the uniform and non-uniform catalyst distribution.

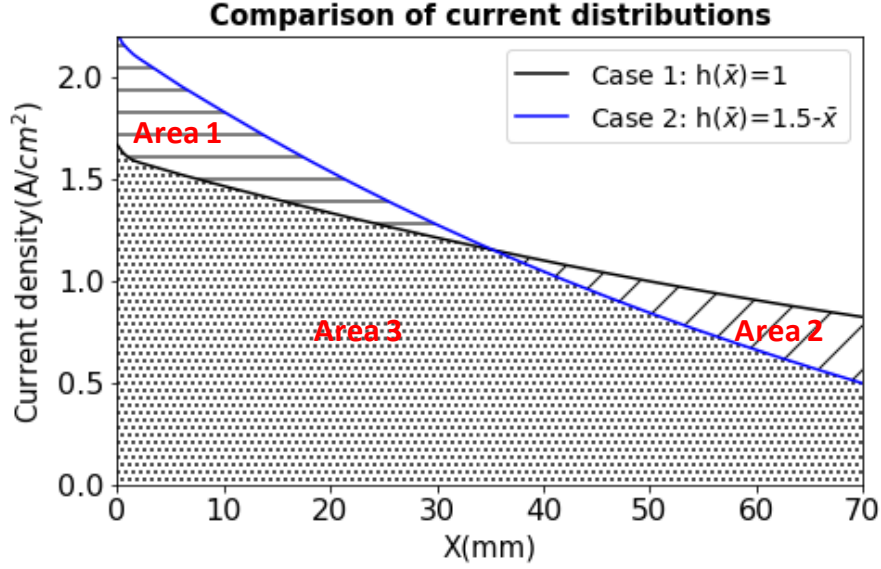


Figure 3-9. current density distributions Comparison between two cases of catalyst distributions ( $\eta = 0.33 V$ )

As it is seen in Figure 3-9, Area 1 indicates the increase in the current density due to inserting more catalyst at the CCH entrance, while Area 2 indicates the current density reduction due to inserting less catalyst at the end of the CCH. Area 3 is common between both cases. Since area 1 is slightly larger than area 2, it can be inferred that using a non-uniform catalyst layer can improve PEMFC efficiency and, at the same time, increases the minimum oxygen concentration along the catalyst layer, which increases the maximum current density and delays the inception of oxygen starvation. Another interesting observation is that flattening the current density profile would not necessarily improve the system performance while flattening oxygen distribution might result in better performance.

In the next step, we compare the values of the maximum liquid saturation obtained from the model. The reason for this comparison is the presence of  $(1 - s_l)$  term in the Butler-Volmer equation (Equation (3-51)). The presence of liquid water reduces the active surface area of the catalyst layer, and it is modeled by  $(1 - s_l)$ . Maximum liquid water saturation in the case of uniform catalyst loading (case 1) is found to be about 0.033, while this is increased to more than 0.037 in the case of employing a non-uniform catalyst

loading. The average liquid water saturation slightly increases, but it does not significantly deteriorate the performance of PEMFC due to the formation of the two-phase flow.

Figure 3-10 provides a comparison between temperature distribution between the two introduced cases. Saturated water pressure highly depends on temperature, and therefore, it can influence liquid water distributions. Besides, the increasing temperature would decrease activation loss and hence improves PEMFC efficiency. On the other hand, very high temperatures can harm the membrane and reduce its lifetime. Therefore, it is important to monitor PEMFC temperature and conduct proper heat management to assure PEMFC high-performance. As Figure 3-10 shows loading more catalysts at the CCH entrance would result in higher temperatures due to a higher ORR rate. However, the temperature gradient does not change significantly, which means that the non-uniform catalyst distribution would not result in a noticeable change in the temperature profile.

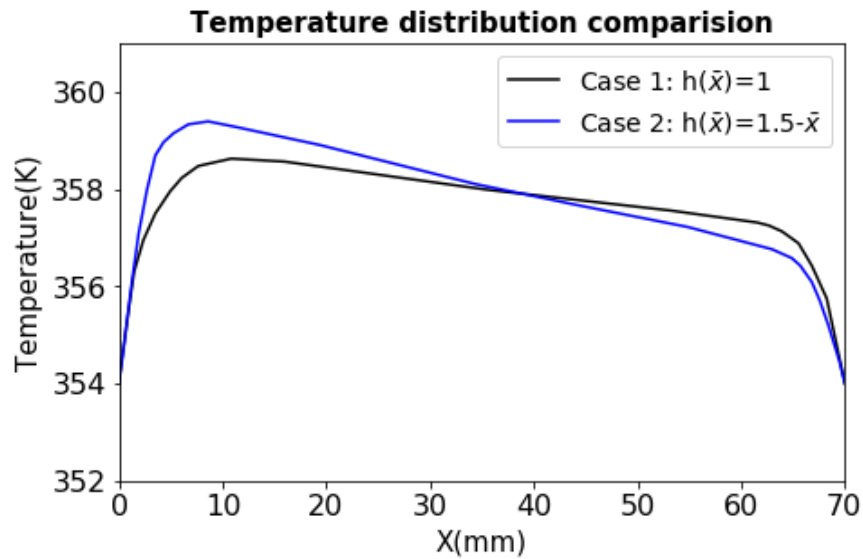


Figure 3-10. Temperature distributions Comparison between two cases of catalyst distributions ( $\eta = 0.33 V$ )

In the next section, an optimization procedure will be defined to find the optimal catalyst distribution that results in maximum PEMFC power density and, at the same time, maximizes the minimum oxygen mass concentration at the CCL in the longitudinal direction.

### 3.4. Optimization of Catalyst Distribution

In this section, the numerical model and genetic algorithm are combined in order to find the optimal catalyst distribution. Catalyst distribution is assumed as a polynomial function with unknown coefficients, and these coefficients are found through the optimization procedure. The first objective function is the maximum PEMFC power density. The second objective function is the minimum oxygen concentration along the CCL at the current density that maximum PEMFC power density occurs. The optimization problem is to maximize both objective functions by finding the optimal catalyst distribution coefficients. Objective functions, constraints, and decision variables are defined as follows:

Maximize (objective function 1 and objective function 2) ,  
 $f_k \in \mathbb{R}$

Objective function 1 = Maximum PEMFC power density for  $J = 0$  to  $J_{lim}$  (3-73)

Objective function 2 (3-74)  
 = Minimum oxygen concentration @CCL for  $J_{Maximum\ PEMFC\ power\ density}$

Constraints =  $\begin{cases} \text{CFD model, Equation 3 – 1 to Equation 3 – 66} \\ \text{Equation 3 – 69} \\ \text{Equation 3 – 72} \end{cases}$

Decision variables:  $f_k, k = 1, 2, \dots, n$

Figure 3-11 provides the optimization algorithm:

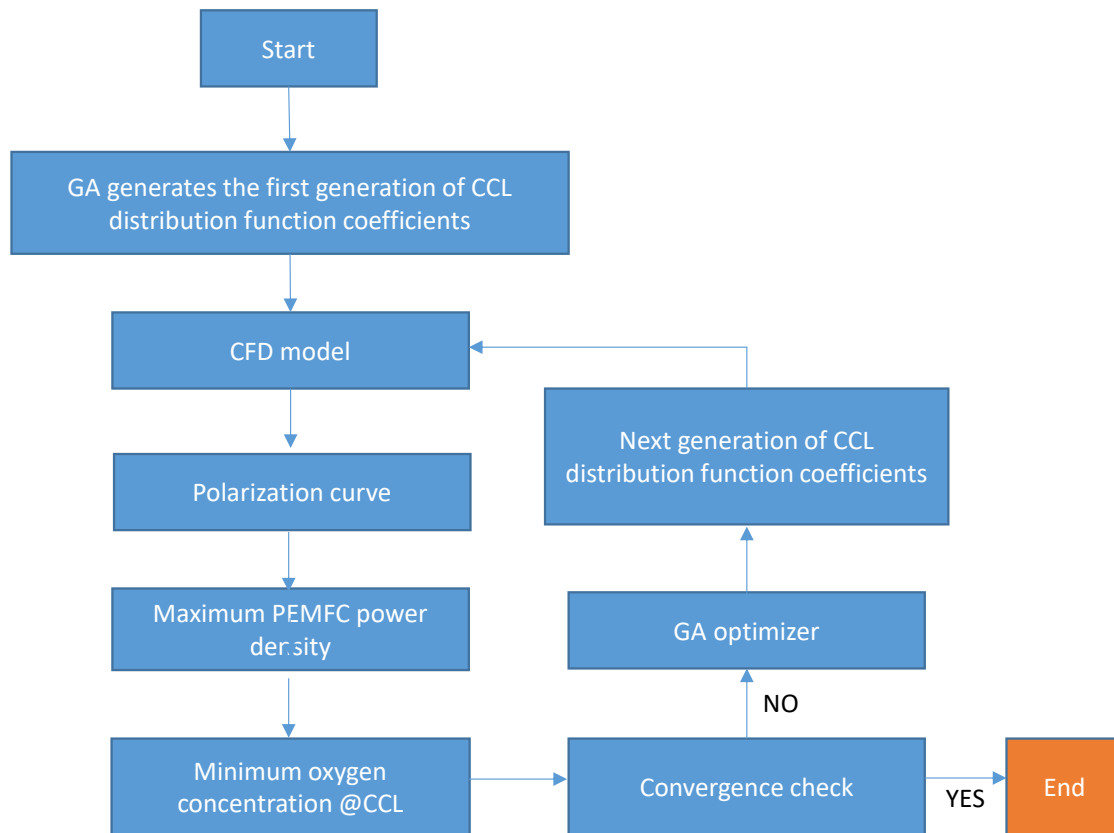


Figure 3-11. Optimization procedure to find the optimal catalyst distribution

A brief explanation of the GA algorithm is provided in Appendix B. The parameters that are used in the genetic algorithm are defined in Table 3-4.

Table 3-4. Optimization algorithm parameters

Parameters	Value
Population size	For three unknown or less=100  For more than three unknown= 500
Lower bound	-20 for all parameters
Higher bound	20 for all parameters
Number of variables	2 to 6
Elite count	0.05*population size
Crossover ratio	0.8
Mutation ratio	0.05
Selection function	Roulette
Mutation function	Uniform
Function tolerance	1e-6
Time limit	-

Following considerations are made to assure that the constraints are satisfied:

- The constant coefficient ( $f_0$ ) is found based on Equation (3-71) to assure that the total amount of catalyst is kept constant.
- Two strategies are chosen to ensure that the catalyst distributions stay positive. The first scenario is to simply replace the sample point that violates this constraint with another random point. The second scenario is to set the objective function value to a positive number equal to the area under the x-axis. Since the objective function values of feasible points are negative, setting a positive value for infeasible points reduces the chance of that point to move to the next generation.

Both of these scenarios are attempted, and GA has run many times to assure that the obtained answer is the optimum answer. Pareto frontiers are found for linear and quadratic polynomial distributions. However, only one optimal answer is found for third and higher degree polynomials. For linear and quadratic polynomials, the optimal answer that resulted in maximum power density is chosen and along with other results, are reported in Table 3-5. The improvement percentages are provided based on the comparison of each case with the base case (uniform distribution). Figure 3-12 also provides the optimal catalyst distributions. As Figure 3-12 shows, increasing the degree of the polynomial function from five to six does not change the optimal distribution. By calculating the area under the optimal catalyst distribution, it can be inferred that the amount of catalyst used in the first half of the CCL is almost two times larger than the amount of the catalyst loaded in the rest of CCL. Figure 3-13 and Figure 3-14 provides a comparison between oxygen mass fractions and current distributions along the CCL at  $\eta=0.33$ .

Table 3-5. Optimal catalyst distribution functions and improvement percentages

Polynomial degree	Coefficients	Maximum PEMFC power density improvement	Minimum oxygen concentration improvement	Maximum current density improvement
Linear	$f_1 = -2,$ $f_0 = 2$	7%	18.1%	4.4%
2 <sup>nd</sup> order	$f_2 = 2.214,$ $f_1 = -3.845,$ $f_0 = 2.185$	10%	27.5%	6.2%
3 <sup>rd</sup> order	$f_3 = -1.66,$ $f_2 = 4.68,$ $f_1 = -4.76,$ $f_0 = 2.24$	11%	33%	6.9%
4 <sup>th</sup> order	$f_4 = 5.53,$ $f_3 = -12.6,$ $f_2 = 11.36,$ $f_1 = -6,$ $f_0 = 2.26$	12 %	36.5%	7.45%
5 <sup>th</sup> order	$f_5 = -1.9,$ $f_4 = 9.44,$ $f_3 = -15.1,$ $f_2 = 11.8,$ $f_1 = -6,$ $f_0 = 2.27$	12.6%	42%	7.8%



6 <sup>th</sup> order	$f_6 = 0,$ $f_5 = -3.66,$ $f_4 = 13.88,$ $f_3 = -19,$ $f_2 = 13.23,$ $f_1 = -6.2,$ $f_0 = 2.27$	12.6.%	42%	7.8%
-----------------------	---	--------	-----	------

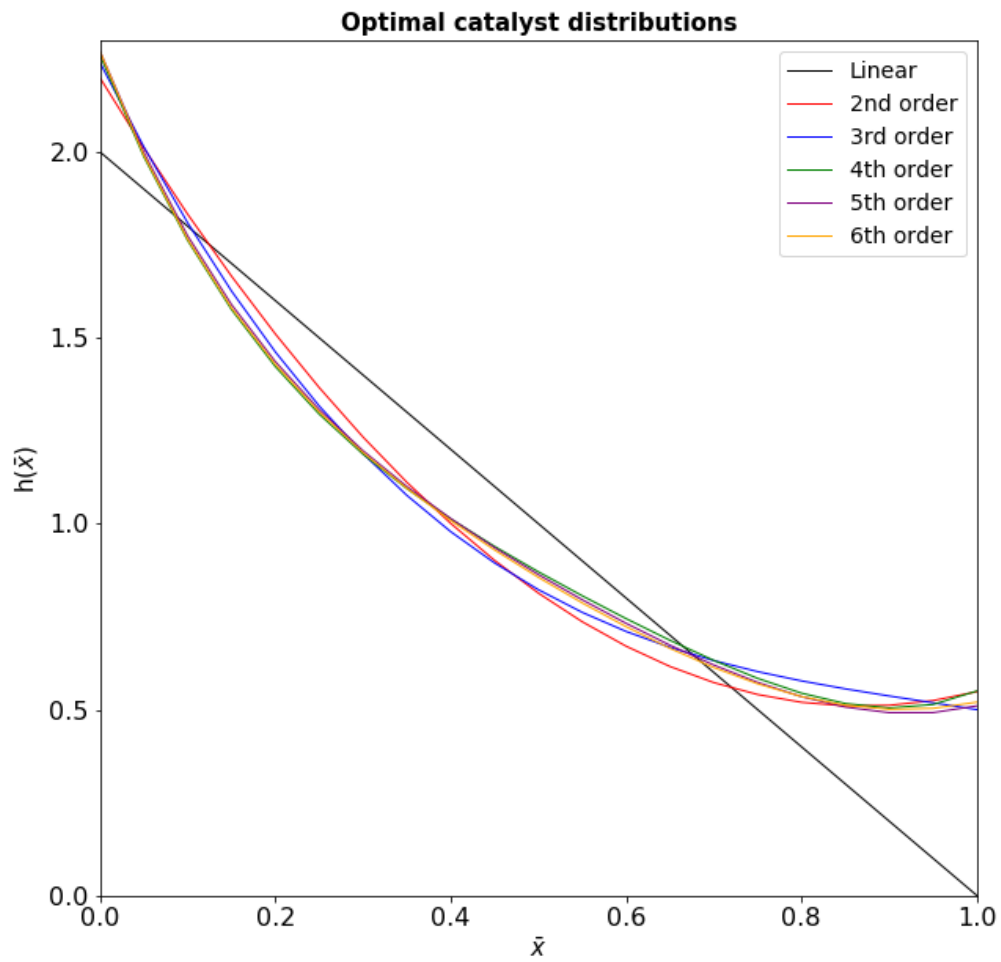


Figure 3-12. Optimal catalyst distributions

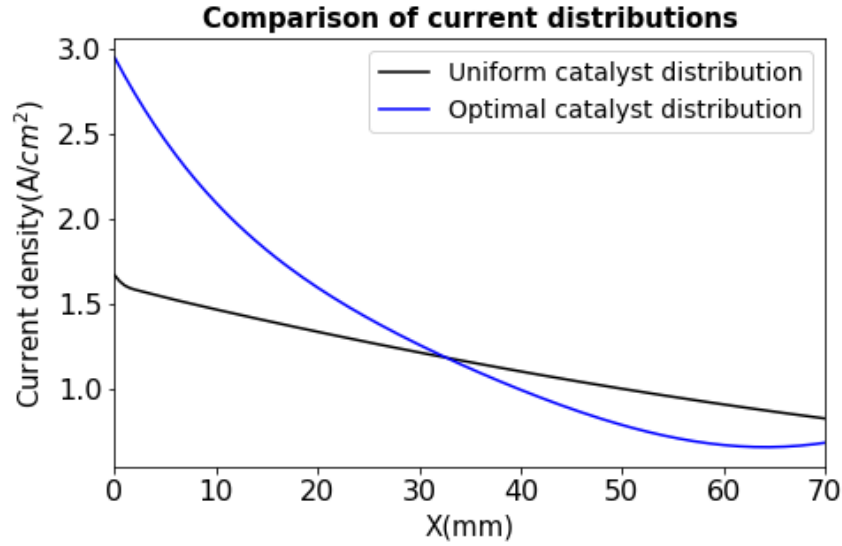


Figure 3-13. Comparison of current distribution between uniform and optimal catalyst distributions at  $\eta = 0.33 \text{ V}$

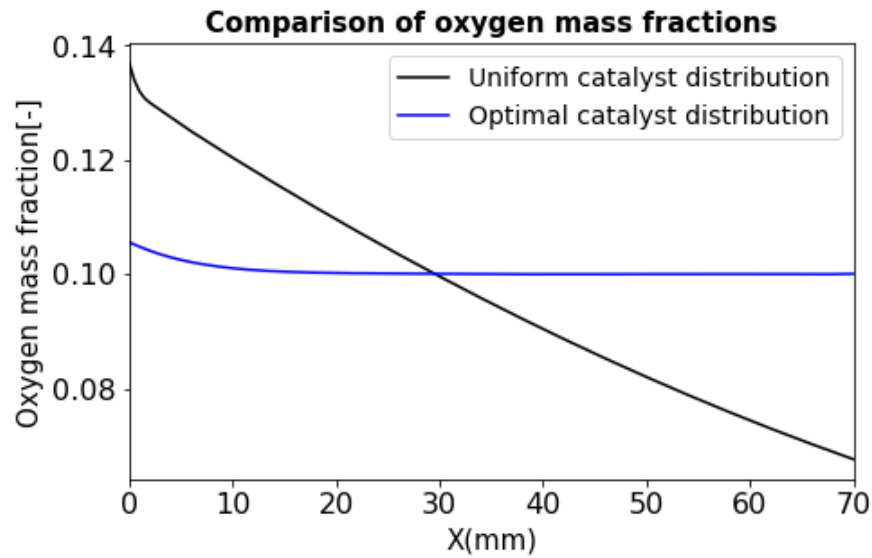


Figure 3-14. Comparison of oxygen mass fraction distributions between uniform and optimal catalyst distributions at  $\eta = 0.33 \text{ V}$

Calculating the area under the current density distributions in Figure 3-13. shows that the amount of current generated at  $\eta=0.33$  is about 12% higher compared to the uniform case, which is a noticeable improvement in PEMFC power density. At the same time, Figure 3-14 indicates that oxygen distribution is flattened, and the minimum amount of oxygen mass fraction is increased from 0.07 to 0.1, which is almost 42%. This noticeable increase in the minimum oxygen mass fraction along the catalyst layer indicates that the maximum current density would increase, which means that oxygen starvation occurs in higher

current densities. Figure 3-15 and Figure 3-16 provide a comparison between polarization and power density curves in uniform and optimal case. The maximum current density improves from  $1.28 \frac{A}{cm^2}$  to  $1.38 \frac{A}{cm^2}$  which is about 7.8% improvement.

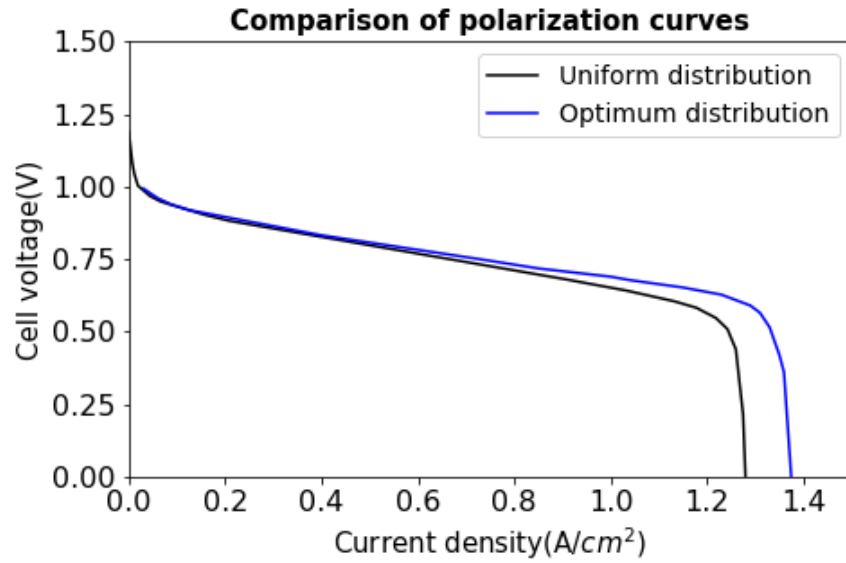


Figure 3-15. Comparison between polarization curves between uniform and optimal catalyst distribution cases

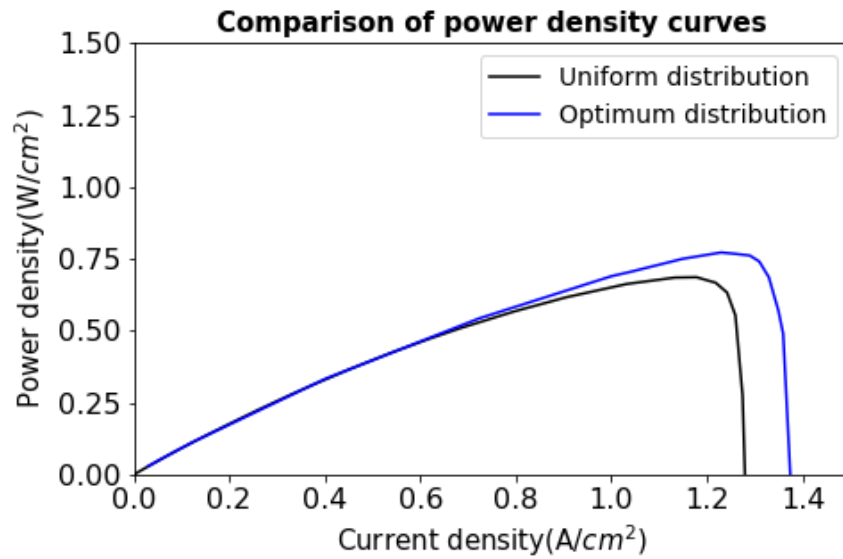


Figure 3-16. Comparison between polarization curves between uniform and optimal catalyst distribution cases

### 3.5. Chapter Summary

In this chapter, a two-dimensional, two-phase, steady-state model is developed to investigate the effects of platinum loading distribution on oxygen distribution at CCL and, therefore PEMFC power density. In the first step, two cases of catalyst distributions are introduced, and an increase in the minimum oxygen concentration and maximum PEMFC density is observed. Next, an optimization procedure is introduced to find the optimal catalyst distributions. Objective functions, constraints, and variables are explained, and GA is selected as the optimizer. Catalyst distributions are modeled as polynomials with unknown coefficients. These coefficients are obtained through the optimization procedure, and the following results are observed:

- In the optimal case, maximum PEMFC power density is improved by 12.6%.
- In the optimal case, the minimum oxygen mass fraction along the CCL is increased by 42%
- In the optimal case, the maximum current density is increased by 7.8%.
- In the optimal case, the oxygen mass fraction is flattened along the CCL.
- The optimum answers for both objective functions are the same, which results in one optimal distribution than a Pareto frontier.
- Loading more catalyst in locations with higher reaction rates improves PEMFC power density.
- The amount of catalyst used in the first half of the catalyst layer is almost twice of the other half.
- An unlimited increase of the platinum mass loading at the CCH inlet and an unlimited decrease in the CCH outlet would not result in the maximum PEMFC power density.
- The increase in the maximum current density in the optimal case indicates that oxygen starvation would occur at a higher current density.

Also, the results are consistent when pure oxygen is used for the simulations [79]. In the next chapter, a simple pseudo two-dimensional model is developed as a based model for diagnosis purposes.

## Chapter 4.

### Developing a Base Model for Leakage Diagnosis

Transfer (crossover) leaks initiated by the physical and chemical deterioration of the MEA are among the primary life-limiting factors in PEMFCs. The leaks result in reduced oxygen levels in affected cells, which could result in hydrogen pumping and hydrogen emission in case of complete oxygen starvation. This chapter builds on previous work presented in Vijayaraghavan et al. [15], that had developed a unified fuel cell model to predict cell voltage behavior under driving (normal) and driven (oxygen-starved) conditions. This work explicitly includes hydrogen pumping and emissions release when operating under oxygen-depleted conditions. The developed model would be used as a base model for the diagnosis tool that will be used to detect and quantify leakage in PEMFC. The based model must be fairly fast and precise since we plan to run this model for a wide range of operating conditions and for different leakage values to make a considerably large dataset. The dataset would be used to train ML estimators to predict and quantify the amount of leakage based on current, voltage, and other operating conditions. Therefore, the computational cost is a very important factor that must be considered. Using the CFD model from the previous chapter would result in a huge computational cost and could result in weeks of processing time. It is also important to note that the ultimate purpose of this work is to include the effects of other faults in the model. Therefore, the dataset must be generated again, and ML methods must be trained again to isolate and quantify the new faults added to the model along with the previous faults. In this case, using a detailed CFD model is not a feasible option, and that is why the pseudo numerical model is introduced and developed. Developing this hybrid analytical-numerical model reduces computational complexity noticeably and improves computational efficiency.

#### 4.1. Mathematical Model

This section presents the mathematical model of the fuel cell that will be used in a finite element solver in Section 4.2. The numerical domain is shown in Figure 4-1.

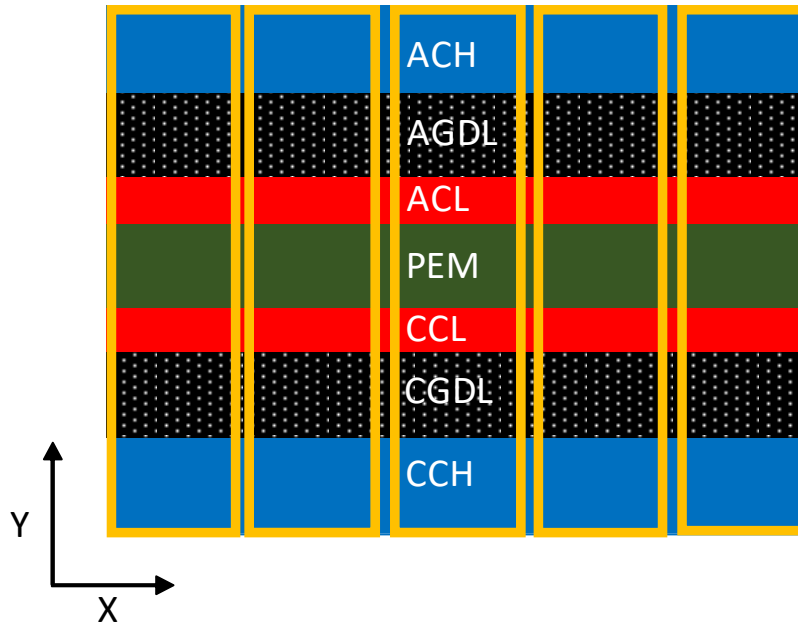


Figure 4-1. Numerical domain of the pseudo two-dimensional model developed for diagnosis purposes

The main model assumptions are listed as follows:

- Model is pseudo two dimensional and single phase.
- Model is developed for both steady-state and dynamic operating conditions.
- Model is developed for PEMFC in normal-mode (Section 4.1.2) and the starved-mode (Section 4.1.3).
- PEMFC voltage is assumed to be constant everywhere.
- The hydrogen concentration gradient along the Y direction is assumed to be negligible.
- Owing to the low velocity and low Reynolds number, the flow is assumed laminar.
- The catalyst layer is considered as an ultra-thin layer which only acts as a source/sink term in electrochemical reactions
- CGDL is considered as isotropic media
- Modal analysis is used to estimate the effective oxygen concentration at the CCL.
- The cell is divided into  $N_{ele}$  elements along the X-axis (along the CCH) while variations along the Z direction (cell depth) are neglected

The first step in the model is to calculate the effective reactant concentrations. This step would help us to understand whether the cell is producing or consuming power. Section 4.1.1 introduces a novel method of calculating the effective reactant concentrations at ACL

and CCL. Section 4.1.1 discusses the modal analysis and explains how effective species concentrations across CGDL are calculated. Section 4.1.2 provides the governing equation for normal operating mode (driving mode), while Section 4.1.3 discusses the governing equations for the starved mode (driven mode). Section 4.1 ends with Section 4.1.4, where species concentrations along the CCH are calculated. Hydrogen pumping is also calculated in the same section.

### 4.1.1. Effective Reactant Concentration at CCL and ACL

#### 4.1.1.1. Prior model [15]:

Due to the fast diffusion of hydrogen in anode comparing to oxygen diffusion rate in the cathode, hydrogen concentration gradient across AGDL is neglected [15]:

$$\phi_{H_2,ACL} = \phi_{H_2,ACH} \quad (4-1)$$

The modal analysis is used to determine the effective oxygen concentration along the Y-axis. To calculate the effective oxygen concentration at CCL, first and second Fick's laws are used as follows [15]:

$$\Gamma = -D \frac{d\phi_{O_2}}{dy} \quad (4-2)$$

$$\frac{\partial \phi_{O_2}}{\partial t} = D \frac{\partial^2 \phi_{O_2}}{\partial y^2} \quad (4-3)$$

$\Gamma$  is oxygen flux,  $D$  is the oxygen diffusion coefficient, and  $\phi_{O_2}$  is oxygen concentration. Modal analysis is used to convert this equation to a differential equation in time. Differentiating Equation (4-3) with regard to  $y$  and defining  $\phi'_{O_2} = \frac{\partial \phi_{O_2}}{\partial y}$ , the following equation is derived [15]:

$$\frac{\partial \phi'_{O_2}}{\partial t} = D \frac{\partial^2 \phi'_{O_2}}{\partial y^2} \quad (4-4)$$

The consumption rate of oxygen across the electrode is estimated based on Faraday's Equation (4-5):

$$\Gamma_{(y=l)} = \frac{J}{nF} \quad (4-5)$$

Replacing oxygen flux from Equation (4-5) into Equation (4-3), the following equation is obtained.

$$\phi'_{O_2 (y=l)} = -\frac{J}{nFD} \quad (4-6)$$

Equation (4-6) is one of the boundary conditions for Equation (4-4). Homogenization of Equation (4-4) at  $y=l$  would result in an easier procedure for the solution. Therefore, a new variable is introduced as follows:

$$\bar{b} = \phi'_{O_2} + \phi'_{O_2 (y=l)} \quad (4-7)$$

Calculating  $\phi'_{O_2}$  from Equation (4-7) and replacing it in Equation (4-6), Equation (4-8) is obtained as follows:

$$\frac{\partial \bar{b}}{\partial t} = D \frac{\partial^2 \bar{b}}{\partial y^2} \quad (4-8)$$

In the next step, the method of separation of variables is used to solve Equation (4.8) where  $Y$  is a function of  $y$  and  $T$  is a function of  $t$ :

$$\bar{b}(y, t) = Y(y) \cdot T(t) \quad (4-9)$$

Substituting Equation (4-9) into Equation (4-8) and dividing both sides to  $Y(y) \cdot T(t)$ , the following equation is derived [15]:

$$\frac{dT/dt}{T} = D \frac{d^2Y/dy^2}{Y^2} = \xi \quad (4-10)$$

where  $\xi$  is a constant number.  $\xi$  should be a negative number so that the time function becomes a finite function. Therefore ( $\xi = -\lambda^2$ ) and  $Y$  is calculated as follows:

$$Y = A' \sin[\lambda(L - y)] + B' \cos [\lambda(L - y)] \quad (4-11)$$

$A'$  and  $B'$  are calculated based on the boundary conditions and since ( $\bar{b}_{(y=l)} = 0$ ), Then  $B' = 0$  and  $Y$  can be written as:



$$Y = A' \sin[\lambda(L - y)] \quad (4-12)$$

As a result,  $\bar{b}$  and  $\phi'$  are written as:

$$\bar{b} = A' \sin(\lambda(l - y))T(t) \quad (4-13)$$

$$\phi'_{O_2} = \bar{b} - \phi'_{O_2(y=l)} = A' \sin(\lambda(l - y))T(t) - \phi'_{O_2(y=l)} \quad (4-14)$$

The oxygen concentration in CCH/CGDL interfaced is assumed as the oxygen concentration in the CCH ( $\phi_{O_2(y=0)} = \phi_{O_2,CCH}$ ). Thus, the oxygen concentration is calculated as follows:

$$\phi_{O_2} = \phi_{O_2,CCH} - \phi'_{O_2(y=l)} y + \sum \frac{A'_m}{\lambda_m} \cos(\lambda_m(l - y))T_m(t) \quad (4-15)$$

and  $\lambda_m$  could be obtained as follows:

$$\lambda_m = \frac{(2m + 1)\pi}{2l}, m = 0, 1, 2, 3, \dots \quad (4-16)$$

In order to calculate  $A'_m$ , Equation (4-15) is substituted into Equation (4-3) and multiply both sides by  $\cos(\lambda_n(l - y))$  and integrate across CGDL width results in the following equation:

$$\frac{A'_n L}{2\lambda_n} \left( \dot{T}_n + \frac{1}{\tau_n} T_n \right) = \frac{(-1)^{n+1} \phi_{O_2,CCH}}{\lambda_n} + \frac{\phi'_{O_2(y=l)}}{\lambda_n^2} \quad (4-17)$$

where

$$\tau_n = \frac{1}{D\lambda_n^2} \quad (4-18)$$

$$\lambda_n = \lambda_0(2n + 1) \quad (4-19)$$

$$\tau_n = \frac{\tau_0}{D(2n + 1)^2} \quad (4-20)$$

By considering the first mode ( $n=0$ ) and taking Laplace from both sides of Equation (4-17), the following equation is derived [15]:

$$\tau_n \times \frac{A'_0}{\lambda_0} = \frac{\tau_n S}{\tau_n + 1} \left( (-1)^{n+1} \frac{4\phi_{O_2,CCH}}{\pi(2n+1)} - \frac{8l\phi'_{O_2(y=l)}}{\pi^2(2n+1)^2} \right) \quad (4-21)$$

Substituting  $\phi'_{O_2(y=l)}$  from Equation (4-6) into Equation (4-21), the following equation is derived.

$$\tau_n \times \frac{A'_0}{\lambda_0} = \frac{\tau_n S}{\tau_n + 1} \left( (-1)^{n+1} \frac{4\phi_{O_2,CCH}}{\pi(2n+1)} - \frac{-8l \frac{J}{nFD}}{\pi^2(2n+1)^2} \right) \quad (4-22)$$

D is estimated from limiting current density as follows:

$$D = \frac{J_{lim} l}{nF\phi_{O_2,normal}} \quad (4-23)$$

Replacing D from Equation (4-23) and  $\tau_n$  from Equation (4-22) into Equation (4-15), the following equation is derived.

$$\phi_{O_2,CCL} = \phi_{O_2,CCH} - \frac{Jl}{nFD} - \sum \frac{\tau_n S}{\tau_n + 1} \left( (-1)^n \frac{4\phi_{O_2,CCH}}{\pi(2n+1)} - \frac{8 \frac{J}{nFD}}{\pi^2(2n+1)^2} \right) \quad (4-24)$$

Vijayaraghavan et al. [15] simplified Equation (4-24) further and derived Equation (4-25) as follows:

$$\begin{aligned} \frac{\phi_{O_2,CCL}}{\phi_{O_2,normal}} &= \frac{\phi_{O_2,CCH}}{\phi_{O_2,normal}} - \frac{J}{J_{lim}} - \frac{\frac{4\tau_0 S}{\tau_0 S + 1} \times \phi_{O_2,CCH}}{\pi C_{O_2,normal}} \\ &\quad + \frac{\frac{4\tau_0/9 S}{\tau_0/9 S + 1} \times \phi_{O_2,CCH}}{3\pi C_{O_2,normal}} + \frac{\frac{8\tau_0 S}{\tau_0 S + 1} \times J}{\pi^2 J_{lim}} \end{aligned} \quad (4-25)$$

Equation (4-25) could be simplified as follows:

$$\frac{\phi_{O_2,CCL}}{\phi_{O_2,normal}} = \frac{\phi_{O_2,CCH}}{\phi_{O_2,normal}} - \frac{J}{J_{lim}} - \frac{4}{\pi} \frac{hp_{\phi_{O_2,CCH}-0}}{\phi_{O_2,normal}} + \frac{4}{3\pi} \frac{hp_{\phi_{O_2,CCH}-1}}{\phi_{O_2,normal}} + \frac{8}{\pi^2} \frac{hp_J}{J_{lim}} \quad (4-26)$$

where

$$hp_{\phi_{O_2,CCH}-0} = \frac{\tau_0 S}{\tau_0 S + 1} \phi_{O_2,CCH} \quad (4-27)$$

$$hp_{\phi_{O_2,CCH}-1} = \frac{\tau_0 / 9 S}{\tau_0 / 9 S + 1} \phi_{O_2,CCH} \quad (4-28)$$

$$hp_J = \frac{\tau_0 S}{\tau_0 S + 1} J \quad (4-29)$$

$$\tau_0 = \frac{4nlF\phi_{O_2,normal}}{\pi^2 J_{lim}} \quad (4-30)$$

#### 4.1.1.2. Model enhancement

It is necessary to mention that oxygen mass transfer limitation due to a thin water formation adjacent to the CCL is neglected in Equation (4-26). Water is generated when hydrogen reacts with oxygen at the Cathode. This water diffuses to the surface of the CGDL. When PEMFCs operate at temperatures below the boiling point of water (i.e., below 100 °C), this water may form at the surface of the CGDL. Such a water film has been empirically observed in fuel cells. While it is possible to include the water transport model to estimate the thickness of the water layer, such detailed modeling of water transport would noticeably increase the computational cost of the model, which is not aligned with the purpose of this model. Since the film is absent at no load and the maximum film thickness would be limited, the thickness of the film will be modeled using a sigmoid function with a half-value point at a current density  $J_{min}$ . Therefore, following empirical equation is used to model the reduction in oxygen mass transfer limitation due to water formation:

$$\phi_{O_2,film} = \phi_{O_2,CCH} - R_{A-film} \times \frac{1}{1 + e^{-R_{B-film}(J-J_{min})}} \quad (4-31)$$

where  $R_{A-film}$  represents the magnitude of the concentration drop.  $R_{B-film}$  represents the current scaling factor in the sigmoid function. It must be noted  $R_{A-film}$  and  $R_{B-film}$  must only be estimated one for a given kind of a PEMFC. To account for this concentration drop,  $\phi_{O_2,CCH}$  is replaced with  $\phi_{O_2,film}$  in Equation (4-26)-Equation (4-29) and the following equations are derived:

$$\frac{\phi_{O_2,CCL}}{\phi_{O_2,normal}} = \frac{\phi_{O_2,film}}{\phi_{O_2,normal}} - \frac{J}{J_{lim}} - \frac{4}{\pi} \frac{hp_{\phi_{O_2,film}-0}}{\phi_{O_2,normal}} + \frac{4}{3\pi} \frac{hp_{\phi_{O_2,film}-1}}{\phi_{O_2,normal}} + \frac{8}{\pi^2} \frac{hp_J}{J_{lim}} \quad (4-32)$$

where

$$hp_{\phi_{O_2,film}-0} = \frac{\tau_0 s}{\tau_0 s + 1} \phi_{O_2,film} \quad (4-33)$$

$$hp_{\phi_{O_2,film}-1} = \frac{\tau_0/9 s}{\tau_0/9 s + 1} \phi_{O_2,film} \quad (4-34)$$

$$hp_J = \frac{\tau_0 s}{\tau_0 s + 1} J \quad (4-35)$$

#### 4.1.2. Governing Equations for PEMFC in Driving Mode [15]

Driving mode is a mode that PEMFC produces power rather than consuming it. In this mode, the cell voltage is calculated as follows:

$$V = V_{oc} - \eta_{ohm} - \eta_{act} \quad (4-36)$$

$V_{oc}$  is open-circuit voltage and is obtained from the following equation

$$V_{oc} = V_0 + B_{conc} \ln \left[ (\phi_{O_2,CCL})^{0.5} \cdot (\phi_{H_2,ACL}) \right] \quad (4-37)$$

where  $B_{conc}$  is an effective coefficient to account for kinetics and is in the range of 0.02 to 0.06 [5].  $\phi_{H_2,ACL}$  and  $\phi_{O_2,CCL}$  are calculated based on Equation (4-1) and Equation (4-32) respectively. The ohmic loss ( $\eta_{ohm}$ ) is a nonlinear function [80] and can be written as [68,80]:

$$R_{ohm} = \rho_0 + \rho_J J + \rho_T (T - 298) \quad (4-38)$$

$$\eta_{ohm} = IR_{ohm} \quad (4-39)$$

The activation loss ( $\eta_{act}$ ) can be obtained from the Tafel equation, which can be written in the following form [68,80]

$$\eta_{act,DL} = w_1 + w_2(T - 298) + w_3 T \ln(J_{Ract}) \quad (4-40)$$

The double-layer effect is accounted for in Equations (4-40). The layer of charges at the electrode/electrolyte interface results in the storage of both charge and energy, and it acts as a capacitor.  $J_{Ract}$  indicates the part of the current that goes through the double-layer resistance and is calculated through the following equations.

$$\eta_{act,DL} = \eta_{act} = \frac{1}{C_{DL}} \int (J - J_{Ract}) dt \quad (4-41)$$

$$\frac{d}{dt} J_{Ract} = \frac{J_{Ract} A}{w_3 T C_{DL}} (J - J_{Ract}) \quad (4-42)$$

The next section discusses the governing equation for the driven mode.

#### 4.1.3. Governing Equations for PEMFC in the Driven Mode [15]

As oxygen concentration at CCL drops, open-circuit voltage approaches zero. In this case, oxygen concentration drops to the equilibrium concentration, and as a result, open-circuit cell voltage becomes zero ( $V_{oc} = 0$ ). When the cell becomes fully starved, the ORR does not occur anymore, and the activation loss comes from the hydrogen decomposition reaction at the anode side. Anode activation loss is calculated through the Butler-Volmer formula as follows:

$$J = J_A^{ref} \left[ \exp\left(\frac{\alpha \eta_{act}}{\eta_{act,0}}\right) - \exp\left(\frac{-(1-\alpha) \eta_{act}}{\eta_{act,0}}\right) \right] \quad (4-43)$$

where

$$\eta_{act,0} = \frac{RT}{nF} \quad (4-44)$$

$J_A^{ref}$  is the exchange current density, and  $\alpha$  is the transfer coefficient and is assumed to be equal to 0.5. Thus  $\eta_{act}$  is calculated based on the following simplifications:

$$J = J_A^{ref} \cdot \left[ \exp\left(\frac{0.5\eta_{act}}{\eta_{act,0}}\right) - \exp\left(\frac{-0.5\eta_{act}}{\eta_{act,0}}\right) \right] \quad (4-45)$$

$$\frac{J}{J_A^{ref}} = 2 \sinh\left(\frac{0.5\eta_{act}}{\eta_{act,0}}\right) \quad (4-46)$$

$$\eta_{act} = 2\eta_{act,0} \text{Arcsinh}\left(\frac{J}{2J_A^{ref}}\right) \quad (4-47)$$

Taking  $w_4 = 2\eta_{act,0}$ , activation losses can be found from Equation (4-48).

$$\eta_{act} = w_4 \text{Arcsinh}\left(\frac{J}{2J_A^{ref}}\right) \quad (4-48)$$

Considering the double layer effect, Equation (4-47) is modified to:

$$\eta_{act,DL} = w_4 \text{Arcsinh}\left(\frac{J_{Ract}}{2J_A^{ref}}\right) \quad (4-49)$$

$$\frac{d}{dt}J_{Ract} = \frac{\sqrt{(2J_A^{ref})^2 + (J_{Ract})^2}A}{w_4 C_{DL}} (J - J_{Ract}) \quad (4-50)$$

Ohmic loss is calculated by Equation (4-38) and Equation (4-39), and cell voltage is calculated as follows:

$$V = -\eta_{ohm} - \eta_{act} \quad (4-51)$$

So far, the governing equations across CGDL are obtained while the species concentrations gradient along the CCH is not discussed. Section 4.1.4 develops equations to calculate the species concentration along the CCH. The hydrogen pumping phenomenon is discussed in the same section, and a formula for the hydrogen pumped into the cathode side is developed.

#### 4.1.4. Species Concentration Along the CCH

##### 4.1.4.1. Prior model [15]:

Let's assume there is a mixture of two species (A and B) in a flow, with respective mole fractions  $\chi_A$  and  $\chi_B$ . Let's assume that the total molar flow of the mixture is  $\dot{N}$ . Therefore, the molar fractions of A and B could be calculated as follows:

$$\dot{N}_A = \chi_A \dot{N} \quad (4-52)$$

$$\dot{N}_B = \chi_B \dot{N} = (1 - \chi_A) \dot{N} \quad (4-53)$$

Therefore, the ratio of molar fluxes could be obtained as follows:

$$\frac{\dot{N}_A}{\dot{N}_B} = \frac{\chi_A}{1 - \chi_A} \quad (4-54)$$

Let's assume that the mole fraction of species A changes from  $\chi_A$  to  $\chi'_A$  due to consumption or removal from the mixture. The next mole fraction ( $\chi'_A$ ) as follows:

$$\frac{\chi'_A}{1 - \chi'_A} = \frac{\dot{N}_A - \Delta \dot{N}_A}{\dot{N}_B} = \frac{\chi_A}{1 - \chi_A} - \frac{\Delta \dot{N}_A}{\dot{N}_B} \quad (4-55)$$

$$\chi'_A = 1 - \frac{1 - \chi_A}{1 - \frac{\Delta \dot{N}_A}{\dot{N}_B} (1 - \chi_A)} \quad (4-56)$$

Over a (small) area  $A_{ele}$ ,

$$I_{ele} = JA_{ele} \quad (4-57)$$

Hydrogen is consumed at  $\Delta\dot{N}_{H_2} = \frac{I_{ele}}{2F}$  at the anode in either mode. Hence the hydrogen mole fraction at the next anode element is calculated as follows:

$$\chi_{H_2,A}(out) = 1 - \frac{1 - \chi_{H_2,A}(in)}{1 - \frac{I_{ele}}{2F\dot{N}_{B,A}}(1 - \chi_{H_2,A}(in))} \quad (4-58)$$

At the cathode,  $\Delta\dot{N}_{O_2} = \frac{I_{ele}}{4F}$  and therefore, the oxygen mole fraction at the next cathode element is calculated as follows:

$$\chi_{O_2,C}(out) = 1 - \frac{1 - \chi_{O_2,C}(in)}{1 - \frac{I_{ele}}{4F\dot{N}_{B,C}}(1 - \chi_{O_2,C}(in))} \quad (4-59)$$

As long as there is sufficient oxygen,  $\chi_{O_2,C}(out)$  can be calculated using Equation (4-59). When the fuel cell is oxygen-starved, all of the oxygen would be consumed and  $\chi_{O_2,C}(out)$  will become negative. Physically, the mole fraction of oxygen  $\chi_{O_2,C}(out)$  cannot be negative and this situation corresponds to the oxygen concentration reaching zero and the inception of hydrogen generation. Using this fact and by writing the equations in the concentration form,  $\phi_{H_2,A}(out)$  and  $\phi_{O_2,C}(out)$  will be obtained by Equation (4-60) and Equation (4-61), respectively.

$$\phi_{H_2,A}(out) = \frac{P_A}{RT} \left( 1 - \frac{\frac{P_A}{RT} - \phi_{H_2,A}(in)}{\frac{P_A}{RT} - \frac{I_{ele}}{2F\dot{N}_{B,A}} \left( \frac{P_A}{RT} - \phi_{H_2,A}(in) \right)} \right) \quad (4-60)$$

$$\phi_{O_2,C}(out) = \max \left[ \frac{P_C}{RT} \left( 1 - \frac{\frac{P_C}{RT} - \phi_{O_2,C}(in)}{\frac{P_C}{RT} - \frac{I_{ele}}{4F\dot{N}_{B,C}} \left( \frac{P_C}{RT} - \phi_{O_2,C}(in) \right)} \right), 0 \right] \quad (4-61)$$



#### 4.1.4.2. Model enhancement through the effect of hydrogen pumping

We will now model the hydrogen pumping that was neglected in the previous model. From Faraday's law, the total number of moles of hydrogen transported is given by

$$\dot{N}_{H_2}(gen) = \frac{I_{ele}}{2F} \quad (4-62)$$

Each mole of oxygen entering the element will consume two moles of hydrogen. Hence

$$\dot{N}_{H_2}(out) = \frac{I_{ele}}{2F} - \frac{2\chi_{O_2,C}(in) \cdot \dot{N}_{B,C}}{1 - \chi_{O_2,C}(in)} \quad (4-63)$$

The hydrogen concentration at the end of the element on the cathode side in the starvation mode can be obtained by Equation (4-64), Equation (4-65), and Equation (4-66).

$$\chi_{H_2,C}(out) = 1 - \frac{1 - \chi_{H_2,C}(in)}{1 + \frac{\frac{I}{2F} - \frac{2\chi_{O_2,C}(in) \cdot \dot{N}_{B,C}}{1 - \chi_{O_2,C}(in)}}{\dot{N}_{B,C}}} (1 - \chi_{H_2,C}(in)) \quad (4-64)$$

$$\chi_{H_2,C}(out) = \max[\chi_{H_2,C}(out), 0] \quad (4-65)$$

$$\phi_{H_2,C}(out) = \frac{P_C}{RT} \chi_{H_2,C}(out) \quad (4-66)$$

So far, the species concentration gradients along the CCH and across the CGDL were discussed for both driven and driving modes in Section 4.1. Section 4.2 discusses the numerical algorithm and provides validation versus experimental data.

## 4.2. Numerical Algorithm

In this section, the numerical algorithm used to solve the governing equations is explained. As mentioned earlier, the entire cell is divided into  $N_{ele}$  elements along the X-axis (along the CCH) where  $i^{th}$  element connects nodes  $i$  and  $(i + 1)$ . Figure 4-2 shows the type of mesh used for the numerical algorithm. (It may be noted that the size of the mesh has

been exaggerated in this figure). Each element is a rectangle that includes both CCH and CGDL for anode and cathode sides.

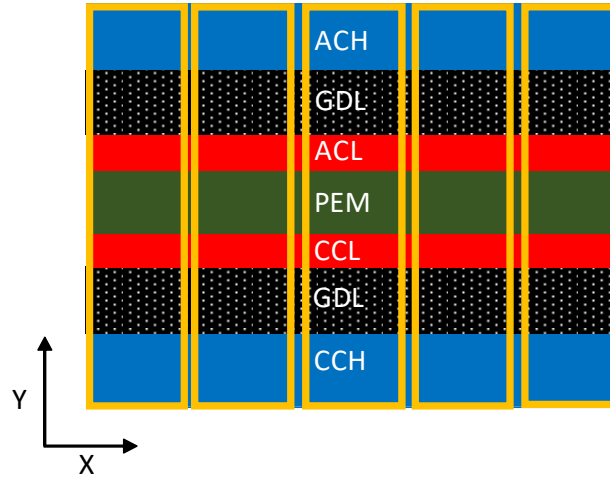


Figure 4-2. Mesh type used the pseudo, two-dimensional model developed for diagnosis purposes

Important model inputs are listed as follows:

- Required current ( $I_{req}$ )
- Inlet species concentrations ( $\phi_{H_2,A}(in), \phi_{O_2,C}(in)$ )
- Inlet species flow rates ( $\dot{N}_{H_2}(in), \dot{N}_{air}(in)$ )
- Anode and cathode pressures ( $P_A, P_C$ )
- Number of mesh elements ( $N_{ele} = 50$ )
- Convergence criterion ( $eps = 0.001$ )

A triple nested algorithm is used to obtain the polarization curves. In this algorithm, the current is model input, and an initial voltage is guessed as cell voltage. Cell voltage is assumed to be constant for all the elements. At the first step, oxygen and hydrogen concentrations are set as inlet concentrations. Then, the current density is iterated to find the cell voltage equal to the assumed cell voltage. Reactant concentrations are calculated based on whether the segment operates in normal or starved mode, and the values are updated for the next cell. By integrating the current densities produced in all segments, the total current density can be calculated and compared with the model input. If the difference between the calculated current and the input current is noticeable, a new cell voltage will be guessed, and the whole algorithm repeated until the calculated current become equal to the model input. The complete algorithm is provided in Figure 4-3.

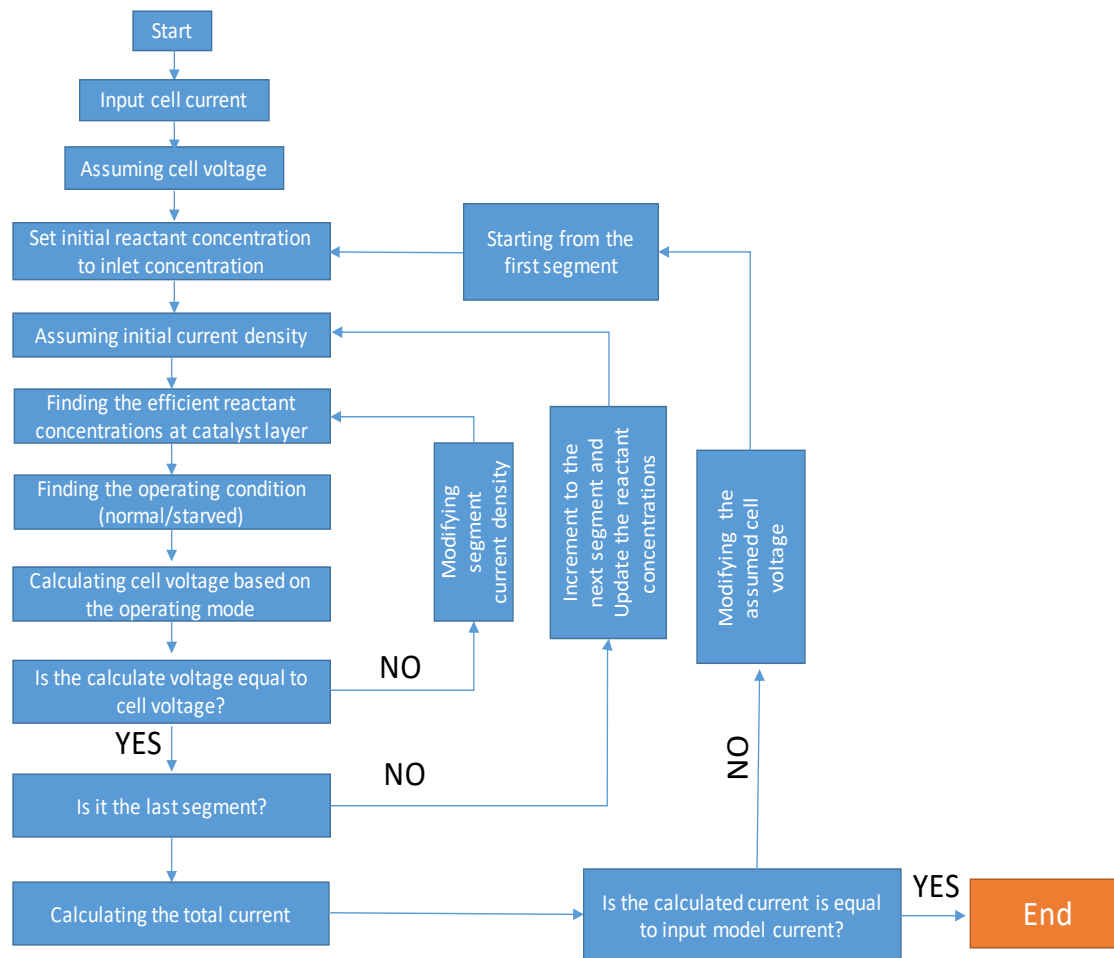


Figure 4-3. Numerical algorithm of the pseudo, two-dimensional model developed for diagnosis purposes

### 4.3. Model Validation

The experimental work by Wang et al. [68] is used for validating the fuel cell. The cell parameters are as follows:

Table 4-1. Model parameters [68]

Parameter	Value
$B_{\text{conc}}$	0.05
$C_{\text{DL}}$	0.1 F
$F$	$96485 \frac{\text{C}}{\text{mol}}$
$J_A^{\text{ref}}$	$100 \frac{\text{A}}{\text{m}^2}$
$J_{\text{lim}}$	$79.88 \frac{\text{A}}{\text{m}^2}$
$N_{\text{ele}}$	100
$R$	$8.314 \frac{\text{J}}{\text{K} \cdot \text{mol}}$
$R_{\text{ohm}}$	0.0347 Ohm
$T_{\text{room}}$	298 K
$\rho_J$	0.0058
$\rho_0$	$3.9 \times 10^{-5}$
$\rho_T$	$4.94 \times 10^{-5}$
$w_1$	0.4170
$w_2$	$-2.9090 \times 10^{-3}$
$w_3$	$1.0417 \times 10^{-4}$
$w_4$	$1.723 \times 10^{-4}$
$P_A$	1.5 atm
$P_C$	1 atm

Figure 4-4 compares the polarization curve obtained from the numerical data with the experimental results derived by Wang et al. [68]. Figure 4-5 compares the dynamic voltage

response to the step current change from 5 A to 10 A. The maximum error in both Figures is less than 0.2 percent.

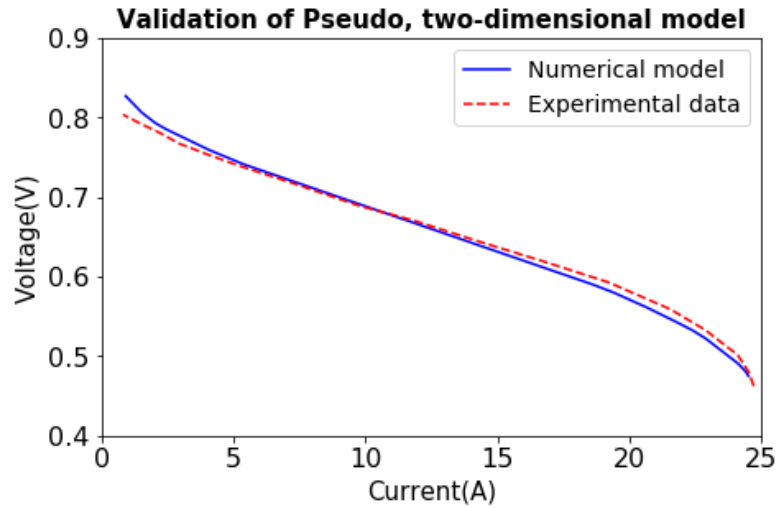


Figure 4-4. Validation of pseudo, two-dimensional model based on the polarization curve

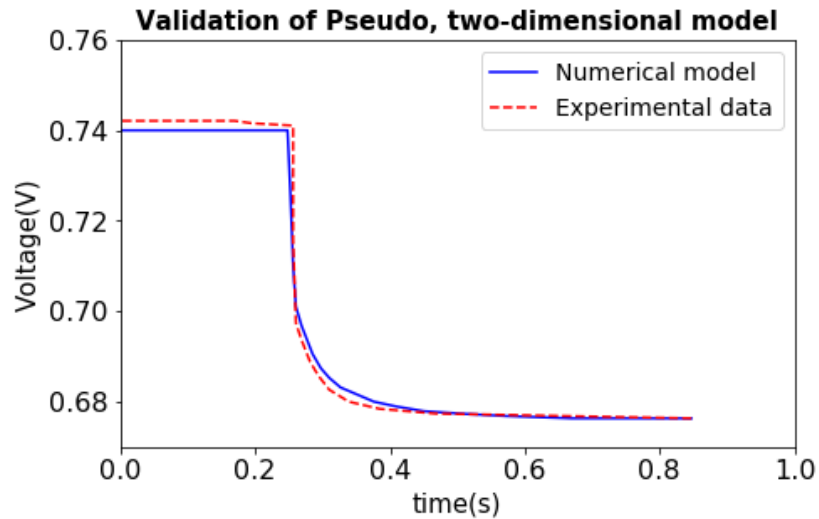


Figure 4-5. Validation of pseudo, two-dimensional models based on the transient response to a step-change in current from 5 A to 10 A

Also, the grid independency test is conducted on grids with 50 and 100 cells, and it has been seen that by changing the mesh size from 50 to 100, the maximum change is less than 1 percent. In the next section, simulation results are discussed and compared versus the data collected at Ballard Power Systems Inc.

## 4.4. Experimental Observations of Oxygen Starvation and Comparisons with Model

Numerical results are compared with the results of five different experimental tests that were conducted in three different cell configurations at Ballard Power Systems' research and testing facility in Burnaby, BC, Canada. Section 4.4.1 and Section 4.4.2 utilizes the experimental data obtained from a 9-cell Mk1100 stack with an estimated limiting current of 1260 A. Section 4.4.3 and Section 4.4.4 report the experimental data obtained from a 10-cell Mk902 stack with an estimated limiting current of 1260.7 A, and eventually Section 4.4.5 compares the numerical results obtained from the model versus the experiment results from a 20-cell Mk903 stack with an estimated limiting current of 780 A.

It is necessary to mention that all gas flows are measured in standard cubic centimeters per minute (sccm), which corresponds to gas flow at the standard pressure and temperature. In addition, standard liter per minute (slm) represents another unit for the gas volumetric flow rate at standard conditions.

Hydrogen leak is simulated by hydrogen injection in the inlet of the cathode flow field of a cell. Also, a hydrogen sensor is used to measure the hydrogen flow rate at the end of the CCH. The model assumes that the oxygen concentration in the cathode entrance is reduced due to the direct combustion of hydrogen and oxygen. The simulations are conducted with the modified oxygen concentration values, which can be calculated from Equation (4-67).

$$\phi_{O_2-CCH}^{eff} = \frac{P_c(\chi_{O_2,amb} - 0.5\chi_{H_2,leak})}{1 - 0.5\chi_{H_2,leak}} \quad (4-67)$$

In this equation,  $\chi_{O_2,amb}$  is the ambient oxygen mole fraction (20.96%) and  $\chi_{H_2,leak}$  is the ratio of the injected hydrogen flow rate to the airflow supplied to the cathode flow field. This parameter could be calculated as follows:

$$\chi_{H_2,leak} = \frac{FR_{injected\_hydrogen}}{FR_{injected\_hydrogen} + FR_{Cathode\_before\_injection}} \quad (4-68)$$

where FR stands for flow rate. Also, it is necessary to mention that Hydrogen Emission is considered as hydrogen molar fraction at the end of the CCH. This concentration is calculated based on the numerical model.

#### 4.4.1. Steady-State Model Validation for a Leak in a Single Cell of the First Commercial Fuel Cell Stack, a 9-Cell Short Stack

Two experiments were conducted at steady-state to validate the model at a current of 10 A and 20 A, respectively. The active area of the fuel cell was provided by Ballard based on a confidentiality agreement between authors and Ballard. The parameters for the tests are provided in Table 4-2, with the exception of the active area. All other parameters for the fuel cell were taken from Wang et al. [68].

Table 4-2. Experimental steady-state tests parameters for hydrogen injection in just one cell

Airflow (liters/min)	Hydrogen flow (liters/min)	Inlet air pressure (psig)	Inlet hydrogen pressure (psig)	PEMFC temperature (°C)	Limiting current (A)	Active area (cm <sup>2</sup> )
1.03	0.66	6.24	8.27	68	1260	confidential

Hydrogen leak is simulated by hydrogen injection in the inlet flow field of a cell, as shown in Figure 4-6. Also, a hydrogen sensor is used to measure the hydrogen rate at the end of the CCH. An RKI Instruments Model FHD-752 (0 – 4%) hydrogen concentration sensor was used to measure the hydrogen emissions. It must be noted that the readings from the hydrogen sensor were scaled appropriately by Vijayaraghavan et al. [15] to account for downstream dilution of the stack cathode outlet flow with dry air. Figure 4-6 shows the schematic of the setup.

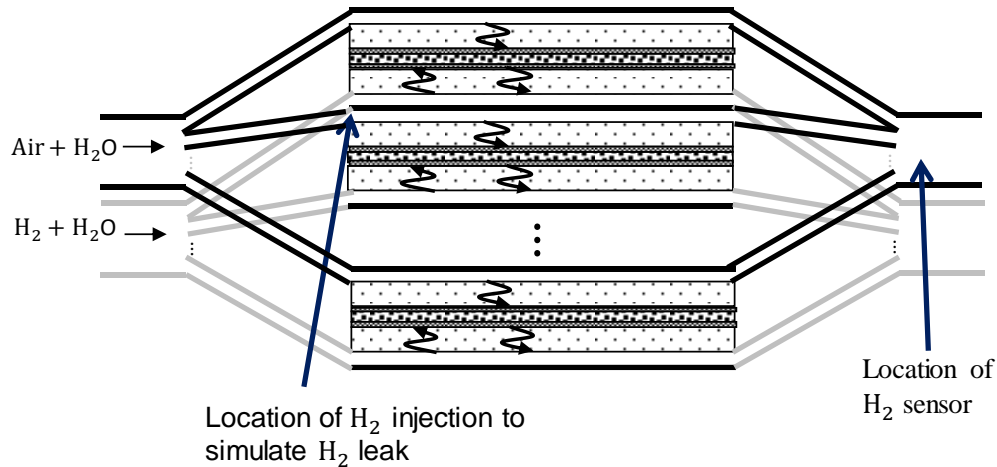


Figure 4-6. Schematic of the setup used for testing first commercial fuel cell stack, a 9-cell short stack

As shown in Figure 4-7 and Figure 4-8, by increasing the hydrogen leak rate (hydrogen flow rate injected at the CCH entrance), at some point, the hydrogen sensor can detect hydrogen at the end of the cathode flow field, and that is where full starvation happens. The model is able to predict this transition point as well as hydrogen emission (hydrogen mole fraction) at the end of the cathode flow field. Comparing Figure 4-7 and Figure 4-8 illustrates that full starvation occurs at a lower hydrogen leak rate when current increases from 10 A to 20 A. When a higher current is taken from the fuel cell, the higher amount of oxygen participates in the ORR, which means by injecting less hydrogen (~18% at 20A versus 23% molar concentration of hydrogen at 10A), the oxygen concentration becomes zero in some parts of the catalyst layer, and as a result, starvation happens sooner. From Figure 4-9 and Figure 4-10, it is clear that hydrogen pumping has an important effect on the emission, and the current model is better able to predict the emission relative to a model purely based on the hole size. Furthermore, the pumping effect increases significantly at higher load currents.



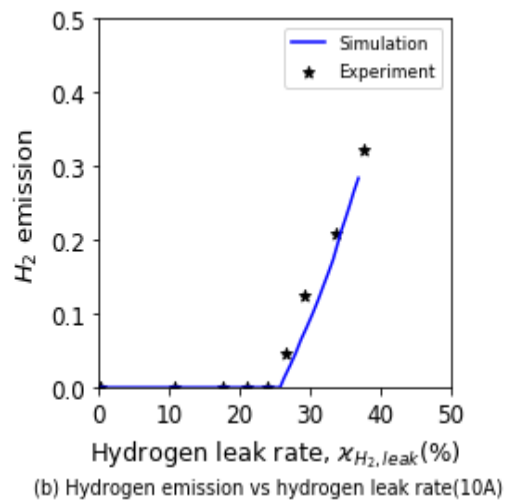
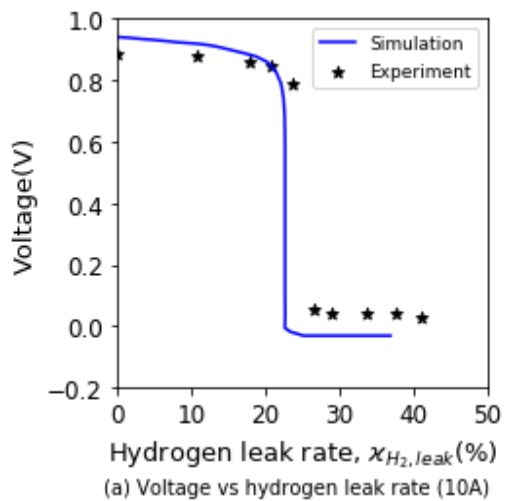


Figure 4-7. Voltage and hydrogen emission versus hydrogen injection at 10 A in a leaky single cell of 9-cell short stack

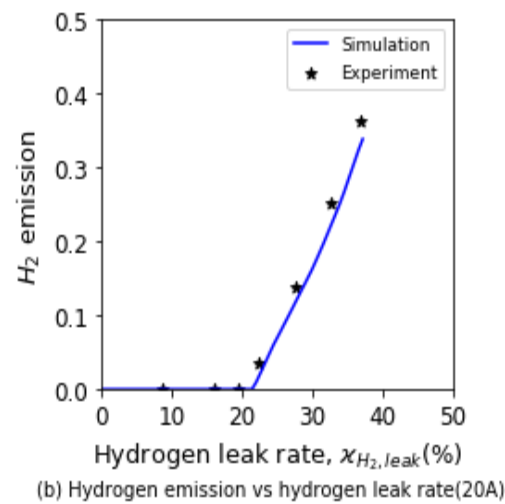
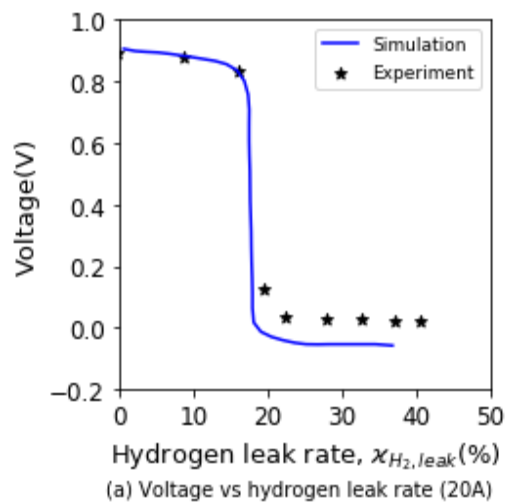


Figure 4-8. Voltage and hydrogen emission versus hydrogen injection at 20 A in a leaky single cell of 9-cell short stack

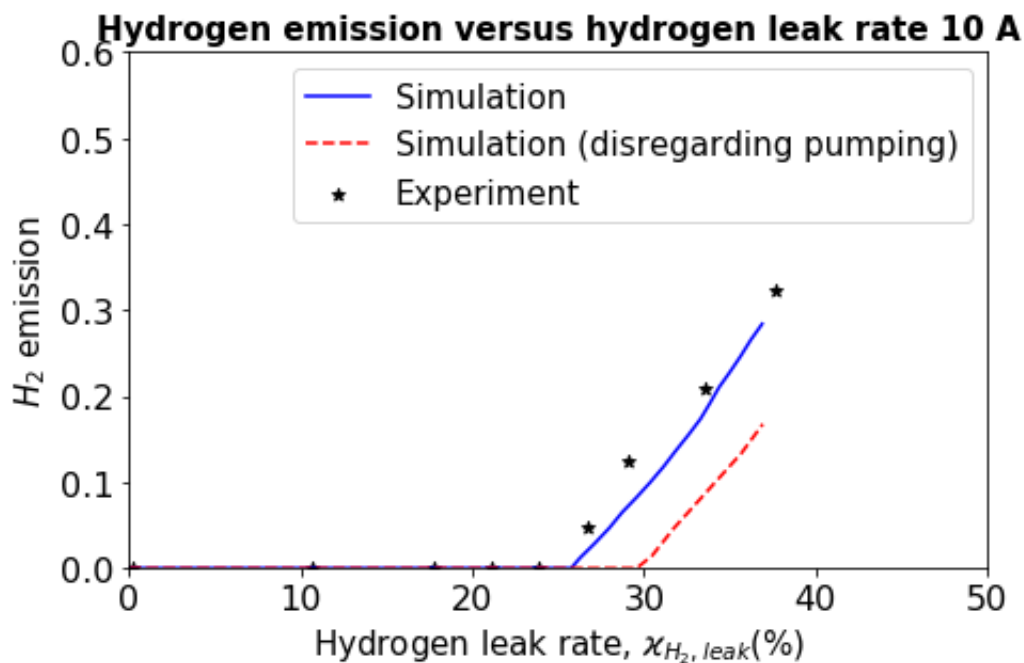


Figure 4-9. Hydrogen emission versus hydrogen leak rate at 10 A

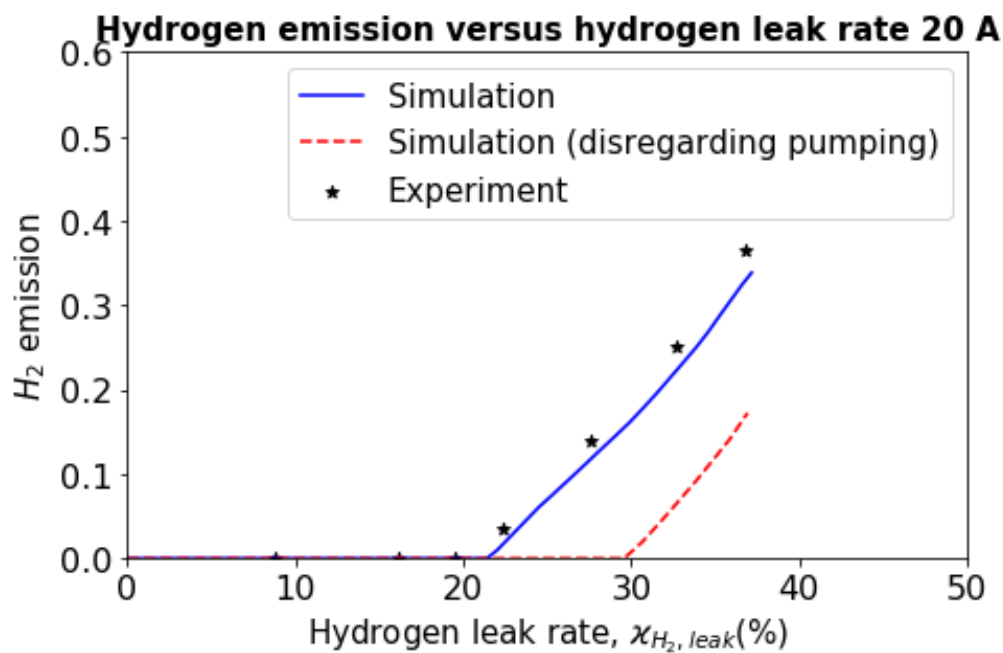


Figure 4-10. Hydrogen emission versus hydrogen leak rate at 20 A

In the next step, the current is incremented from 0A to 50A, and the hydrogen leak rate that triggers hydrogen pumping is calculated in Figure 4-11. Our model illustrates that less hydrogen leak rate is required to fully starve the stack at higher current values.

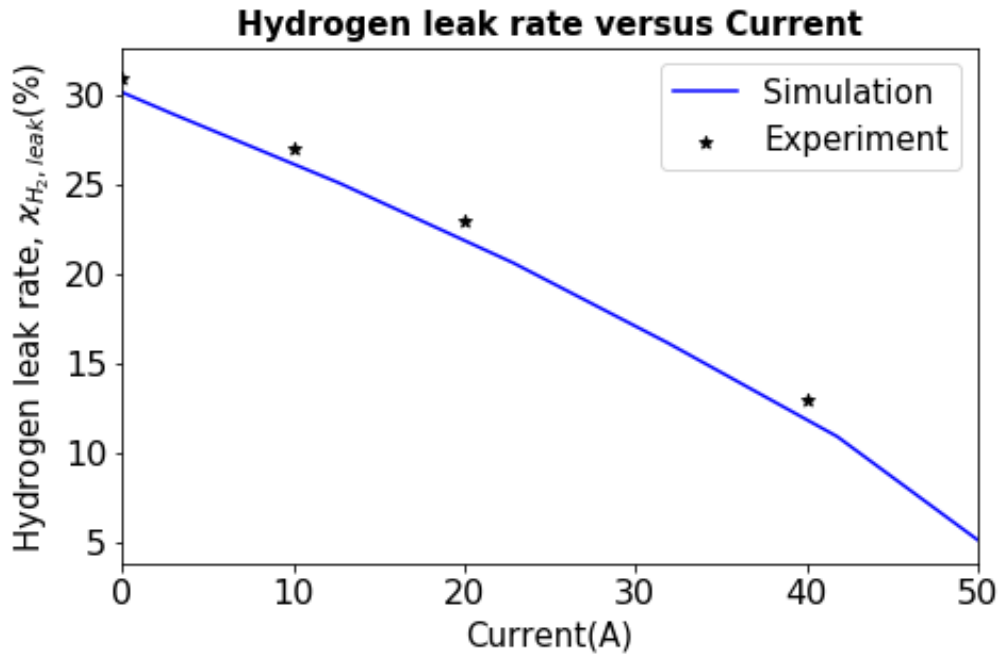


Figure 4-11. Hydrogen pumping triggering leak at different currents in the entire stack of the 10-cell short stack

#### 4.4.2. Transient Model Validation for a Leak in a Single Cell of the First Commercial Fuel Cell Stack, a 9-Cell Short Stack

In this experiment, the hydrogen leak is increased multiple times in steps of 50 sccm. For the transient simulation, a forward Euler solver with a time step of 0.5 s is utilized. Each step increase in hydrogen leak simulates a sudden onset of a leak. While there may not be such a sequential of leaks in a real PEMFC, the experiment illustrates the model's ability to predict a strong transient behavior. Figure 4-12 shows that there is an offset between the transient model response and the experimental data. Similar to steady-state results, voltage and hydrogen emission obtained by our model are higher than experimental data. Despite these differences, the transient responses of the model are in good agreement with the experiment data. The current is 10 A in the simulation and the experiment.

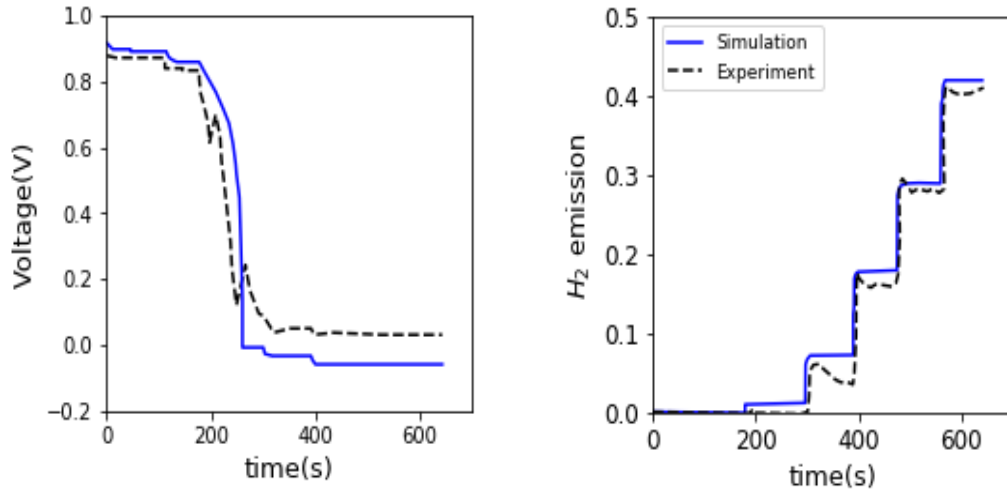


Figure 4-12. Transient model validation for a sudden increase in a leak in a single cell of a 9-cell short stack.

#### 4.4.3. Steady-State Model Validation for a Leak in the Entire Stack of a Second Commercial Fuel Cell Stack, a 10-Cell Short Stack

The steady-state experiments from Section 4.4.1 are repeated for a 10-cell fuel cell stack. In the experiments performed in Section 4.4.1, hydrogen was injected into the inlet of the cathode flow field of only one cell, while here, hydrogen is injected into the cathode inlet of all cells, as illustrated in Figure 4-13. In the former case, the effect of a leak in a single cell was investigated, while in the latter one, the effect of leakage in all cells was simulated. There were three different tests conducted, and the results were provided in Figure 4-14 to Figure 4-16. Test parameters for each experiment are provided in Table 4-3.

Table 4-3. Experimental steady-state tests parameters for hydrogen injection in the whole stack

Test	Airflow (slm)	Current (A)	Limiting current (A)	Other parameters
Case 1	6.73	0	1260	Same as [68]
Case 2	6.73	8	1260	Same as [68]
Case 3	60	0	1260	Same as [68]



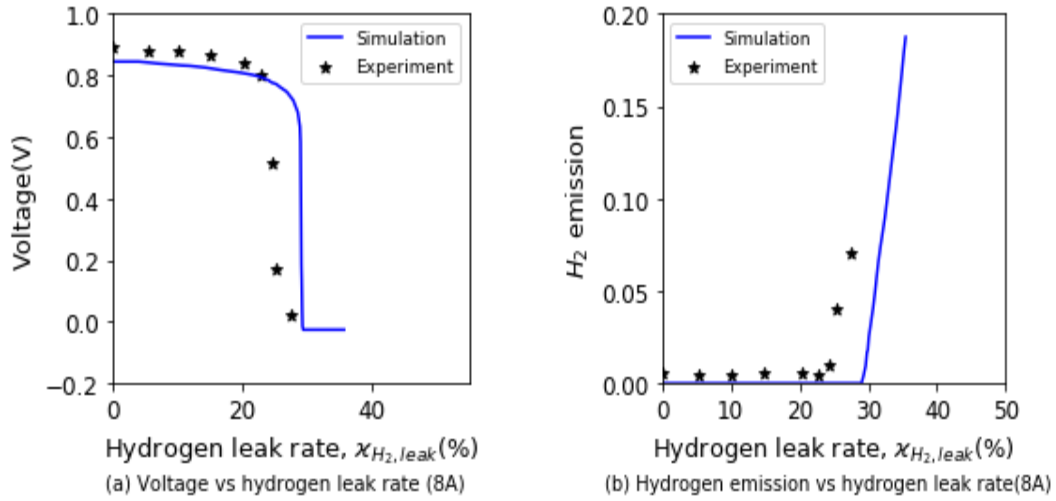


Figure 4-15. Voltage and hydrogen emission response under hydrogen injection at 6.73 slm airflow and 8 A for a leak in the entire stack of the 10-cell short stack

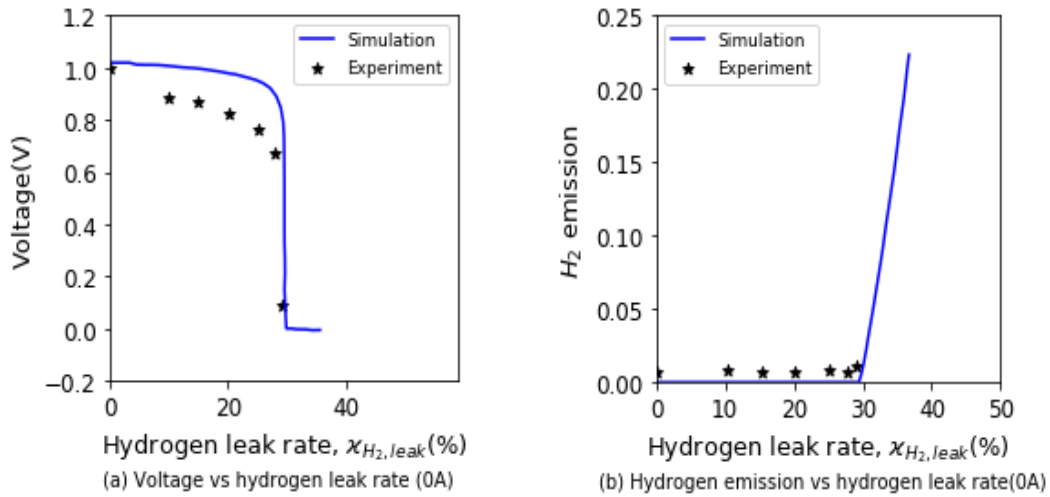


Figure 4-16. Voltage and hydrogen emission response hydrogen injection at 60 slm airflow and 0 A for a leak in the entire stack of the 10-cell short stack

#### 4.4.4. Test on a Real MEA Transfer Leak in the Second Commercial Fuel Cell Stack Model

In this section, a leaky PEMFC is tested at 8 A. Different leak rates for the numerical model are calculated based on the different anode and cathode differential pressures. Since the calculation of the exact hydrogen crossover to the cathode side is difficult, an equivalent

hydrogen leak is calculated proportionally to the differential pressures. This assumption is also confirmed by Mousa et al. [60,61]. Figure 4-17 shows a very good match between simulation and experiments, suggesting that the model, coupled with a simple expression for hydrogen flow versus hole sizes and anode-to-cathode pressure difference, could be used to determine cell voltage response as the hole grows. It should be noted that conducting more experiments and deriving a generic empirical relation between pressure difference and leak size could equip this model to be used as a diagnosis tool to simulate not only the amount of leakage but the growth of the hole.

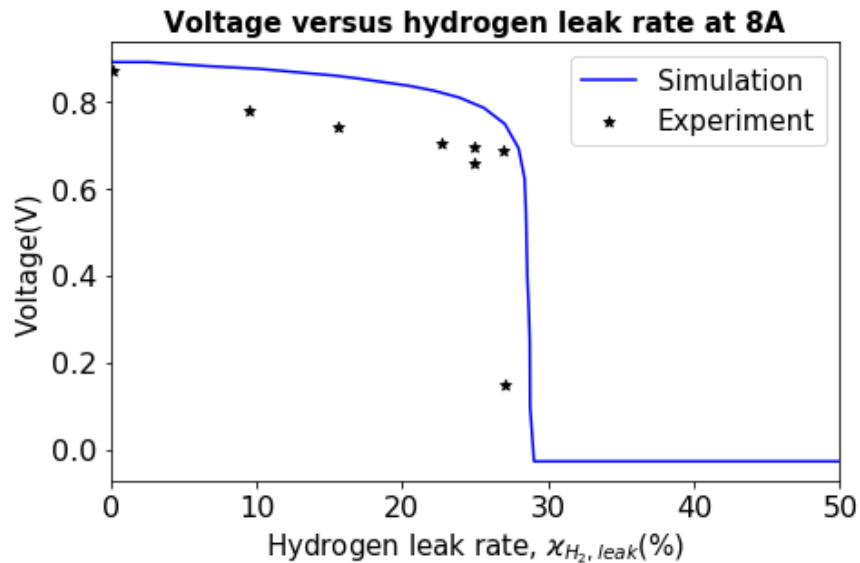


Figure 4-17. Actual hydrogen transfer leak test simulated by different differential pressure

#### 4.4.5. Starvation Point Determination on a Third Commercial Fuel Cell Stack

The purpose of this section is to understand the relation between the current and hydrogen leak rate that results in triggering full starvation and hydrogen pumping. It is clear that at higher currents, a lower hydrogen leakage rate would result in full starvation and, consequently, hydrogen pumping. A commercial fuel cell stack (an Mk903 stack) with vehicle operation airflow rate was used in this experiment. The current was set to zero at first and then was increased through several steps. At each step (each specific current), hydrogen was injected at the inlet of all cathode flow fields. Then hydrogen flow rate was

increased from zero to the point that the hydrogen sensor could detect hydrogen at the outlet of all cathode flow fields. This point is a transition point to the full oxygen starvation mode, and the value recorded for the injected hydrogen flow rate is the hydrogen leak rate for that specific current. Figure 4-18 was obtained by performing this experiment for different current values. In the simulation, another loop is used to gradually increase hydrogen leakage from zero to the point that voltage becomes equal to zero. Other parameters are the same as Wang et al. [68]. Figure 4-18 shows that numerical results underestimate the values for hydrogen leak, and this difference might be due to the fact that there are errors in voltage measurement in the starvation mode. Constant cell voltage is not quite a correct assumption, as mentioned before. Also, there are uncertainties in the actual airflow to individual cells at starvation. Nonetheless, the model shows a good agreement with experimental data.

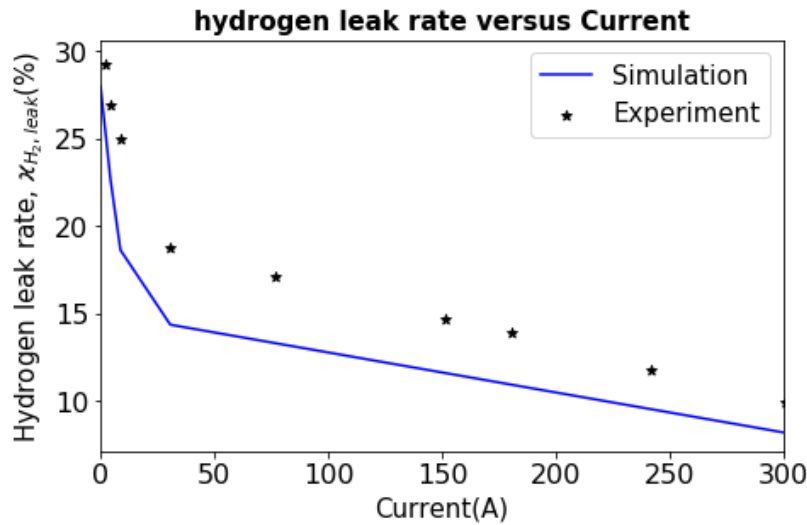


Figure 4-18. Full starvation model results on the third commercial fuel cell stack

## 4.5. Chapter Conclusion

In this chapter, a pseudo two-dimensional, steady-state, and dynamic model is presented to simulate PEMFC performance in case of normal operating conditions and complete starvation. Model's results are compared with experiments, and good agreement between



numerical data and experimental results was observed. The model employs a novel modal analysis to account for the transient response of the fuel cell. The separation of variables and modal analysis illustrates that three high pass filters must be included in the transient part to accurately compute the effective concentration at the CCL. The double-layer effect is also considered in the model, and the oxygen mass transfer losses due to the formation of a thin layer of water are also calculated based on an empirical equation. Hydrogen pumping is added to the model, and the model can accurately predict hydrogen emission at the cathode outlet caused by leakage and hydrogen pumping phenomenon. The model is solved iteratively through a triple-nested loop algorithm. Euler solver with a forward difference scheme is used to model the transient response. Validation of the model is performed versus experimental data obtained by Wang et al. [68] and Ballard corporation's test data. The Ballard experimental data is provided for three commercial PEMFC stacks and one leaky cell. In the first stack, leakage is simulated by first injecting hydrogen flow to once cell, while in the other test, hydrogen is injected in the flow fields of all cells. For both cases, voltage response and hydrogen emission values are compared with the model, and results are in good agreement with the data. However, negative voltages are not observed in the experimental data. This might be due to the experimental error since the author has limited information about how the experiment is conducted. Also, the injection of hydrogen into one flow channel would affect the airflow in the neighbor cells, and the effect is not clear yet, and in-depth experimental studies are required to clear out the problem. In the next step, the model is subjected to step changes in hydrogen injection at the cathode side. Voltage response and emission response is recorded and compared with the experimental data of the first commercial stack. Although this incident does not happen in PEMFC, the numerical results could illustrate its effectiveness as a base model for diagnosis purposes. In addition, model results are compared with the results of a leaky MEA in a second commercial stack. Eventually, the model is executed for different leak rates with a fixed current to calculate the hydrogen leak rate led to the third commercial stack's full starvation. The current is incremented from 0 to 300 A and the fully-starvation led hydrogen leakage is recorded. The difference in data seems to be related to the constant cell voltage assumption in the model and the uncertainties in the experiments. The model underestimates the value of hydrogen leaks in this experiment.

The inclusion of the hydrogen pumping, double-layer effect, and thin-layer water formation in the model and comparing the results with experimental data shows that the pseudo,

two-dimensional model could be used as a base model for diagnosis purposes. The precision and computational effectiveness of the model makes this model a strong candidate to diagnose different faults and eventually used in a controller.

## Chapter 5. Leakage Diagnosis and Quantification

The development of ML algorithms has resulted in the noticeable development of diagnosis methods. These methods are mainly employed as black-box models in model-based diagnosis methods to calculate the residual of the predicted performance versus real performance. More recently, non-model based diagnosis scholarly works have employed ML methods to train the experimental data derived from EIS, CV, and other experimental setups to diagnose different PEMFC faults. In this chapter, a combined model-based and non-model based approach is proposed to detect and quantify leakage in PEMFCs. The combined approach utilizes the model that is developed in Chapter 4 to create a dataset in steady-state mode. In the first step, two different classifiers are developed and used to classify PEMFC into normal and leaky categories. Next, In the case of leaky PEMFCs, two types of regressors are employed to quantify the amount of leakage and to predict the current that results in full starvation and the inception of the hydrogen pumping phenomenon. KNN and ANN estimators are selected and compared for both classification and regression parts. KNN estimator is discussed in Appendix C, and ANN classifier is explained in Appendix D. The performance of classifiers are evaluated based on different metrics such as accuracy, precision, F1-score, and recall, while the performance of regressors are compared based on  $R^2$  score, Mean Squared Error (MSE) and Mean Average Error (MAE). The performance indexes are explained in detail in Appendix E. Employed estimators are tuned mainly based on grid search [81] and cross-validation [81] methods, and best estimator parameters are selected. The purpose of developing the leakage diagnosis tool is to detect and quantify leakage before hydrogen pumping occurs, and voltage drops to negative numbers.

## 5.1. Approach Principle

There are several types of learning, as provided in Figure 5-1. However, in general, the learning process could be categorized into supervised and unsupervised learning.

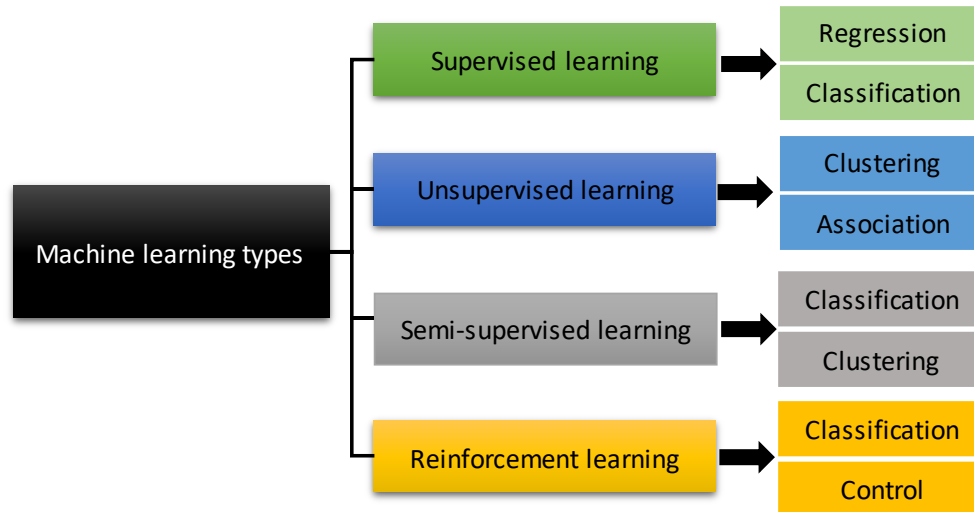


Figure 5-1. ML types [81]

Supervised learning refers to the development of a model that maps input data to output results. In this type of learning, we use both input and output data to train and test the estimator. However, in unsupervised learning, a model is built solely based on the input data without any connection to the target outcomes. Classification and regression algorithms are considered as supervised learning methods. Classification refers to a problem that data are labeled into different categories, whereas a numeric label is predicted in regression. The proposed problem is a supervised learning problem since we can label and categorize data in the dataset into leaky and healthy PEMFCs, and in the case of leaky PEMFCs, the amount of PEMFC leakage can be obtained by using regressors [81]. Leakage diagnosis and quantification methodology are provided in Figure 5-2.

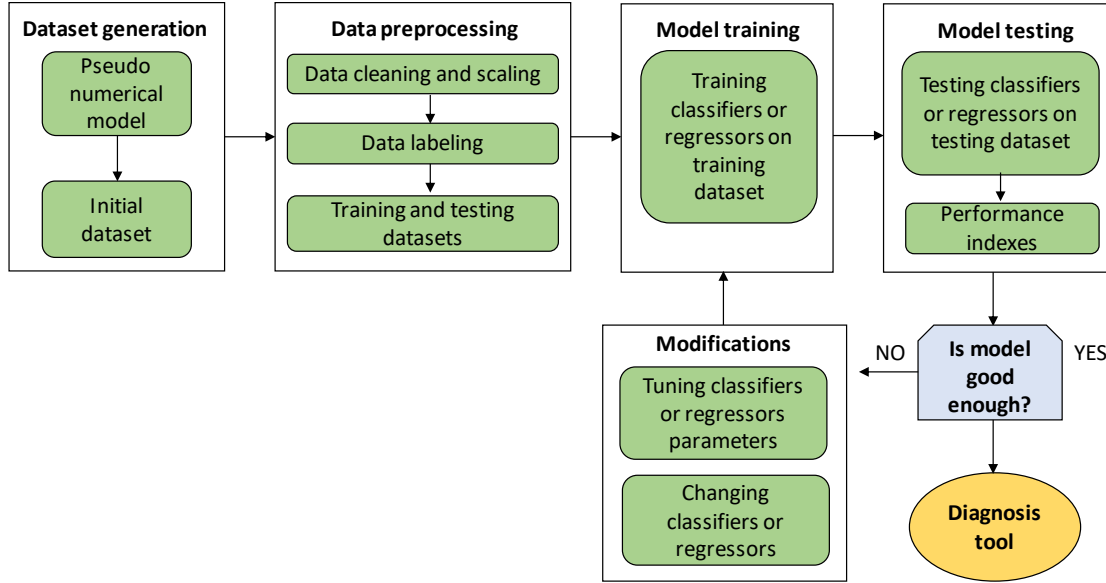


Figure 5-2. Diagnosis methodology [81]

Two classifiers and two regressors are evaluated in this work for developing the diagnosis tools. KNN and ANN are chosen since they are both non-linear estimators and are more appropriate to address the non-linearity in PEMFC data.

## 5.2. Dataset Generation in Steady-State

The pseudo two-dimensional model that is used in Chapter 4 is run based on different parameters to build the base dataset. The cell information is the same as a cell in an MK1100 commercial stack. Eight parameters, including current, hydrogen leakage flow rate, oxidizer type (air or pure oxygen), anode hydrogen mole fraction, cathode inlet flow rate, fuel cell temperature, anode, and cathode pressures are varied based on the values in Table 5-1. The voltage value is recorded for each simulation and the data collection is completed by recording all the voltage values. It is necessary to note that the upper bound value for current (50 A) is chosen in a way that even in the case of zero leakage, PEMFC becomes fully starved at high current values. Therefore, the upper bound is high enough to include the current that led to complete oxygen starvation (or the inception of hydrogen inception) for each leakage value. This is beneficial in the case of hydrogen pumping prediction.

Next, input and output arrays are rearranged to form the required datasets for ML training. Dataset 1 includes all the data, while dataset 2 only includes the rows corresponds to positive leakage values. The process of dataset generation for ML training is shown in Figure 5-3.

Table 5-1. Range of different features used for generating the basic dataset

Parameters	Range of values	Units
Current (I)	[0,50] with 2A increments	A
Cathode flow rate ( $FR_C$ )	[1,1.5] with 0.1 slm increments	slm
Leak flow rate ( $FR_{leak}$ )	[0,400] with 20 sccm increments	sccm
Cathode inlet oxygen mass concentration ( $X_{O_2,in}$ )	0.21 and 1	—
Anode inlet hydrogen concentration ( $X_{H_2,in}$ )	0.9, and 1	—
Fuel cell temperature (T)	58.5 , 68.5, 78.5	°C
Cathode pressure ( $P_C$ )	1,2,3,4	atm
Anode pressure ( $P_A$ )	1,2,3,4	atm

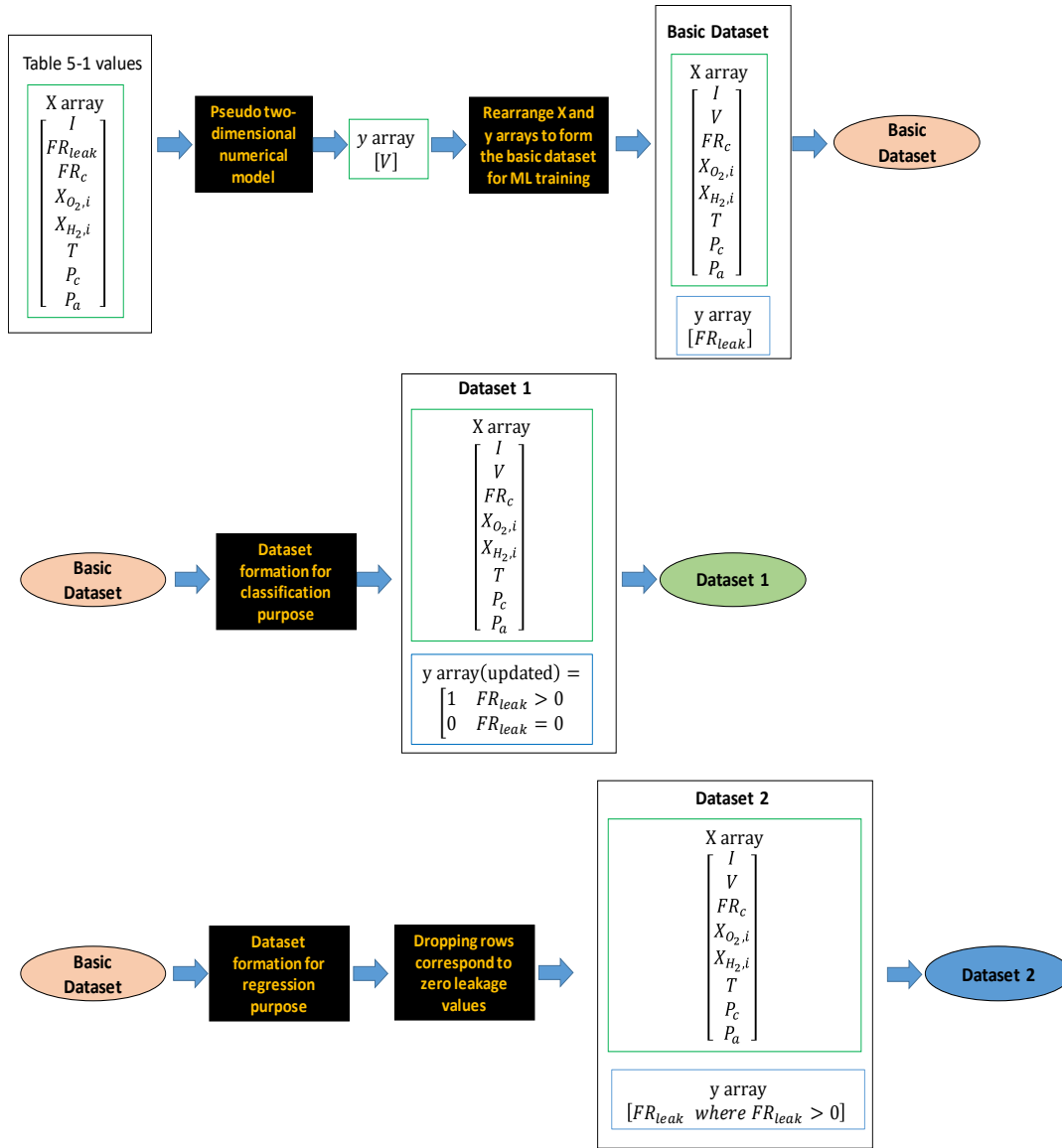


Figure 5-3. Dataset formation for ML estimators

Figure 5-4 shows the roadmap for developing ML leakage diagnosis estimators. The first step in this figure illustrates the process for developing the classifier that categorizes PEMFCs into healthy and leaky groups. The input array (X) is formed based on the values of current, voltage, cathode flow rate, anode hydrogen inlet concentration, cathode oxygen inlet concentration, PEMFC temperature, anode, and cathode pressures. The output array (y) is formed by binary values. If there is a leakage in the system, the y value would be equal to one, and for healthy PEMFCs, this value is equal to zero. Therefore, Dataset 1 is used for fault detection. KNN and ANN classifiers are trained based on input and output arrays to develop a leakage detection model. If leakage is detected, the second step and

third step would be conducted to quantify the leakage value and predict hydrogen pumping current values.

The purpose of the second stage is to quantify the amount of leakage. Since PEMFCs are already classified into leaky and healthy groups, the rows correspond to the healthy PEMFCs or zero leakage values are eliminated from the dataset, and dataset 2 is used for this purpose. The input array (x) is filled with the same parameters as those in the first step but only for leaky PEMFCs, while the output array (y) is filled with non-zero numeric values correspond to the leakage values. ANN and KNN regressors are trained based on the new dataset to quantify the amount of leakage.

In the last step, the leakage amount found by the regressor in the second step, along with other operating conditions, would be passed to the pseudo numerical model to predict the hydrogen pumping current.

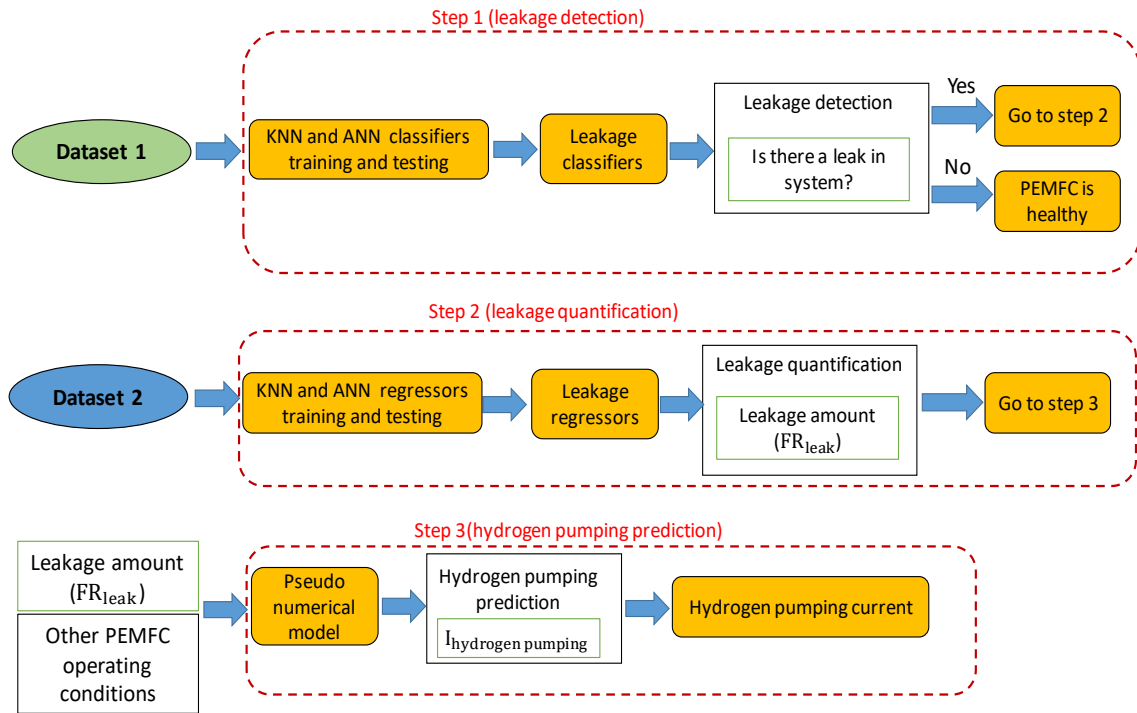


Figure 5-4. Leakage detection quantification, and hydrogen pumping prediction roadmap in steady-state



### 5.3. Preprocessing and Data Cleaning in Steady-State

According to the data presented in Table 5-1, the input variables take various values that some of them are significantly different in magnitude. For instance, cathode pressure changes from 1 atm to 4 atm, while hydrogen leak flow rates changes from 0 to 400 sccm. The ML algorithm does not understand the physics of the problem and solely works based on the input-output data that they receive. Several factors affect the performance of ML algorithms, and data preprocessing is the first and one of the most important steps [82]. ML algorithms might exhibit poor performance if the features do not look alike in terms of their magnitude and range. Z-score normalization or standardization [82] is employed to standardize the data. In this work, features are standardized using the following formula [82]:

$$x_{standardized} = \frac{x - \bar{x}}{\sigma} \quad (5-1)$$

where  $\bar{x}$  and  $\sigma$  represent the mean and standard deviation of the set. In this work, we employed the “StandardScaler” library in python to standardize the data. An example of scaled data is provided in Table 5-2.

Table 5-2. Sample of scaled data

Data type	$I$ (A)	$V$ (V)	$P_C$ (atm)	$P_A$ (atm)
Raw	21	0.4	1	4
Scaled	-0.174163	-0.881828	-1.42551	1.4254
Data type	$X_{O_2,in}$	$X_{H_2,in}$	$FR_{leak}$ (slm)	$FR_{cat}$ (slm)
Raw	0.21	0.9	340	1.2
Scaled	-0.79898	-1.412	0.74804	-0.581488

It is also necessary to clean and preprocess the data so that only useful information can be passed to the estimators and prevent noises that could disturb the learning process. The process is conducted as follows:

- The initial amount of data in the raw dataset is 628,992 data points (rows). Separating the leaky PEMFC data from healthy ones, 29,952 rows are allocated for the healthy fuel cells while the rest (599,040 rows) are allocated to leaky PEMFCs. Thus, the amount of information for leaky PEMFCs is about 20 times bigger than those for healthy PEMFCs. This issue would cause a serious problem for the classification process. For instance, if we label all rows as leaky data, that would result in 0.952 accuracy even though all the healthy PEMFCs are labeled incorrectly. To prevent this issue, we must ensure that the amount of data for both classes is not significantly different. Therefore, another 500,000 distinct data points are generated for healthy PEMFCs with no leakage to assure there is no bias in the dataset.
- Rows correspond to negative voltage values are eliminated from the dataset. This step is conducted since the intention is to diagnose leakage before it causes complete starvation and hydrogen pumping.
- For the classification problem, all data points are being used to train the estimator. The output will be “zero” if the cell operates in normal condition, while leaky cells are labeled as “one”. On the other hand, only data points corresponding to the leaky PEMFCs are used to train the regressor. The reason for employing a pair of classifier-regressor instead of one regressor is the fact that the ML regressor might not be able to exactly predict zero as an outcome, and therefore most of the PEMFC data, including the healthy ones, would be incorrectly labeled as leaky PEMFCs. In this case, employing a pair of classifier-regressor would allow us to separate healthy PEMFCs and leaky ones and then quantify the amount of leakage for leaky PEMFCs. Python 3.7 was employed in the current work to implement data preprocessing and data training.

## 5.4. Training/Testing Process in Steady-State

In this section, the training and testing procedure of steady-state data is explained for both classification and regression tasks. Different tuning strategies are explained, and performance indexes are investigated for each estimator. As mentioned earlier, KNN and ANN estimators are used and evaluated for both classification and regression purposes.

### 5.4.1. Classification (Leakage Detection)

The purpose of this section is to develop a classifier for leakage diagnosis. KNN and ANN classifiers are trained and tuned to predict the presence of leakage in PEMFC. Array y values are updated based on the following condition.

$$Binary\ value = \begin{cases} 1 & FR_{leak} > 0 \\ 0 & FR_{leak} = 0 \end{cases} \quad (5-2)$$

The binary value assists us in labeling data into two categories, negative and positive, which correspond to healthy and leaky fuel cells, respectively. We first discuss the results for the KNN classifier.

#### KNN classifier

Cross-validation and grid search methods are used to find the best parameters as well as the best setting for the KNN method. First, data is shuffled into five folds as  $[X_i, y_i]$  where  $i$  changes from 1 to 5. For each fold, we train all the other folds and test the model in a round-robin fashion, as illustrated in Figure 5-5. Grid search parameters are conducted by varying the number of neighbors from 3 to 21. Manhattan and Euclidean distances are the taken hyperparameters for the search grid method. Grid search method tries different possible combinations of model settings to find the combination that would result in the best model performance.



Figure 5-5. Cross-validation scheme

Cross-validation and grid search methods show that using seven neighbors and Manhattan distance can result in the best result. The best accuracy score is 0.957 in this

case. In order to investigate other performance indexes such as recall, F1-score, and precision, we divide the whole dataset into training and testing datasets. The training dataset forms 75% of the dataset, while the testing dataset includes the other 25%. The confusion matrix for the testing dataset is provided in Figure 5-6.

		Predicted class	
		Classes	
Actual class		Healthy PEMFCs	Leaky PEMFCs
	Healthy PEMFCs	118039	5186
	Leaky PEMFCs	3485	77852

Figure 5-6. Confusion matrix for KNN classifier

From Figure 5-6, the performance indexes can be obtained. These values are listed in Table 5-3.

Table 5-3. Performance indexes for KNN classifier

Precision	Accuracy	F1-Score	Recall	True Negative Rate
0.957	0.957	0.964	0.971	0.937

To ensure that  $k=7$  is the best result and we are not overfitting the model, testing accuracy is plotted for  $k$  values between 3 and 22. As Figure 5-7 indicates, using more than seven neighbors would result in a decline in the accuracy, and therefore  $k=7$  is the best value for the classification purpose.

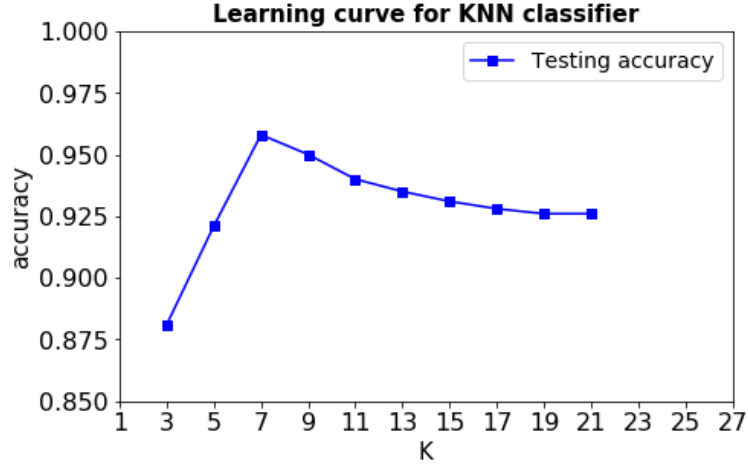


Figure 5-7. Learning curve for KNN classifier

### ANN classifier

ANNs are strong estimators due to their capabilities in training, parallel computation, and noise tolerance and therefore are beneficial in complex and non-linear problems. This kind of estimator can be used for both classification and regression problems. In this work, we employed a feed-forward neural network with a backpropagation algorithm that is used to minimize the cost function. The Cross-entropy cost function, which is chosen for the classification problem, is provided as follows:

$$\text{Cross entropy cost function} = - \sum_i y_i \log(\hat{y}_i) + (1 - y_i) \log(1 - \hat{y}_i) \quad (5-3)$$

$\hat{y}_i$  is the predicted label and  $y_i$  is the correct label. A schematic of the ANN classifier is shown in Figure 5-8. There are eight inputs, as discussed earlier. Two hidden layers with seven neurons each are shown in this figure. The activation functions for the middle layers are “ReLU” and the activation function for the last layer is “Sigmoid” that provides the probability of PEMFC being leaky. If the probability is larger than 0.5, PEMFC is categorized as leaky, whereas probabilities smaller than 0.5 corresponds to healthy PEMFCs. During training an ANN, all the weights are randomly initialized. It is necessary to mention that feed-forward ANN structure, activation functions, cost functions, and the optimization method are explained in detail in Appendix D.

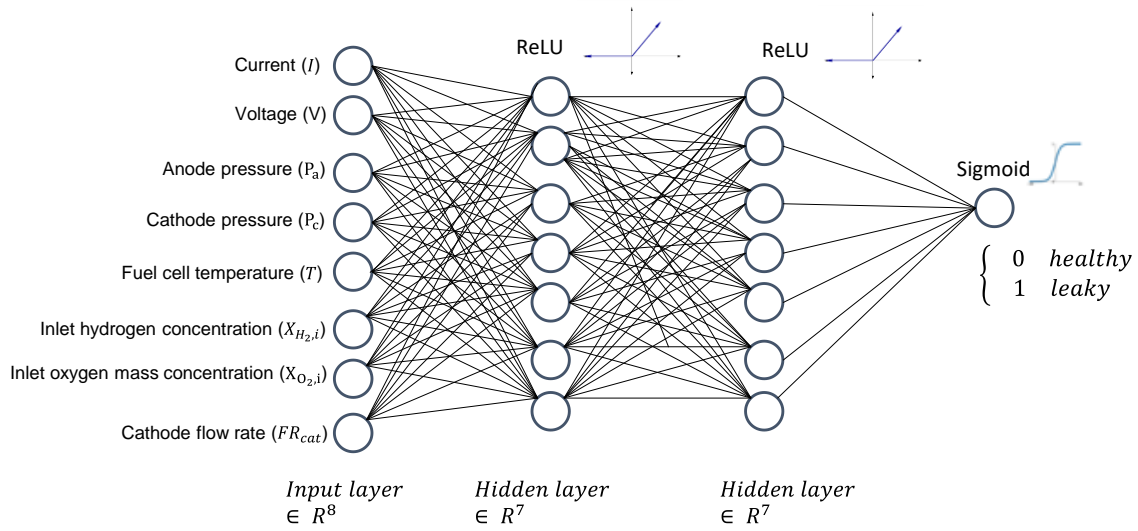


Figure 5-8. Neural network schematic

To find the best configuration for the ANN classifier, the grid search method is conducted to find the required number of neurons in each layer. Two hidden layers are chosen for the grid search method, and the number of neurons in each layer is varied from a minimum of four to a maximum of eight. ANN is trained with “Adam optimizer”, which is explained in Appendix D. ANN is run for 100 epochs for each case, and the accuracy of each ANN is recorded and illustrated in Figure 5-9.

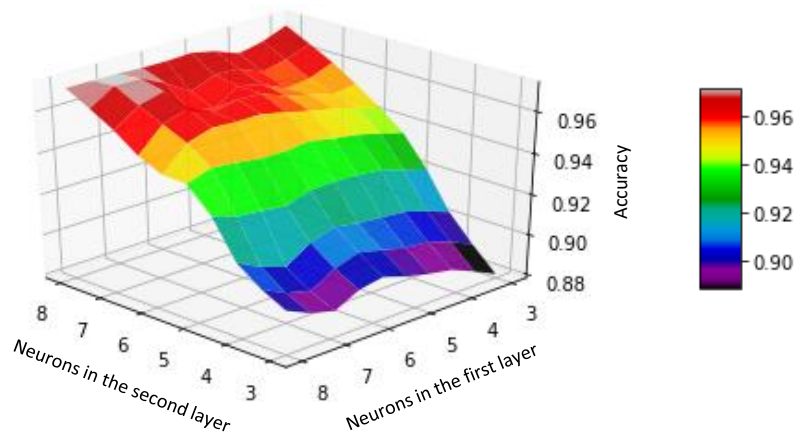
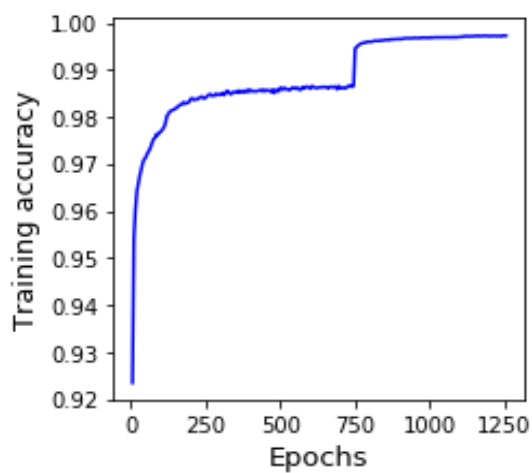


Figure 5-9. Accuracy of ANN classifier based on the number of neurons in each hidden layer

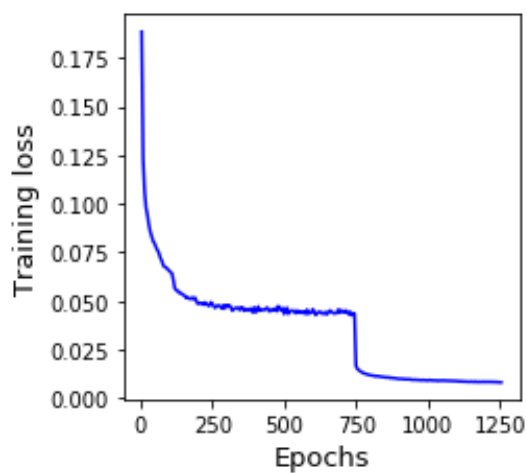
It is necessary to note that ANN could converge to different results (different weights and biases) with the same settings, and therefore the classifier must be tuned to provide the

best results. Nonetheless, performing the grid search method on the number of neurons in each layer provides the initial insight on how to choose the number of neurons in hidden layers. Figure 5-9 shows that increasing the number of neurons to values more than seven in each layer does not have any significant effect in increasing the accuracy of the model. The recorded accuracy for seven neurons in each hidden layer is 0.97. Therefore, seven neurons are chosen for each hidden layer, and the following strategies are taken to tune the ANN classifier and increase the accuracy of the model.

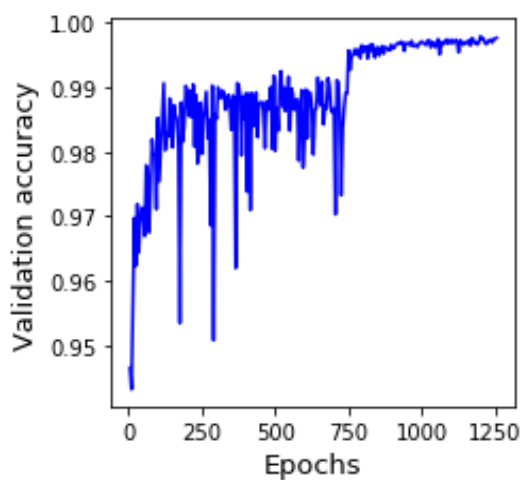
- ANNs tend to overfit easily. Therefore, from the whole dataset, 56.25% is used to train the model, 18.75% is used for evaluating the ANN performance and tuning the parameters. Eventually, 25% of the data is used to test the model report performance indexes.
- Keras library with Tensorflow backend is employed to form the neural network. Adam optimizer is chosen for adjusting the weight and bias values. Cross-entropy function is utilized for model validation and tuning. Tensorboard is used to monitor the validation loss and validation accuracy graphs. The model graph is provided in Appendix D. The training accuracy, training loss, validation accuracy, and validation loss plots are provided in Figure 5-10. The initial learning rate is set to 0.01. At epochs=750, when there is no improvement in validation loss, the learning rate is decreased to 0.001, and the batch size is increased from 35 to 75. This change resulted in a jump from 0.985 to 0.995 and stabilization of the validation loss. Repeating the same strategy did not result in any improvement in the validation, and all the metrics are flattened. The maximum validation accuracy is 0.997.



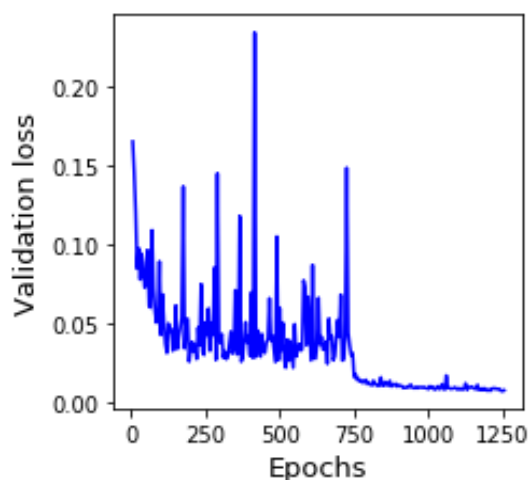
(a) Training accuracy



(b) Training loss



(c) Validation accuracy



(d) Validation loss

Figure 5-10. ANN classification metric plots



The confusion matrix on the test dataset is provided in Figure 5-11.

		Predicted class	
Actual class	Classes	Healthy PEMFCs	Leaky PEMFCs
	Healthy PEMFCs	124345	69
	Leaky PEMFCs	367	79781

Figure 5-11. Confusion matrix for ANN classifier

From Figure 5-11, the performance indexes can be obtained. These values are listed in Table 5-4.

Table 5-4. Performance indexes for ANN classifier

Precision	Accuracy	F1-Score	Recall	True Negative Rate
0.997	0.999	0.998	0.997	0.999

Comparing KNN, and ANN shows that KNN can compete with ANN in fast model development. However, if ANN is tuned properly, it outperforms KNN and detects leaky PEMFCs with very high accuracy.

#### 5.4.2. Regression (Leakage Quantification)

After the leaky PEMFCs are detected, we need to quantify and estimate the value of the leakage flow rate. KNN and ANN regressors are trained and tuned to quantify the leakage. For quantification, the data that corresponds to healthy PEMFCs is dropped from Dataset 1, and only the data for leaky PEMFCs are saved. This step is done since healthy PEMFCs are already detected and found in the classification stage. The new dataset has 321250

rows (data points). Dataset is shuffled and scaled and divided into training (75%) and test sets (25%).

### KNN regressor

Similar to classification, cross-validation and grid search methods are used to find the best parameters as well as the best setting for the KNN method. Grid search parameters are conducted by varying the number of neighbors from 3 to 21 neighbors. Manhattan and Euclidean distances are the taken hyperparameters for the search grid method. Cross-validation and grid search methods show that using five neighbors and Manhattan distance can result in the best  $R^2$  score, and MSE. The leakage value is then found by taking the average values of the neighbor data points. Several performance indexes are chosen to investigate the performance of the regressors. These indexes are  $R^2$  score, MSE, and MAE. Figure 5-12 shows the learning curve for the KNN regressor based on the number of neighbors.

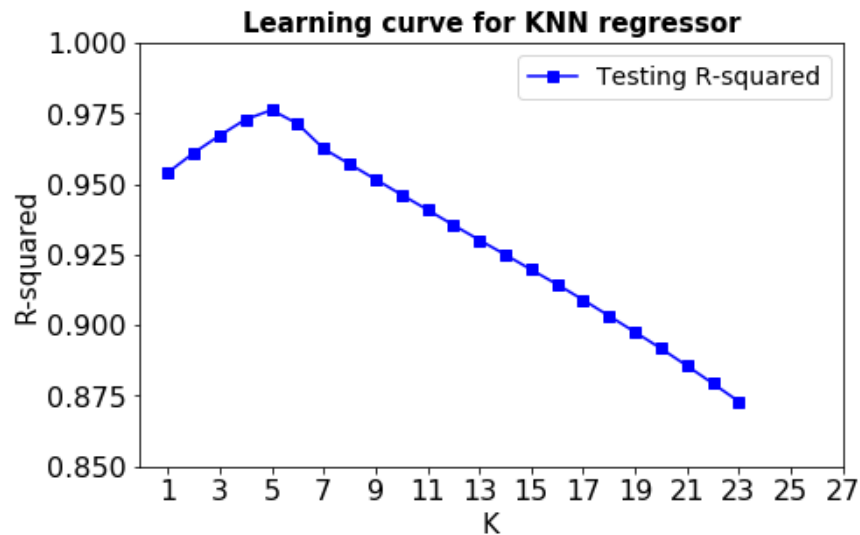


Figure 5-12. Learning curve for KNN regressor

As Figure 5-12 shows, the test accuracy slightly drops for  $k$  values higher than five. In fact, by taking  $k$  values bigger than five, some neighbors would aggravate the regression process. The regressor performance value indexes are provided in Table 5-5.

Table 5-5. Performance indexes for KNN regressor

R <sup>2</sup> score	MSE	MAE
0.976	232.98	11.47

### ANN regressor

Although the inputs are the same as the inputs in the ANN classification problem, the output and the activation function are different. The output for the regression problem is the hydrogen leakage flow rate, which is a numeric value. The activation function for the output layer is changed to “ReLU” since the output layer must generate positive numeric numbers. The best configuration for the ANN regressor is found based on the grid search method. Two hidden layers are chosen, and the number of neurons in each layer is varied from a minimum of six to a maximum of twelve. ANN is trained with “Adam optimizer”, and validation is conducted based on the MSE loss function for all cases. ANN is run for 100 epochs, and the MSE score is recorded for each configuration. The results are provided in Figure 5-13.

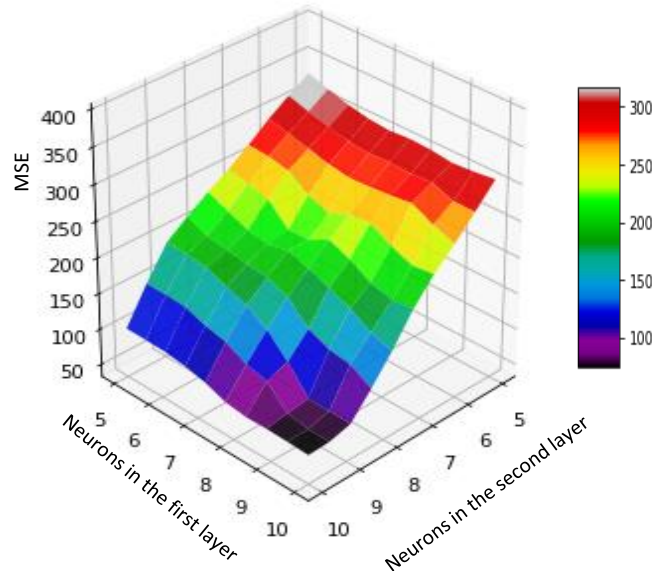


Figure 5-13. MSE of ANN regressor based on the number of neurons in each layer for leakage quantification

Similar to the ANN classifier, ANN regressor could converge to different values, and therefore, the MSE values might differ even with the same setting if we rerun the model. Therefore the regressor must be tuned to provide the best results. Nonetheless, performing the grid search method on the number of neurons in each layer provides the initial insight on how to choose the number of neurons in hidden layers. Based on Figure 5-13, the number of neurons in the first and the second layer is set to nine. Figure 5-13 shows that increasing the number of neurons to values more than nine in each layer does not result in a significant reduction in MSE values.

To further tune the ANN regressor and to prevent overfitting following strategies are taken:

- Like classification problem, 56.25% is used for training the model, 18.75% is used for evaluating the ANN performance and tuning the parameters, and eventually, 25% of data is used to test the model and report performance indexes.
- Keras library with Tensorflow backend is employed to form the neural network. Adam optimizer is chosen for adjusting the weight and bias values. MSE loss function is used for model validation and tuning. Tensorboard is used to monitor the validation loss and validation accuracy graphs. The model graph is similar to the one provided in Appendix D. The plots for training MSE loss and validation MSE loss are provided in Figure 5-14. The initial learning rate is set to 0.01. At epochs=100, the learning rate is changed to 0.001 with the same batch size. At epochs=600, the learning rate is set to 0.0001, and the batch size is increased from 35 to 75. Further decrease in learning rate and increase in batch size did not result in significant improvement in model performance. The minimum validation loss is 13.77.

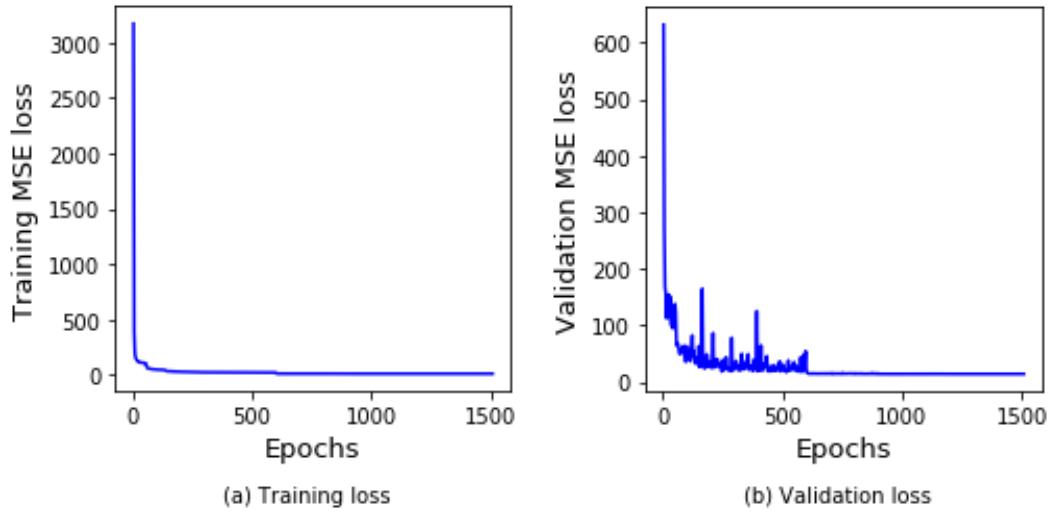


Figure 5-14. Training and validation loss plots for ANN regressor

After the ANN regressor is trained successfully, it is tested on the testing data, and performance indexes are provided in Table 5-6. The MSE and MAE values are noticeably smaller compared to the KNN regressor, which indicates that the ANN regressor is doing a much better job in leakage quantification.

Table 5-6. Performance indexes for ANN regressor

$R^2$ score	MSE	MAE
0.9987	13.77	2.85

### 5.4.3. Leakage Detection and Quantification Case Study

In the previous section, ANN and KNN estimators are developed to detect and quantify the leakage crossover through membrane pinholes or cracks. Comparing the performance indexes of these estimators illustrates that using a pair of ANN classifier-regressor would result in the best estimation. In this section, we will demonstrate how the leak detector would be used on a real fuel cell. The fuel cell, whose parameters are listed in Table 4-2, is assumed to operate at a constant load of 10A. It is further assumed that a small leak appears at  $t=20s$  and gradually progresses to a large leak, where at  $t=90s$ , the leak is saturating at 325 sccm as shown in Figure 5-15. The response of the fuel cell to this leak is provided in Figure 5-16. It may be noted that although the leak changes with time, the time-scale of the change in the leak rate is much smaller than the time-scale of

the dynamics of the fuel cells. Hence the steady-state leaks detection algorithm developed earlier can be used.

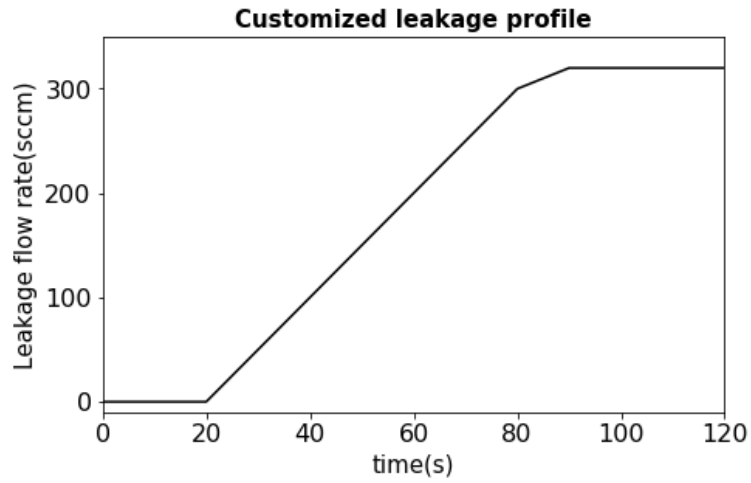


Figure 5-15. Customized leakage profile

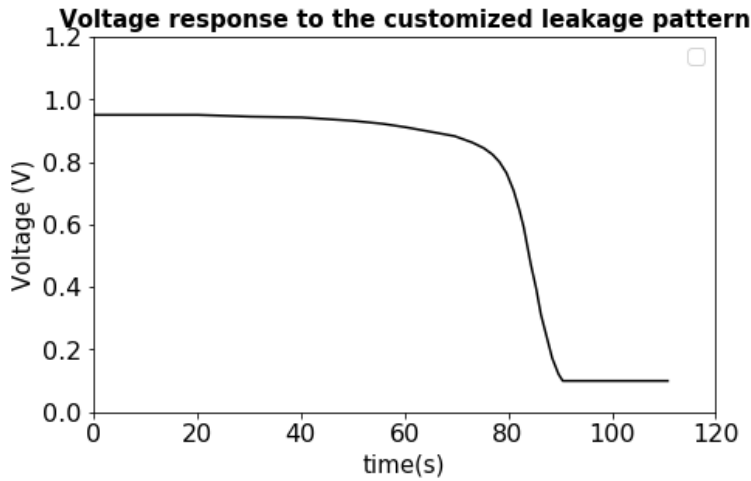


Figure 5-16. Voltage response to the customized leakage pattern at  $I = 10$  A

In the next step, the voltage response along with the other operating conditions, are fed to the pair of ANN classifier-regressor to detect and quantify the amount of leakage. A comparison of the predicted leakage values versus the exact introduced values is provided in Figure 5-17.

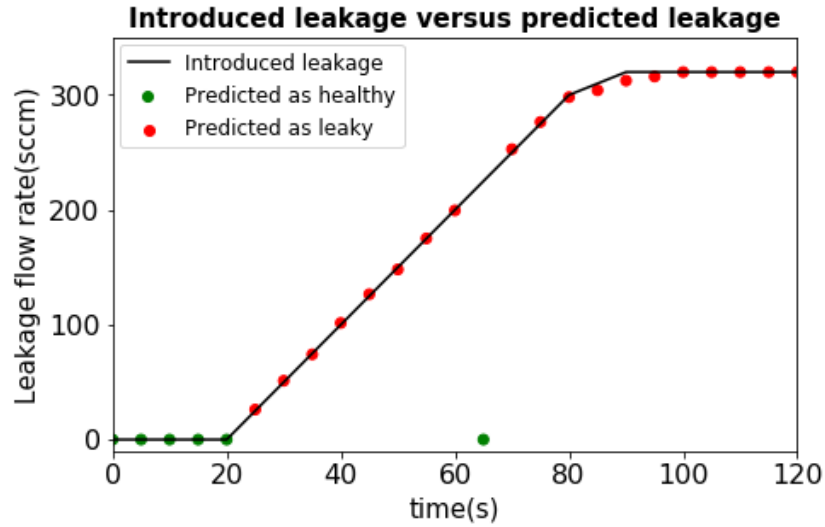


Figure 5-17. Comparison of the introduced leakage values and the predicted leakage values

As Figure 5-17 shows, the introduced pair of ANN classifier- regressor is able to predict the amount of leakage values. There is only one wrong prediction out of 25 predictions, which means the ANN classifier has an accuracy of 96% in this specific case. Putting aside the wrong prediction, the MSE and  $R^2$  score values of the ANN regressor are 1.417 and 0.999.

#### 5.4.4. Hydrogen Pumping Prediction

The purpose of this section is to find the current values that could result in the inception of hydrogen pumping in leaky PEMFCs. The previously developed regressors could be employed to predict the value of the leakage flow rate. By obtaining the amount of leakage flow rate, it is possible to find the current density that led to hydrogen pumping at each data point by using the pseudo numerical model. All the parameters are passed to the numerical model while current is increased incrementally to the point that voltage drops to the negative values. The algorithm is shown in Figure 5-18.

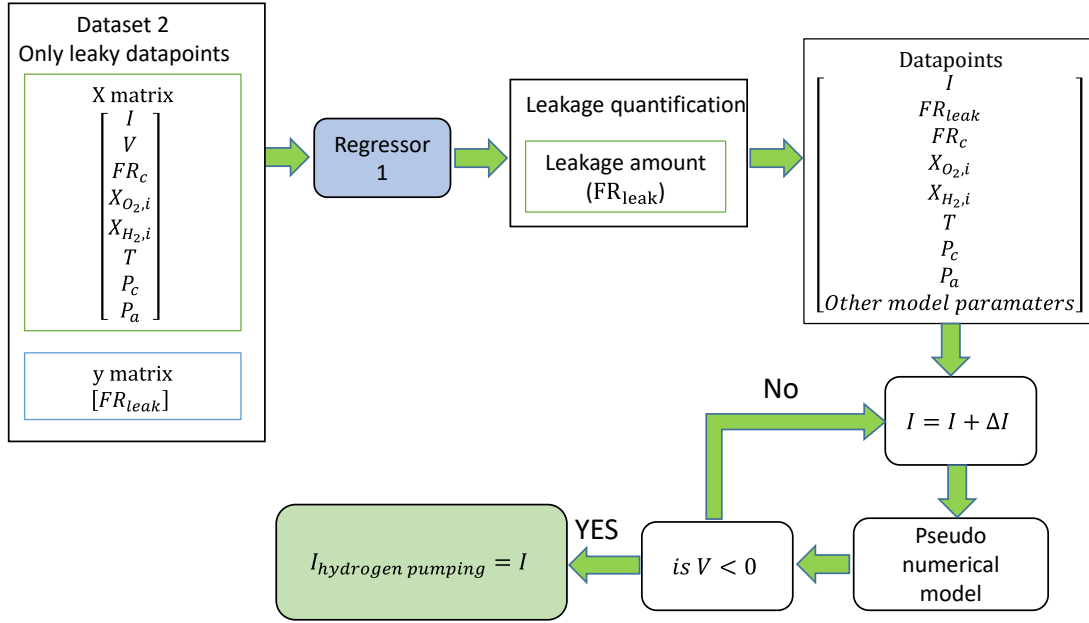


Figure 5-18. Hydrogen pumping prediction algorithm

The  $R^2$  score between hydrogen pumping currents and the predicted values is 0.9987, and MSE is found to be equal to 1.43.

## 5.5. Chapter Summary

In this chapter, the pseudo numerical two-dimensional model that was developed and validated in Chapter 4 was used to build two considerably large datasets to detect and quantify hydrogen leakage in PEMFC. Thanks to the very fast and accurate performance of the pseudo numerical model, we manage to build two datasets with eight features, including voltage, current, cathode flow rate, cathode and anode pressures, oxygen mole fractions in the cathode, hydrogen mole fraction at the anode, and PEMFC temperature. The first dataset contained more than 1 million data points with an almost equal portion for leaky and healthy PEMFCs. The dataset was used for leakage detection and classification. The second dataset contains about 500,000 leaky PEMFC data points and is used for leakage quantification. Building these two datasets enabled developing accurate ML estimators to develop a hybrid model for leakage diagnostics. First, the presence of the leakage is examined through binary classifiers, and in case of a leakage, a regressor was employed to quantify the amount of leakage and predict the current value that leaky PEMFC experience hydrogen pumping. ANN and KNN estimators were used



for both classification and regression problems. These two models are used to address the non-linear nature of PEMFCs. The following conclusions are made:

- By employing the grid search method and cross-validation, the KNN classifier can acquire accuracy of 0.957. KNN tuning process is easy and is not time-consuming. Using seven neighbors would result in the best performance, and F1-score is equal to 0.964.
- ANN classifier requires precise tuning, and the tuning process might be tricky and complex. It is important to observe the training and validation loss through the training process to prevent overfitting and to change the optimization parameters when needed. Two hidden layers are sufficient to achieve high accuracy of 0.999. The number of neurons in each layer is found by using the grid search method and cross-validation. Seven neurons in each layer are utilized for the classification problem.
- Although the difference between KNN and ANN accuracy seems to be very negligible (about 4 percent), the KNN classifier misclassifies about 8500 data points while ANN misclassifies only about 450 data points. The noticeable difference between these two numbers indicates that even a small improvement in performance indexes in a very large dataset is very important.
- KNN regressor works based on memorizing the training dataset. Increasing the number of neighbors to higher values than five resulted in the involvement of some bad neighbors in the estimation process. Employing five neighbors could result in the best performance of KNN regressor.
- ANN regressor with two layers and nine neurons in each layer would result in the best performance of the regressor.
- The pair of ANN regressor-pseudo model can be used to successfully predict the current that would trigger the hydrogen pumping phenomenon in PEMFCs.
- The pair of ANN classifier-regressor introduced in this work successfully acts as a virtual hydrogen leakage sensor for online tracking of the hydrogen leakage and to assure that the PEMFC current will not exceed the hydrogen pumping current.

## **Chapter 6. Conclusion and Future Work**

In this study, several novel solutions were offered to enhance the PEMFC performance by improving the maximum power density, preventing oxygen starvation, modeling, and diagnosis of hydrogen leakage. This work is done in three parts, and the findings and suggested future works for each part are explained in the following sections.

### **6.1. Part One: Non-Uniform Catalyst Distribution**

Non-uniform catalyst distribution along CCL was proposed as a method of improving the maximum PEMFC power density that also could provide a more homogeneous oxygen distribution at the CCL. The presence of oxygen molecules along the CCL at higher current densities resulted in the prevention of oxygen starvation and the improvement of maximum current density. A two-dimensional, two-phase, steady-state model was developed to investigate the effects of platinum loading distribution on oxygen distribution at CCL and therefore, PEMFC power density. Next, an optimization procedure was introduced to find the optimal catalyst distributions. The CFD model, constant amount of catalyst, and positive catalyst distribution formed the constraints, while decision variables were the coefficients of polynomial distributions. The employed optimization method was GA, and the unknown coefficients were obtained through the optimization procedure. The following findings were inferred:

- In the optimal case, maximum PEMFC power density was improved by 12.6%.
- In the optimal case, the minimum oxygen mass fraction along the CCL was increased by 42%.
- In the optimal case, the maximum current density was increased by 7.8%.
- Loading more catalyst in locations with higher reaction rates improved PEMFC power density.
- The amount of catalyst used in the first half of the catalyst layer was almost twice of the other half.

- An unlimited increase of the platinum mass loading at the CCH inlet and an unlimited decrease in the CCH outlet would not result in the PEMFC power density improvement.
- The increase in the maximum current density in the optimal case indicated that oxygen starvation would occur at a higher current density.

The following suggestions are provided for future works:

- Finding the optimal catalyst distribution using a three-dimensional, non-isothermal, and two-phase model.
- Conducting experimental studies to back up the optimization results. Conducting non-uniform catalyst deposition using nanofabrication methods and PEMFC power density measurements are amongst the suggestions for future works.

## **6.2. Part Two: Pseudo Two-Dimensional Modeling of a PEMFC**

A novel pseudo two-dimensional, steady-state, and dynamic model was presented to simulate PEMFC behavior under both driving and driven modes. The model was developed and was used as a base model in the leakage diagnosis part. The model results were validated versus the experimental data in the literature as well as the data provided by Ballard corporation. The hydrogen pumping effect was considered in the model, and the model results fit very well with the experimental data, which illustrated its capability for diagnosis purposes. The precision and computational effectiveness of the model make this model a strong candidate to be used as a base model in a diagnosis tool.

There are several suggestions for the further development of the model, which can be listed as follows:

- Inclusion of other faults such as drying, flooding, and fault in hydrogen delivery system
- Considering the temperature change as a result of oxygen combustion due to hydrogen leakage

- In-depth experimental tests on the effect of leakage on airflow distribution between cells and the way cells compete. As a suggestion, voltage measurements could be done in several locations in the stack and along each cell to understand the underlying phenomenon.

### **6.3. Part Three: Leakage Diagnosis, Quantification, and Hydrogen Pumping Prediction in Steady-State**

A novel combined model-based and non model-based diagnosis method was used to predict the presence of leakage in a PEMFC and quantify it. The combined method utilized the pseudo numerical model to simulate the effect of leakage on PEMFC voltage. The proposed method resembles model-based approaches since a PEMFC model is developed to simulate the effect of different leakage sizes on the voltage. However, the model was not used to calculate the residual directly and to determine if PEMFC was leaky or healthy. Instead, the model was used to create two big datasets of information. Different leak sizes along with seven other features (current, cathode flow rate, anode and cathode pressures, inlet oxygen mole fraction in the cathode, inlet hydrogen mole fraction in the anode, and fuel cell temperature) were passed to the model, and the voltage value was recorded for each data point. These datasets were then used to predict and quantify the leakage, and that was where the combined model resembled the non-model based approaches. The difference between the proposed method and non-model based approaches was related to the way that the datasets were formed. Datasets were not formed through experimental data, and they were generated through a fast, precise, and validated PEMFC model.

A pair of classifier-regressor approach was developed to first detect leakage and then quantify the amount of the leakage. KNN and ANN estimators were used as estimators for both classification and regression purposes. These two types of estimators were chosen since they were non-linear classifiers/regressors and could handle the non-linear nature of PEMFCs. The performance of developed classifiers was investigated using the performance indexes such as accuracy, precision, recall, and F1-score, while the performance of the developed regressors was investigated by  $R^2$  score, MSE, and MAE values. Following results were obtained

- KNN classifier accuracy was 0.958, while ANN classifier accuracy was 0.997.

- KNN regressor  $R^2$  score was 0.976 while  $R^2$  score for ANN regressor was 0.994.
- For fast tuning and prediction of leakage, KNN could compete with ANN. However, proper tuning of ANN would lead to a better performance of the estimator.
- The pair of ANN classifier-regressor could successfully isolate leaky PEMFCs and quantify the amount of leakage.
- The combined ANN regressor-pseudo numerical model could successfully predict the hydrogen pumping current for leaky PEMFCs.

The followings are very interesting suggestions for future works:

- Developing a similar pair of classifier-regressor to detect and quantify the leakage values in a PEMFC in dynamic mode; As an initial suggestion, voltage response under different types of loads (step current, linear, etc.) could be recorded and sampled for creating the dataset.
- The effect of other faults (drying, flooding, etc.) could be added to the numerical model to create a bigger dataset of information containing the information of different types of faults and their effects on voltage or other characteristics. The developed dataset could be used for a multi-class classification problem where the data is categorized under different faults.
- Conducting online leakage detection and quantification on commercial stacks and experimental data

## References

- [1] Mench MM. Fuel Cell Engines. John Wiley & Sons, Inc.; 2008. <https://doi.org/10.1002/9780470209769>.
- [2] Cristian Kunusch, Paul Puleston MM. Sliding-Mode Control of PEM Fuel Cells. Springer-Verlag London; 2012. <https://doi.org/10.1007/978-1-4471-2431-3>.
- [3] Malekian A. Compressive behaviour of thin porous layers with application to PEM fuel cells. Ph.D. Thesis, Mechatronic Systems Engineering Department, Simon Fraser University, 2019.
- [4] Wang Y, Chen KS, Mishler J, Cho SC, Adroher XC. A review of polymer electrolyte membrane fuel cells: Technology, applications, and needs on fundamental research. Appl Energy 2011;88:981–1007. <https://doi.org/10.1016/j.apenergy.2010.09.030>.
- [5] Larminie J, Dicks A. Fuel Cell Systems Explained. J Power Sources 2001;93:285. [https://doi.org/10.1016/S0378-7753\(00\)00571-1](https://doi.org/10.1016/S0378-7753(00)00571-1).
- [6] Giorgi L. Fuel Cells: Technologies and Applications. Open Fuel Cells J 2013;6:1–20. <https://doi.org/10.2174/1875932720130719001>.
- [7] Wilkinson DP, Zhang J, Hui R, Fergus J, Li X. Proton Exchange Membrane Fuel Cells: Materials Properties and Performance. Baton Rouge: CRC Press; 2009. <https://doi.org/10.1201/9781439806661>.
- [8] Benmouna A, Becherif M, Depernet D, Gustin F. Fault diagnosis methods for Proton Exchange Membrane Fuel Cell system. Int J Hydrogen Energy 2017;42:1534–43. <https://doi.org/10.1016/j.ijhydene.2016.07.181>.
- [9] US Department of Energy. Progress Report for the DOE Hydrogen and Fuel Cells Program For Year 2017. Washington, DC 20585-0121: 2017.
- [10] US Department of Energy. Progress Report for the DOE Hydrogen and Fuel Cells Program For Year 2011. Washington, DC 20585-0121: 2011.
- [11] Ahn SY, Shin SJ, Ha HY, Hong SA, Lee YC, Lim TW, et al. Performance and lifetime analysis of the kW-class PEMFC stack. J Power Sources 2002;106:295–303. [https://doi.org/10.1016/S0378-7753\(01\)01032-1](https://doi.org/10.1016/S0378-7753(01)01032-1).
- [12] Narimani M, Devaal J, Golnaraghi F. ScienceDirect Hydrogen emission characterization for proton exchange membrane fuel cell during oxygen starvation e Part 1 : Low oxygen concentration. Int J Hydrogen Energy 2016;41:4843–53. <https://doi.org/10.1016/j.ijhydene.2016.01.057>.
- [13] Narimani M, Devaal J, Golnaraghi F. ScienceDirect Hydrogen emission

characterization for proton exchange membrane fuel cell during oxygen starvation  
e Part 2 : Effect of hydrogen transfer leak. *Int J Hydrogen Energy* 2016;41:18641–53. <https://doi.org/10.1016/j.ijhydene.2016.06.227>.

- [14] Ebrahimi S, Devaal J, Narimani M, Vijayaraghavan K. ScienceDirect Transient model of oxygen-starved proton exchange membrane fuel cell for predicting voltages and hydrogen emissions. *Int J Hydrogen Energy* 2017;42:21177–90. <https://doi.org/10.1016/j.ijhydene.2017.05.209>.
- [15] Vijayaraghavan K, DeVaal J, Narimani M. Dynamic model of oxygen starved proton exchange membrane fuel-cell using hybrid analytical-numerical method. *J Power Sources* 2015;285:291–302. <https://doi.org/10.1016/j.jpowsour.2015.03.103>.
- [16] Standaert F, Hemmes K, Woudstra N. Analytical fuel cell modeling. *J Power Sources* 1996;63:221–34. [https://doi.org/10.1016/S0378-7753\(96\)02479-2](https://doi.org/10.1016/S0378-7753(96)02479-2).
- [17] Cheddie D, Munroe N. Review and comparison of approaches to proton exchange membrane fuel cell modeling. *J Power Sources* 2005;147:72–84. <https://doi.org/10.1016/j.jpowsour.2005.01.003>.
- [18] Bernardi DM. A Mathematical Model of the Solid-Polymer-Electrolyte Fuel Cell. *J Electrochem Soc* 1992;139:2477. <https://doi.org/10.1149/1.2221251>.
- [19] Eikerling M. Phenomenological Theory of Electro-osmotic Effect and Water Management in Polymer Electrolyte Proton-Conducting Membranes. *J Electrochem Soc* 1998;145:2684. <https://doi.org/10.1149/1.1838700>.
- [20] Springer TE, Zawodzinski T a., Gottesfeld S. Polymer electrolyte fuel cell model. *J Electrochem Soc* 1991;138:2334–42. <https://doi.org/10.1149/1.2085971>.
- [21] Roshandel R, Farhanieh B. The effects of non-uniform distribution of catalyst loading on polymer electrolyte membrane fuel cell performance. *Int J Hydrogen Energy* 2007;32:4424–37. <https://doi.org/10.1016/j.ijhydene.2007.06.027>.
- [22] Futerko P, Hsing I-M. Two-dimensional finite-element method study of the resistance of membranes in polymer electrolyte fuel cells. *Electrochim Acta* 2000;45:1741–51. [https://doi.org/10.1016/S0013-4686\(99\)00394-1](https://doi.org/10.1016/S0013-4686(99)00394-1).
- [23] Das PK, Li X, Liu ZS. A three-dimensional agglomerate model for the cathode catalyst layer of PEM fuel cells. *J Power Sources* 2008;179:186–99. <https://doi.org/10.1016/j.jpowsour.2007.12.085>.
- [24] Berning T, Lu DM, Djilali N. Three-dimensional computational analysis of transport phenomena in a PEM fuel cell. *J Power Sources* 2002;106:284–94. [https://doi.org/10.1016/S0378-7753\(01\)01057-6](https://doi.org/10.1016/S0378-7753(01)01057-6).
- [25] Chen H, Zhao X, Zhang T, Pei P. The reactant starvation of the proton exchange

membrane fuel cells for vehicular applications: A review. *Energy Convers Manag* 2019;182:282–98. <https://doi.org/10.1016/j.enconman.2018.12.049>.

- [26] Schmittinger W, Vahidi A. A review of the main parameters influencing long-term performance and durability of PEM fuel cells. *J Power Sources* 2008;180:1–14. <https://doi.org/10.1016/j.jpowsour.2008.01.070>.
- [27] Meyers JP, Darling RM. Model of Carbon Corrosion in PEM Fuel Cells. *J Electrochem Soc* 2006;153:A1432. <https://doi.org/10.1149/1.2203811>.
- [28] Ohs JH, Sauter U, Maass S, Stolten D. Modeling hydrogen starvation conditions in proton-exchange membrane fuel cells. *J Power Sources* 2011;196:255–63. <https://doi.org/10.1016/j.jpowsour.2010.06.038>.
- [29] Reiser, C.A., Bregoli, L., Patterson, T.W., Yi, J.S. Yang, J.D., Perry, M.L., Jarvi TD. A reverse-current decay mechanism for fuel cells. *Electrochem Solid-State Lett* 2005;8:A273–6. <https://doi.org/10.1149/1.1896466>.
- [30] Liang D, Shen Q, Hou M, Shao Z, Yi B. Study of the cell reversal process of large area proton exchange membrane fuel cells under fuel starvation. *J Power Sources* 2009;194:847–53. <https://doi.org/10.1016/j.jpowsour.2009.06.059>.
- [31] Tang H, Qi Z, Ramani M, Elter JF. PEM fuel cell cathode carbon corrosion due to the formation of air / fuel boundary at the anode. *J Power Sources* 2006;158:1306–12. <https://doi.org/10.1016/j.jpowsour.2005.10.059>.
- [32] Knights SD, Colbow KM, St-Pierre J, Wilkinson DP. Aging mechanisms and lifetime of PEFC and DMFC. *J Power Sources* 2004;127:127–34. <https://doi.org/10.1016/j.jpowsour.2003.09.033>.
- [33] Huang, J.-B., Yang, D.-J, Chang, F.-R., Ma J-X. Durability of a fuel cell stack with low hydrogen stoichiometry under driving cycle conditions. *J Chem Eng Chinese Univ* 2015;29:1364–70. <https://doi.org/10.1002/fuce.201600132>.
- [34] Bodner M, Schenk A, Salaberger D, Rami M, Hochenauer C, Hacker V. Air Starvation Induced Degradation in Polymer Electrolyte Fuel Cells. *Fuel Cells* 2017:18–26. <https://doi.org/10.1002/fuce.201600132>.
- [35] Yousfi-Steiner N, Moçotéguy P, Candusso D, Hissel D. A review on polymer electrolyte membrane fuel cell catalyst degradation and starvation issues: Causes, consequences and diagnostic for mitigation. *J Power Sources* 2009;194:130–45. <https://doi.org/10.1016/j.jpowsour.2009.03.060>.
- [36] Rao RM, Rengaswamy R. A distributed dynamic model for chronoamperometry , chronopotentiometry and gas starvation studies in PEM fuel cell cathode. *J Chem Eng Sci* 2006;61:7393–409. <https://doi.org/10.1016/j.ces.2006.06.021>.
- [37] Mousa G, Golnaraghi F, Devaal J, Young A. Detecting proton exchange



membrane fuel cell hydrogen leak using electrochemical impedance spectroscopy method. *J Power Sources* 2014;246:110–6.  
<https://doi.org/10.1016/j.jpowsour.2013.07.018>.

- [38] Taniguchi A, Akita T, Yasuda K, Miyazaki Y. Analysis of degradation in PEMFC caused by cell reversal during air starvation. *Int J Hydrogen Energy* 2008;33:2323–9. <https://doi.org/10.1016/j.ijhydene.2008.02.049>.
- [39] Inaba M, Kinumoto T, Kiriake M, Umebayashi R, Tasaka A, Ogumi Z. Gas crossover and membrane degradation in polymer electrolyte fuel cells. *Electrochim Acta* 2006;51:5746–53.  
<https://doi.org/10.1016/j.electacta.2006.03.008>.
- [40] Liu Z, Yang L, Mao Z, Zhuge W, Zhang Y, Wang L. Behavior of PEMFC in starvation 2006;157:166–76. <https://doi.org/10.1016/j.jpowsour.2005.08.006>.
- [41] Kulikovskiy A. A. Optimal shape of catalyst loading across the active layer of a fuel cell. *Electrochem Commun* 2009;11:1951–5.  
<https://doi.org/10.1016/j.elecom.2009.08.026>.
- [42] Srinivasarao M, Bhattacharyya D, Rengaswamy R, Narasimhan S. Multivariable optimization studies of cathode catalyst layer of a polymer electrolyte membrane fuel cell. *Chem Eng Res Des* 2011;89:10–22.  
<https://doi.org/10.1016/j.cherd.2010.04.020>.
- [43] Roshandel R, Ahmadi F. Effects of catalyst loading gradient in catalyst layers on performance of polymer electrolyte membrane fuel cells. *Renew Energy* 2013;50:921–31. <https://doi.org/10.1016/j.renene.2012.08.040>.
- [44] Zhang Y, Smirnova A, Verma A, Pitchumani R. Design of a proton exchange membrane (PEM) fuel cell with variable catalyst loading. *J Power Sources* 2015;291:46–57. <https://doi.org/10.1016/j.jpowsour.2015.05.002>.
- [45] Mathieu-Potvin F, Gosselin L. Optimal topology and distribution of catalyst in PEMFC. *Int J Hydrogen Energy* 2014;9.  
<https://doi.org/10.1016/j.ijhydene.2014.02.098>.
- [46] Natarajan D, Nguyen T Van. Current Distribution in PEM Fuel Cells . Part 1 : *AIChE J* 2005;51:2587–98. <https://doi.org/10.1002/aic.10545>.
- [47] Natarajan D, Nguyen T Van. Current Distribution in PEM Fuel Cells . Part 2 : *AIChE J* 2005;51. <https://doi.org/10.1002/aic.10577>.
- [48] S.X.Ding. *Model-based Fault Diagnosis Techniques*. Berlin : Springer; 2008.  
<https://doi.org/10.1007/978-3-540-76304-8>.
- [49] Zheng Z, Petrone R, Péra M., Hissel D, Becherif M, Pianese C, et al. A review on non-model based diagnosis methodologies for PEM fuel cell stacks and systems.

Int J Hydrogen Energy 2013;38:8914–26.  
<https://doi.org/10.1016/j.ijhydene.2013.04.007>.

- [50] Isermann R. Model-based fault detection and diagnosis – status and applications. *Annu Rev Control* 2005;29:71–85. <https://doi.org/10.1016/j.arcontrol.2004.12.002>.
- [51] Petrone R, Zheng Z, Hissel D, Péra MC, Pianese C, Sorrentino M, et al. A review on model-based diagnosis methodologies for PEMFCs. *Int J Hydrogen Energy* 2013;38. <https://doi.org/10.1016/j.ijhydene.2013.03.106>.
- [52] Hernandez A, Hissel D, Outbib R. Fuel cell fault diagnosis: A stochastic approach. *2006 IEEE Int Symp Ind Electron* 2006:1984–9. <https://doi.org/10.1109/ISIE.2006.295877>.
- [53] Zhongliang LI. Data-driven fault diagnosis for PEMFC systems. Ph.D. thesis, Aix-Marseille University, 2014.
- [54] Tian G, Wasterlain S, Endichi I, Candusso D, Harel F, François X, et al. Diagnosis methods dedicated to the localisation of failed cells within PEMFC stacks. *J Power Sources* 2008;182:449–61. <https://doi.org/10.1016/j.jpowsour.2007.12.038>.
- [55] Ashraf Khorasani MR, Asghari S, Mokmeli A, Shahsamandi MH, Faghih Imani B. A diagnosis method for identification of the defected cell(s) in the PEM fuel cells. *Int J Hydrogen Energy* 2010;35:9269–75. <https://doi.org/10.1016/j.ijhydene.2010.04.157>.
- [56] Niroumand AM, Pooyanfar O, Macauley N, Devaal J, Golnaraghi F. In-situ diagnostic tools for hydrogen transfer leak characterization in PEM fuel cell stacks part I: R&D applications. *J Power Sources* 2015;278:652–9. <https://doi.org/10.1016/j.jpowsour.2014.12.093>.
- [57] Niroumand AM, Mérida W, Eikerling M, Saif M. Pressure-voltage oscillations as a diagnostic tool for PEFC cathodes. *Electrochem Commun* 2010;12:122–4. <https://doi.org/10.1016/j.elecom.2009.11.003>.
- [58] Rezaei Niya SM, Hoorfar M. Study of proton exchange membrane fuel cells using electrochemical impedance spectroscopy technique - A review. *J Power Sources* 2013;240:281–93. <https://doi.org/10.1016/j.jpowsour.2013.04.011>.
- [59] Yan Q, Toghiani H, Causey H. Steady state and dynamic performance of proton exchange membrane fuel cells (PEMFCs) under various operating conditions and load changes. *J Power Sources* 2006;161:492–502. <https://doi.org/10.1016/j.jpowsour.2006.03.077>.
- [60] Mousa G, DeVaal J, Golnaraghi F. Diagnosis of hydrogen crossover and emission in proton exchange membrane fuel cells. *Int J Hydrogen Energy* 2014;39:21154–64. <https://doi.org/10.1016/j.ijhydene.2014.09.046>.

- [61] Mousa G. Fuel Cell Diagnostics using Electrochemical Impedance Spectroscopy. Ph.D. thesis, Mechatronic systems engineering, Simon Fraser University, 2014.
- [62] Liu J, Li Q, Chen W, Cao T. A discrete hidden Markov model fault diagnosis strategy based on K-means clustering dedicated to PEM fuel cell systems of tramways. *Int J Hydrogen Energy* 2018;43:12428–41. <https://doi.org/10.1016/j.ijhydene.2018.04.163>.
- [63] Zhang X, Zhou J, Chen W. Data-driven fault diagnosis for PEMFC systems of hybrid tram based on deep learning. *Int J Hydrogen Energy* 2020;45:13483–95. <https://doi.org/10.1016/j.ijhydene.2020.03.035>.
- [64] Shao M, Zhu X, Cao H, Shen H. An artificial neural network ensemble method for fault diagnosis of proton exchange membrane fuel cell system. *Energy* 2014;67:268–75. <https://doi.org/10.1016/j.energy.2014.01.079>.
- [65] Kamal MM, Yu DW, Yu DL. Fault detection and isolation for PEM fuel cell stack with independent RBF model. *Eng Appl Artif Intell* 2014;28:52–63. <https://doi.org/10.1016/j.engappai.2013.10.002>.
- [66] Wang Y, Basu S, Wang C. Modeling two-phase flow in PEM fuel cell channels. *J Power Sources* 2008;179:603–17. <https://doi.org/10.1016/j.jpowsour.2008.01.047>.
- [67] You L, Liu H. A two-phase flow and transport model for the cathode of PEM fuel cells. *Int J Heat Mass Transf* 2002;45:2277–87. [https://doi.org/10.1016/S0017-9310\(01\)00322-2](https://doi.org/10.1016/S0017-9310(01)00322-2).
- [68] Wang C, Nehrir MH, Shaw SR. Dynamic Models and Model Validation for PEM Fuel Cells Using Electrical Circuits. *IEEE Trans Energy Convers* 2005;20:442–51. <https://doi.org/10.1109/TEC.2004.842357>.
- [69] Chao-Yang W, Beckermann C. A two-phase mixture model of liquid-gas flow and heat transfer in capillary porous media-I. Formulation. *Int J Heat Mass Transf* 1993;36:2747–58. [https://doi.org/10.1016/0017-9310\(93\)90094-M](https://doi.org/10.1016/0017-9310(93)90094-M).
- [70] Versteeg HK, Malalasekera W. An Introduction to Computational Fluids Dynamics: The finite volume method. Second Edi. Pearson (Feb. 6 2007); 2007.
- [71] You L, Liu H. A two-phase flow and transport model for PEM fuel cells. *J Power Sources* 2006;155:219–30. <https://doi.org/10.1016/j.jpowsour.2005.04.025>.
- [72] You L. The two-phase flow, transport mechanism and performance studies for PEM fuel cells. Ph.D. thesis, University of Miami, 2001.
- [73] Wang ZH, Wang CY, Chen KS. Two-phase flow and transport in the air cathode of proton exchange membrane fuel cells. *J Power Sources* 2001;94:40–50. [https://doi.org/10.1016/S0378-7753\(00\)00662-5](https://doi.org/10.1016/S0378-7753(00)00662-5).

- [74] Chao-Yang W, Beckermann C. A two-phase mixture model of liquid-gas flow and heat transfer in capillary porous media—II. Application to pressure-driven boiling flow adjacent to a vertical heated plate. *Int J Heat Mass Transf* 1993;36:2759–68. [https://doi.org/10.1016/0017-9310\(93\)90095-N](https://doi.org/10.1016/0017-9310(93)90095-N).
- [75] Pasaogullari U. Two-Phase Transport and Prediction of Flooding in Polymer Electrolyte Fuel Cells, Ph.D. Thesis in Mechanical Engineering. The Pennsylvania State University, 2005.
- [76] Chen F, Chang MH, Hsieh PT. Two-phase transport in the cathode gas diffusion layer of PEM fuel cell with a gradient in porosity. *Int J Hydrogen Energy* 2008;33:2525–9. <https://doi.org/10.1016/j.ijhydene.2008.02.077>.
- [77] Wang ZH, Wang CY. Two-phase flow and transport in the interdigitated air cathode of proton exchange membrane fuel cells. *Am Soc Mech Eng Heat Transf Div HTD* 2000;366:27–33.
- [78] Abdollahzadeh M, Pascoa JC, Ranjbar AA, Esmaili Q. Analysis of PEM (Polymer Electrolyte Membrane) fuel cell cathode two-dimensional modeling. *Energy* 2014;68:478–94. <https://doi.org/10.1016/j.energy.2014.01.075>.
- [79] Ebrahimi S, Ghorbani B, Vijayaraghavan K. Optimization of catalyst distribution along PEMFC channel through a numerical two-phase model and genetic algorithm. *Renew Energy* 2017;113:846–54. <https://doi.org/10.1016/j.renene.2017.06.067>.
- [80] Amphlett JC, Baumert RM, Mann RF, Peppley BA, Roberge PR. Performance Modeling of the Ballard Mark IV Solid Polymer Electrolyte Fuel Cell. *J Electrochem Soc* 1995;142:1–8. <https://doi.org/10.1149/1.2043866>.
- [81] Mukhopadhyay S. *Advanced Data Analytics Using Python*. 1st ed. Berkeley, CA : Apress : Imprint: Apress; 2018. <https://doi.org/10.1007/978-1-4842-3450-1>.
- [82] Shalev-Shwartz S, Ben-David S. *Understanding Machine Learning: From Theory to Algorithms*. Cambridge University Press; 2014. <https://doi.org/10.1017/CBO9781107298019>.
- [83] Deb K. An introduction to genetic algorithms. *Sadhana - Acad. Proc. Eng. Sci.*, vol. 24, New Delhi: Springer Science and Business Media LLC; 1999, p. 293–315. <https://doi.org/10.1007/BF02823145>.
- [84] Deng L. *Deep Learning: Methods and Applications*, Hanover, Massachusetts: Now Publishers; 2014, p. 197–387. <https://doi.org/10.1561/20000000039>.
- [85] Rao MA, Srinivas J. *Neural networks : algorithms and applications*. Pangbourne, Eng. : Alpha Science International; 2003.
- [86] Masutani Y, Nemoto M, Nomura Y, Hayashi N. *Clinical Machine Learning in*

Action. Manning Publications (April 19 2012); 2012. <https://doi.org/10.4018/978-1-4666-0059-1.ch008>.

## Appendix A. SIMPLE Method and Hybrid Scheme

In this appendix, we explain the numerical scheme used in Chapter 3 of the thesis in more detail. We start the discussion about the staggered grid by considering the governing equations for a two-dimensional laminar flow in steady-state [70]:

$$\frac{\partial}{\partial x}(\phi uu) + \frac{\partial}{\partial y}(\phi vu) = \frac{\partial}{\partial x}\left(\mu \frac{\partial u}{\partial x}\right) + \frac{\partial}{\partial y}\left(\mu \frac{\partial u}{\partial y}\right) - \frac{\partial p}{\partial x} + S_u \quad (\text{A-1})$$

$$\frac{\partial}{\partial x}(\phi uv) + \frac{\partial}{\partial y}(\phi vv) = \frac{\partial}{\partial x}\left(\mu \frac{\partial v}{\partial x}\right) + \frac{\partial}{\partial y}\left(\mu \frac{\partial v}{\partial y}\right) - \frac{\partial p}{\partial y} + S_v \quad (\text{A-2})$$

$$\frac{\partial}{\partial x}(\phi u) + \frac{\partial}{\partial y}(\phi v) = 0 \quad (\text{A-3})$$

$S_u$  and  $S_v$  terms are source/sink terms. The problem with these sets of equations is that the convection term is non-linear, and all three equations must be coupled together. The main problem is related to the pressure gradient terms that appear in the first two equations, but there is no separate equation to solve for this term. The mentioned problems can be resolved by employing methods such as SIMPLE, SIMPLER, and SIMPLEC [70]. Similar to other methods, the finite volume method starts with the discretization of equations. First, it is important to select the locations of saving velocity components. Numerical problems might occur If we define velocities at the same nodes that scalars such as temperature and pressure are defined. Here we provide an example from famous checker-board pressure field in a structured mesh in Figure A-1. Pressures at node w,n,s, and e are calculated by interpolation between W, N, S, and E. Thus, the pressure gradients can be calculated as follows:

$$\frac{\partial p}{\partial x} = \frac{p_e - p_w}{\partial x} = \frac{\left(\frac{p_E + p_P}{2}\right) - \left(\frac{p_P + p_W}{2}\right)}{\partial x} = \frac{p_E - p_W}{2\partial x} \quad (\text{A-4})$$

$$\frac{\partial p}{\partial y} = \frac{p_n - p_s}{\partial y} = \frac{\left(\frac{p_N + p_P}{2}\right) - \left(\frac{p_P + p_S}{2}\right)}{\partial y} = \frac{p_N - p_S}{2\partial y} \quad (\text{A-5})$$

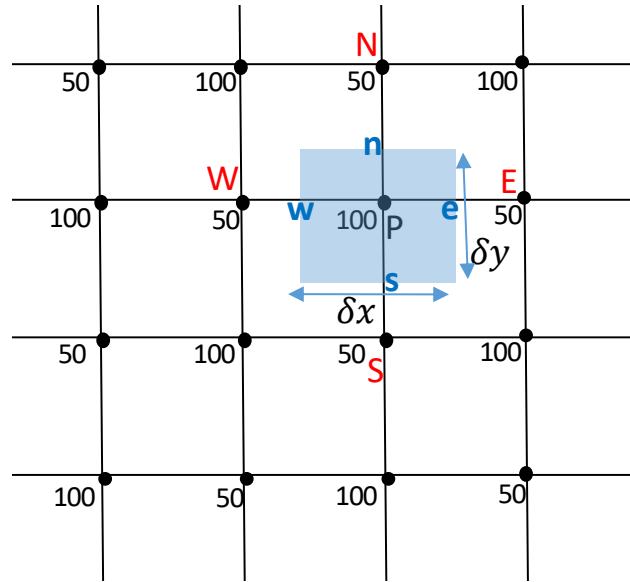


Figure A-1. Checkerboard pressure field

Therefore, the pressure at node P does not appear in pressure gradients, and substituting the values into these equations would result in zero pressure at all nodes and divergence of the solution. Therefore, it can be seen that defining velocities and pressures at the same node would result in infeasible pressure gradient values. One of the efficient solutions for this problem is using a staggered grid for velocity components [70].

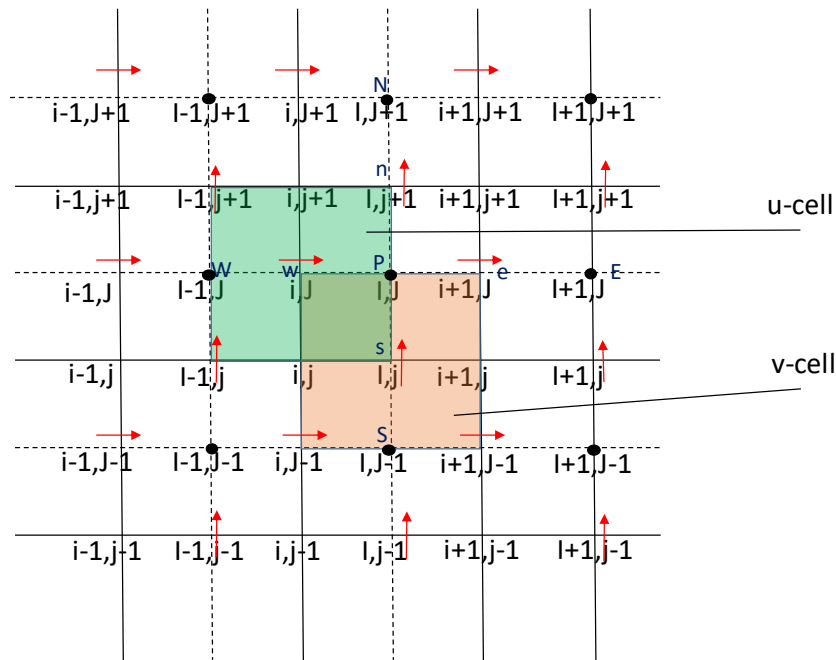


Figure A-2. Staggered grid

Pressure, temperature, and scalar products are stored in nodes marked with solid black circles.  $u$  velocity components are stored where horizontal arrows are located. Similarly,  $v$  velocities are located where vertical arrows are located. In other words, horizontal velocities are stored in  $(i,j)$  nodes. Vertical velocities are stored in  $(I,j)$  nodes, and scalars are stored in  $(I,J)$  nodes. Looking at  $u$ -cell and  $v$ -cell control volumes, we can see that these control volumes are not only different from each other but are different than scalar control volumes. In a staggered grid network, horizontal pressure gradients are calculated based on  $u$ -velocity control volumes, while vertical pressure gradients are calculated based on  $v$ -velocity control volumes. These gradients are shown as follows:

$$\frac{\partial p}{\partial x} = \frac{p_P - p_W}{\delta x_u} \quad (\text{A-6})$$

$$\frac{\partial p}{\partial y} = \frac{p_P - p_S}{\delta y_v} \quad (\text{A-7})$$

Now, if we calculate these pressures for the checker-board example, we can see that the pressure gradients will not be zero anymore and are noticeable values.

To proceed with the SIMPLE algorithm, we need to guess the initial pressure field. To discrete momentum equations, we can either use backward/forward staggered grids. The provided staggered grid is backward since the  $i$  location of horizontal velocity ( $u_{i,j}$ ) is at a distance  $-\frac{1}{2\delta x}$  from node  $(I,J)$ . Discrete momentum equations are in the following form [70]:

$$a_{i,j} u_{i,j}^* = \sum a_{nb} u_{nb}^* + (p_{I-1,J}^* - p_{I,J}^*) A_{i,j} + b_{i,j} \quad (\text{A-8})$$

$$a_{I,j} v_{I,j}^* = \sum a_{nb} v_{nb}^* + (p_{I,J-1}^* - p_{I,J}^*) A_{I,j} + b_{I,j} \quad (\text{A-9})$$

The values for  $a_{i,j}$  and  $a_{I,j}$ , and  $a_{nb}$  are calculated based on the proper differencing methods such as upwind, hybrid, and Quick discretization methods. In our simulation, the hybrid method is used. In order to calculate  $\sum a_{nb} u_{nb}^*$ , we need to calculate F and D values for n,w,e,s as follows:



$$F_w = (\rho u)_w = \frac{F_{i,J} + F_{i-1,J}}{2} \quad (\text{A-10})$$

$$= \frac{1}{2} \left[ \left( \frac{\varphi_{I,J} + \varphi_{I-1,J}}{2} \right) u_{i,J} + \left( \frac{\varphi_{I-1,J} + \varphi_{I-2,J}}{2} \right) u_{i-1,J} \right]$$

$$F_e = (\rho u)_e = \frac{F_{i+1,J} + F_{i,J}}{2} = \frac{1}{2} \left[ \left( \frac{\varphi_{I+1,J} + \varphi_{I,J}}{2} \right) u_{i+1,J} + \left( \frac{\varphi_{I,J} + \varphi_{I-1,J}}{2} \right) u_{i,J} \right] \quad (\text{A-11})$$

$$F_s = (\rho v)_s = \frac{F_{I,j} + F_{I-1,j}}{2} \quad (\text{A-12})$$

$$= \frac{1}{2} \left[ \left( \frac{\varphi_{I,J} + \varphi_{I,J-1}}{2} \right) v_{I,j} + \left( \frac{\varphi_{I-1,J} + \varphi_{I-1,J-1}}{2} \right) v_{I-1,j} \right]$$

$$F_n = (\rho v)_n = \frac{F_{I,j+1} + F_{I-1,j+1}}{2} \quad (\text{A-13})$$

$$= \frac{1}{2} \left[ \left( \frac{\varphi_{I,J+1} + \varphi_{I,J}}{2} \right) v_{I,j+1} + \left( \frac{\varphi_{I-1,J+1} + \varphi_{I-1,J}}{2} \right) v_{I-1,j+1} \right]$$

$$D_w = \frac{\Gamma_{I-1,J}}{(x_i - x_{i-1})} \quad (\text{A-14})$$

$$D_e = \frac{\Gamma_{I,J}}{(x_{i+1} - x_i)} \quad (\text{A-15})$$

$$D_s = \frac{\Gamma_{I-1,J} + \Gamma_{I,J} + \Gamma_{I-1,J-1} + \Gamma_{I,J-1}}{4(y_J - y_{J-1})} \quad (\text{A-16})$$

$$D_n = \frac{\Gamma_{I-1,J+1} + \Gamma_{I,J+1} + \Gamma_{I-1,J} + \Gamma_{I,J}}{4(y_{J+1} - y_J)} \quad (\text{A-17})$$

$$a_w = \max \left[ F_w, \left( D_w + \frac{F_w}{2} \right), 0 \right] \quad (\text{A-18})$$

$$a_e = \max \left[ -F_e, \left( D_e - \frac{F_e}{2} \right), 0 \right] \quad (\text{A-19})$$

$$a_S = \max \left[ F_s, \left( D_s + \frac{F_s}{2} \right), 0 \right] \quad (\text{A-20})$$

$$a_N = \max \left[ -F_n, \left( D_n - \frac{F_n}{2} \right), 0 \right] \quad (\text{A-21})$$

$$a_P = a_W + a_E + a_S + a_N + F_e - F_w + F_n - F_s \quad (\text{A-22})$$

Similarly, F and D values for v control volumes are calculated as follows:

$$\begin{aligned} F_w = (\rho u)_w &= \frac{F_{i,j} + F_{i,j-1}}{2} \\ &= \frac{1}{2} \left[ \left( \frac{\varphi_{i,j} + \varphi_{i,j-1}}{2} \right) u_{i,j} + \left( \frac{\varphi_{i-1,j-1} + \varphi_{i,j-1}}{2} \right) u_{i,j-1} \right] \end{aligned} \quad (\text{A-23})$$

$$\begin{aligned} F_e = (\rho u)_e &= \frac{F_{i+1,j} + F_{i+1,j-1}}{2} \\ &= \frac{1}{2} \left[ \left( \frac{\varphi_{i+1,j} + \varphi_{i,j}}{2} \right) u_{i+1,j} + \left( \frac{\varphi_{i,j-1} + \varphi_{i+1,j-1}}{2} \right) u_{i+1,j-1} \right] \end{aligned} \quad (\text{A-24})$$

$$\begin{aligned} F_s = (\rho v)_s &= \frac{F_{i,j-1} + F_{i,j}}{2} \\ &= \frac{1}{2} \left[ \left( \frac{\varphi_{i,j-1} + \varphi_{i,j-2}}{2} \right) v_{i,j-1} + \left( \frac{\varphi_{i,j} + \varphi_{i,j-1}}{2} \right) v_{i,j} \right] \end{aligned} \quad (\text{A-25})$$

$$F_n = (\rho v)_n = \frac{F_{i,j} + F_{i,j+1}}{2} = \frac{1}{2} \left[ \left( \frac{\varphi_{i,j} + \varphi_{i,j-1}}{2} \right) v_{i,j} + \left( \frac{\varphi_{i,j+1} + \varphi_{i,j}}{2} \right) v_{i,j+1} \right] \quad (\text{A-26})$$

$$D_w = \frac{\Gamma_{i-1,j-1} + \Gamma_{i,j-1} + \Gamma_{i-1,j} + \Gamma_{i,j}}{4(x_i - x_{i-1})} \quad (\text{A-27})$$

$$D_e = \frac{\Gamma_{i,j-1} + \Gamma_{i+1,j-1} + \Gamma_{i,j} + \Gamma_{i+1,j}}{4(x_{i+1} - x_i)} \quad (\text{A-28})$$

$$D_s = \frac{\Gamma_{i,j-1}}{(y_j - y_{j-1})} \quad (\text{A-29})$$

$$D_n = \frac{\Gamma_{I,J}}{(y_{j+1} - y_j)} \quad (\text{A-30})$$

$$a_W = \max \left[ F_W, \left( D_W + \frac{F_W}{2} \right), 0 \right] \quad (\text{A-31})$$

$$a_E = \max \left[ -F_e, \left( D_e - \frac{F_e}{2} \right), 0 \right] \quad (\text{A-32})$$

$$a_S = \max \left[ F_S, \left( D_S + \frac{F_S}{2} \right), 0 \right] \quad (\text{A-33})$$

$$a_N = \max \left[ -F_n, \left( D_n - \frac{F_n}{2} \right), 0 \right] \quad (\text{A-34})$$

$$a_P = a_W + a_E + a_S + a_N + F_e - F_W + F_n - F_S \quad (\text{A-35})$$

After the momentum equation is solved and  $u^*$  and  $v^*$  fields are obtained, new variables will be defined to address the difference between the correct answer and the results obtained based on the guessed pressure fields.

$$p = p^* + p' \quad (\text{A-36})$$

$$u = u^* + u' \quad (\text{A-37})$$

$$v = v^* + v' \quad (\text{A-38})$$

Replacing  $p^*, u^*$ , and  $v^*$  with their equivalent terms in Equations (A-36) – Equation (A-38) and substituting them into discrete momentum equation would result in the following equations:

$$a_{i,j} u'_{i,j} = \sum a_{nb} u'_{nb} + (p'_{I-1,J} - p'_{I,J}) A_{i,j} \quad (\text{A-39})$$

$$a_{i,j} v'_{i,j} = \sum a_{nb} v'_{nb} + (p'_{I,J-1} - p'_{I,J}) A_{i,j} \quad (\text{A-40})$$

To simplify Equation (A-39) and Equation (A-40),  $\sum a_{nb} u'_{nb}$  and  $\sum a_{nb} v'_{nb}$  terms are dropped. The elimination of these terms is the main idea of the SIMPLE algorithm. Therefore, the simplified equations are [70]:

$$u'_{i,j} = d_{i,j}(p'_{l-1,j} - p'_{l,j}) \quad (\text{A-41})$$

$$v'_{l,j} = d_{l,j}(p'_{l,j-1} - p'_{l,j}) \quad (\text{A-42})$$

where  $d_{i,j} = \frac{A_{i,j}}{a_{i,j}}$  and  $d_{l,j} = \frac{A_{l,j}}{a_{l,j}}$ . The corrected velocities could be obtained as follows [70]:

$$u_{i,j} = u_{i,j}^* + u'_{i,j} \quad (\text{A-43})$$

$$v_{l,j} = v_{l,j}^* + v'_{l,j} \quad (\text{A-44})$$

Substituting the modified velocities into discrete continuity equation would result in the following equations:

$$a_{l,j}p'_{l,j} = a_{l+1,j}p'_{l+1,j} + a_{l-1,j}p'_{l-1,j} + a_{l,j+1}p'_{l,j+1} + a_{l,j-1}p'_{l,j-1} + b'_{l,j} \quad (\text{A-45})$$

where

$$a_{l,j} = a_{l+1,j} + a_{l-1,j} + a_{l,j+1} + a_{l,j-1} \quad (\text{A-46})$$

$$a_{l+1,j} = (\varphi Ad)_{l+1,j} \quad (\text{A-47})$$

$$a_{l-1,j} = (\varphi Ad)_{l,j} \quad (\text{A-48})$$

$$a_{l,j+1} = (\varphi Ad)_{l,j+1} \quad (\text{A-49})$$

$$a_{l,j-1} = (\varphi Ad)_{l,j} \quad (\text{A-50})$$

$$b'_{I,J} = (\varphi u^* A)_{i,j} - (\varphi u^* A)_{i+1,j} + (\varphi v^* A)_{i,j} - (\varphi v^* A)_{i,j+1} \quad (\text{A-51})$$

Pressures corrections ( $p'$ ) can be obtained by solving Equation (A-45), and therefore the modified pressure can be obtained by  $p = p^* + p'$ ,  $p$  values tend to diverge if they are not under relaxed. Therefore, pressures and velocities must be relaxed to prevent divergence [70].

$$p^{new} = p^* + \omega_p(p') \quad (\text{A-52})$$

$$u^{new} = \omega_u u + (1 - \omega_u)u^{(n-1)} \quad (\text{A-53})$$

$$v^{new} = \omega_v v + (1 - \omega_v)v^{(n-1)} \quad (\text{A-54})$$

$\omega$  values are under relaxation factors for pressures and velocities.  $u^{(n-1)}$  and  $v^{(n-1)}$  are solutions from the previous step. The under relaxation factors that are used for  $u, v, p$  are 0.8, 0.8, and 0.6, respectively. The general schematic of the SIMPLE finite volume is provided as follows:

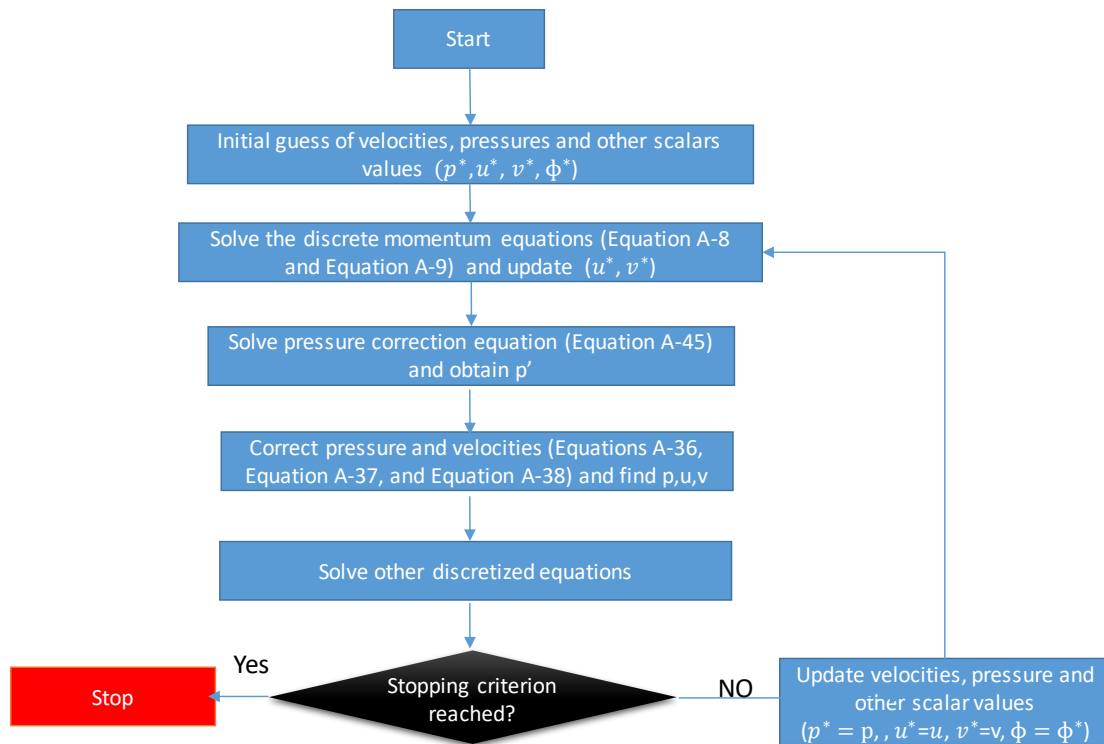


Figure A-3. SIMPLE algorithm flowchart [70]

## Appendix B. GA Algorithm

Genetic algorithm (GA) is a global optimization method inspired by the evolution theory. This theory is first presented by J. Holland in 1975 [83]. GA does not necessarily result in the exact optimal solution; however, evidence has shown that the obtained solutions are acceptable if the simulation is repeated several times. GA efficiency competes with other combinatorial optimization algorithms such as hyper-climbing, simulated annealing, and sequential search methods. GA does not know any information about the search space, and that is the reason that GA is largely used in different optimization problems in various scientific fields.

GA encodes the optimization variables into a string of one of the followings [83]:

- Binary bits
- Characters
- Real numbers

Each bit in the string is called a gene, and a complete set of genes forms a chromosome, string, or individual. Changing genes would result in changing the chromosome, which would result in a new variable in the space. In our problem, genes are catalyst distribution function coefficients, and the whole chromosome represents a non-uniform distribution function. The optimization process starts with the initialization of a specific number of chromosomes, which is called the first generation. Each chromosome is generated through a random process, and the performance of each chromosome is evaluated with the fitness function(s). In this project, fitness functions are the maximum PEMFC power density and minimum oxygen distribution at CCL. The calculation of fitness functions is conducted by the PEMFC CFD model. The optimization process starts by evaluating the first generation so that GA understands how strong each chromosome performs in the solution space.

The next step is to form the next generation. This process starts by selecting parents to mate and produce the next generation. This process is called selection and gives more opportunity to strong chromosomes to be chosen as parents. However, the selection process does not entirely ignore the weak genes to prevent premature convergence. Once

parents are chosen, the new generation is formed based on the crossover of genes, and the new individuals are formed by different combinations of genes. The new generation of children is then evaluated through the fitness function(s). Selection and crossover operators tend to preserve the combination of the parameter values that obtain a better result in the optimization process. However, if the optimization process only relies on these two processes, it might miss some spaces in the solution area. This issue happens when there are not enough parameter values in the previous generation, or the chromosomes are concentrated in a specific part of the solution space. This problem is resolved through the mutation process inspired by biology evolution. In fact, random mutations would help to not get stuck around the local minimum and leads the optimization algorithm towards the global optimal answer. However, it is essential to set the mutation rate to a small number to prevent data loss and not change it to a random search.

Optimization would continue by forming new generations, evaluating chromosomes, selecting parents, and producing the next generation through crossover and mutation operators. It is also suggested to send some of the strong chromosomes in each generation to the next one. This number must be small enough to prevent immature convergence. The general optimization procedure is shown as follows:

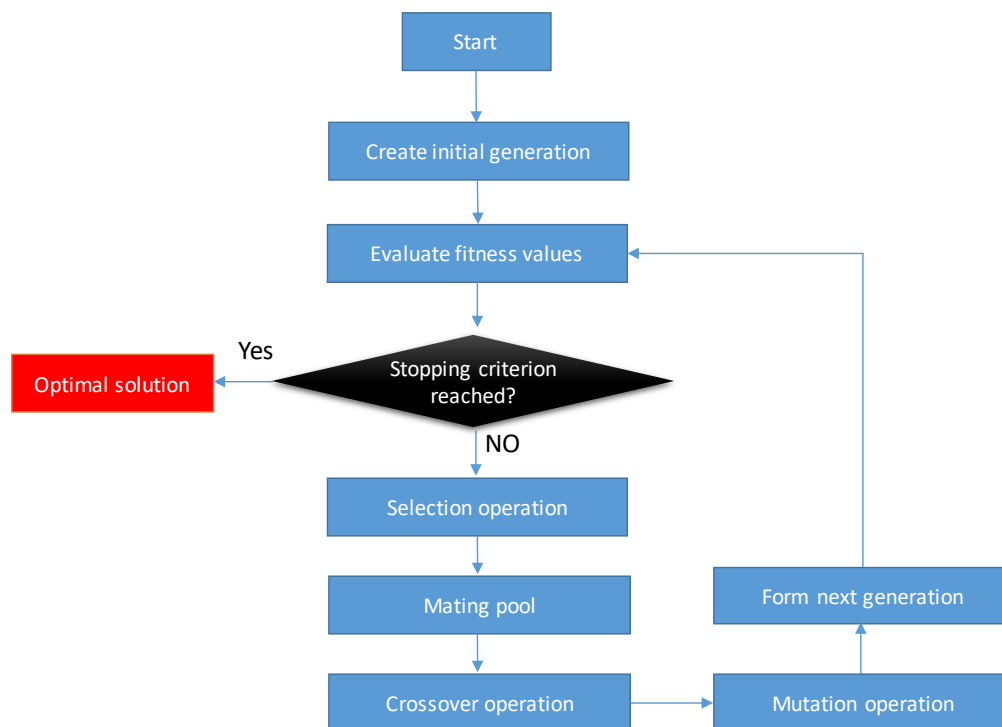


Figure B-1. GA algorithm



## Appendix C. KNN Estimator

KNN algorithm is a very simple ML method that works based on memorizing the training set. The label of any new data is predicted based on its closest neighbors. The primary assumption is that close neighbors own similar labels. KNN is also known as a non-parametric lazy instance-based algorithm that does not explicitly model the data-generating process but directly models the posterior probabilities. The algorithm for this method is provided as follows:

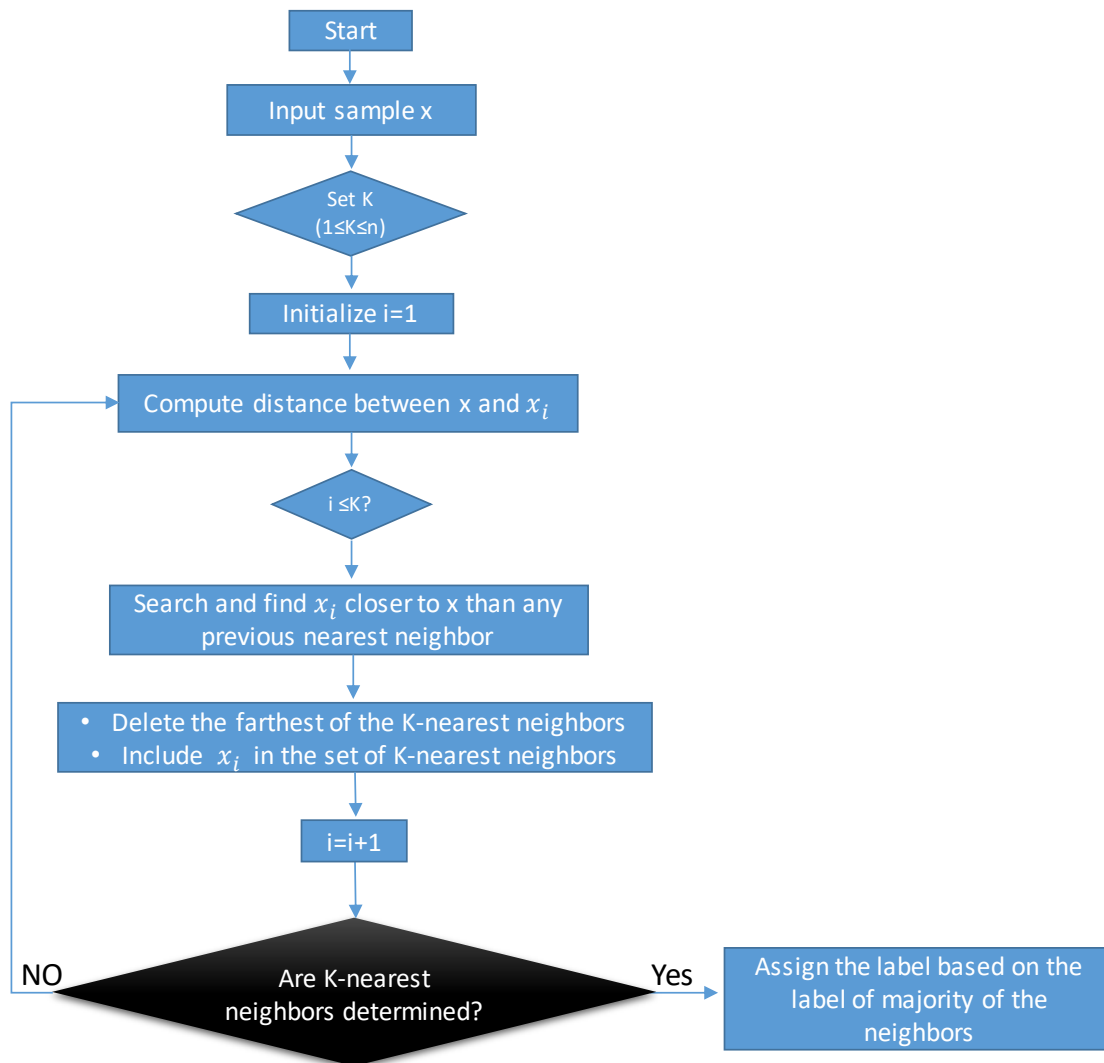


Figure C-1. KNN estimator algorithm

The famous distance metrics in the KNN algorithm is Minkowski and can be obtained from the following equation.

$$d(x^{[a]}, x^{[b]}) = \sum \sqrt[q]{(x_j^{[a]} - x_j^{[b]})^q} \quad (\text{C-1})$$

$x^{[a]}$  is the  $a^{\text{th}}$  data point and  $x^{[b]}$  is the  $b^{\text{th}}$  data point.  $d$  and  $j$  correspond to the distance and feature, respectively. When  $q$  is equal to one ( $q=1$ ), the distance metric is Manhattan distance, and  $q=2$  corresponds to Euclidean distance.

In the classification problem, the label of new data is determined based on the majority of neighbors. For example, in our classification problem, seven neighbors ( $K=7$ ) resulted in the highest accuracy, which means that the seven closest neighbors determine whether PEMFC is leaky or healthy. In the regression problem, the numeric label is calculated by the average of the five nearest neighbors. The problem with the KNN algorithm is the curse of dimensionality. In ML, the curse of dimensionality refers to the presence of high dimensional data and a high range of features in the training examples. In other words, with the high dimensional data, a larger portion of hypervolume must be taken into consideration, and even, in that case, the KNN estimator might not be particularly close to the query point. Therefore, alternatives must be developed to be used in case of the poor performance of the KNN estimator in high dimensional data.

KNN method has a time complexity of  $O(n.m)$ , where  $n$  is the number of training examples, and  $m$  is the number of features in the training set. If  $n \gg m$  (similar in our case), then the algorithm has  $O(n)$  time complexity.

## Appendix D. ANN Estimator

ANNs are derived based on the biological concept of brain cell structures, i.e., neurons. Neurons are connected by synapses that generate electrical signals. When the electrical signals surpass the threshold of neural excitation, the information would be propagated to the other neurons. With the huge number of neurons in the human brain, we can receive information and knowledge, process, and understand them. The neuron structure used in this work is the most common and is shown as follows:

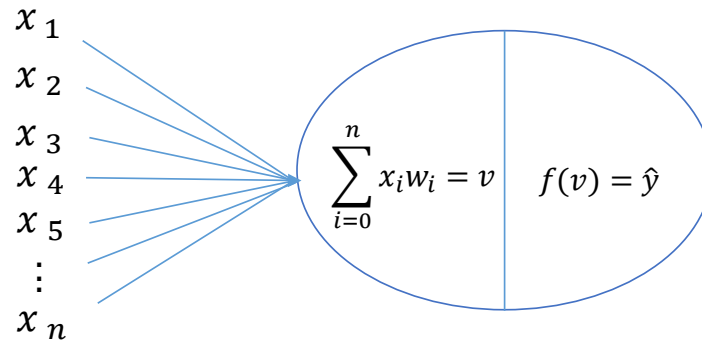


Figure D-1. A neuron structure in feed-forward ANN

Multiple input values ( $x$ ) are multiplied by different weight values ( $w$ ), and the values are summed up and stored in  $v$ .  $v$  is the input value for the activation function ( $f$ ), and the output of the activation function is the neuron outcome ( $\hat{y}$ ). There are four famous activation functions: sigmoid, tanh, reLU, and linear. The equations for these activation functions are provided in Figure D-2. The sigmoid function is mainly used in the output neurons for classification purposes since it generates the probability of different classes. On the other hand, ReLU is used when the output is numeric and positive. A detailed explanation of different activation functions can be found in [84].

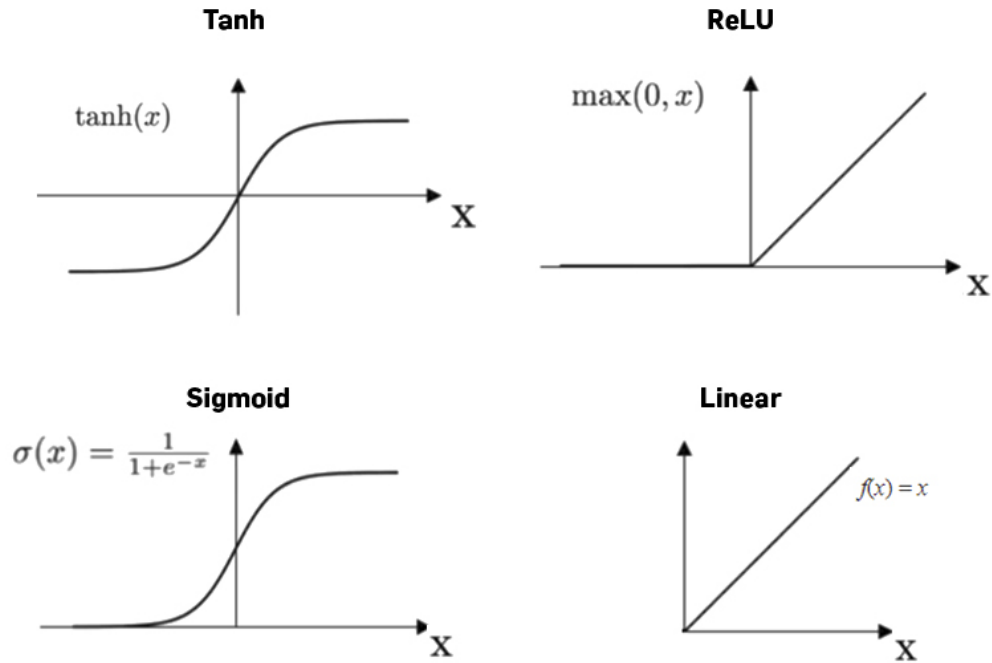


Figure D-2. Different activation functions for neurons

In this work, we used feed-forward neural networks to obtain the desired information. As the name indicates, the information flows through the model to calculate the loss function. The loss function measures the difference between the real outcomes and the predicted outcomes. We used cross-entropy and MSE to calculate the cost (loss) function for the binary and numeric estimators. The equations for these cost functions are listed in Table D-1. A detailed explanation of different cost functions can be found in [84].

Table D-1. Cost function definitions

Cost function	Equation
cross-entropy	$J(y, \hat{y}) = - \sum_{i=1} y_i \log(\hat{y}_i) + (1 - y_i) \log(1 - \hat{y}_i)$
MSE	$J(y, \hat{y}) = \frac{1}{N} \sum_{i=1}^N  (y_i - \hat{y}_i)^2 $

The loss function is the prediction error that must be minimized. An example of a feed-forward neural network is provided in Figure D-3.

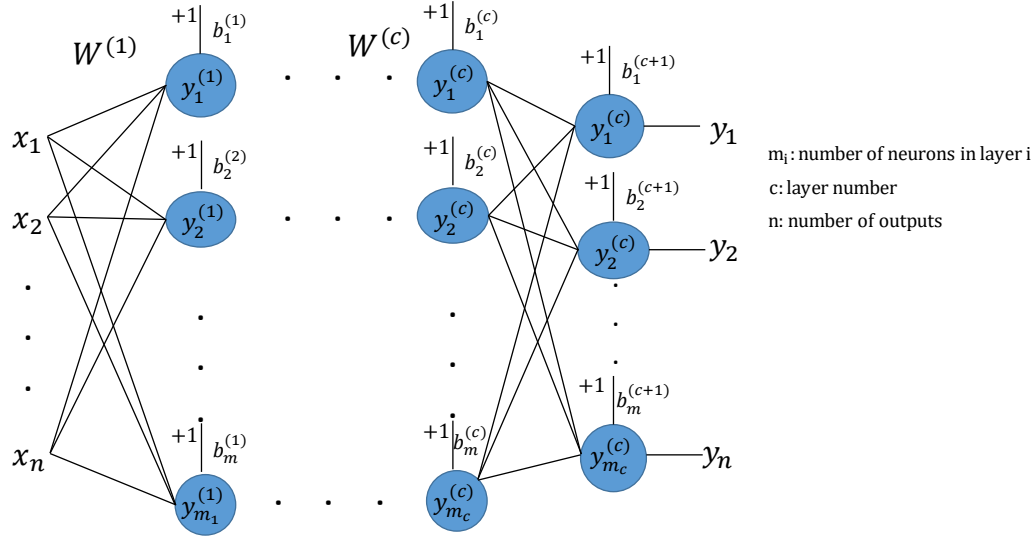


Figure D-3. Schematic of a feedforward ANN

In a feed-forward algorithm, information flows from input to the output. The initial weight and bias values are initialized, and the output predicted values are calculated. Once the output values are calculated, the cost function would be calculated. In the ideal case, the cost function must be equal to zero, which is equivalent to the case that all the estimations are correct. Therefore, the values of weights and biases must be tuned to minimize the cost function. This step requires the calculation of the derivative of the cost function with respect to the model parameters, including weights. This process is done based on the chain rule and is called backpropagation. The intensive mathematical background for the backpropagation process is provided in [85]. Once all the derivatives are calculated the weight values could be changed based on the optimizer. “Batch Gradient Descent”, “Stochastic Gradient Descent”, “Gradient Descent”, and other optimization methods are proposed for this purpose. However, the most famous optimizer used for this purpose is “Adam optimizer”, which computes the adaptive learning rates for each parameter. Adam optimizer tracks the exponentially decaying average of past gradients as well as their squared values. The former one is called the first moment ( $m_t$ ) and the latter one is called the second moment ( $v_t$ ).

$$m_t = \beta_1 m_{t-1} + (1 - \beta_1) g_t \quad (D-1)$$

$$v_t = \beta_2 v_{t-1} + (1 - \beta_2) g_t^2$$

$\beta_1$  and  $\beta_2$  are arbitrary numbers and are usually taken as 0.9 and 0.999. Since the calculation of  $m_t$  and  $v_t$  requires information about the previous iteration, they are initialized as 0 in the first iteration. Therefore, at the early steps of the algorithm are, these two momentums are biased toward zero. Thus the following corrections are conducted to remove the bias.

$$\hat{m}_t = \frac{m_t}{1 - \beta_1} \quad (D-2)$$

$$\hat{v}_t = \frac{v_t}{1 - \beta_2} \quad (D-3)$$

Eventually, the model parameters ( $\theta$ ) are updated as follows:

$$\theta_{t+1} = \theta_t - \frac{\lambda \hat{m}_t}{\sqrt{\hat{v}_t} + \varepsilon} \quad (D-4)$$

$\lambda$  is the learning rate and is usually taken as a small value (0.01 or 0.001).  $\varepsilon$  is a constant and is equal to  $10^{-8}$ . Figure D-4 shows the algorithm for Adam optimizer. It is necessary to mention that it is possible to use only a portion of the training dataset to calculate the cost function. This is extremely important when the amount of data is very high, and the computational cost is expensive. Using a subset of the training dataset would result in lower computational cost and a quicker convergence. However, a very small batch size might result in the instability of cost function and its gradient.

Keras library with TensorFlow backend provides a simple implementation of feed-forward neural networks with several layers and different optimizers. Our ANN classifier structure graph is visualized by the Tensorboard library and is provided in Figure D-5 to Figure D-9. The ANN regressor has a similar structure with MSE as a cost function.

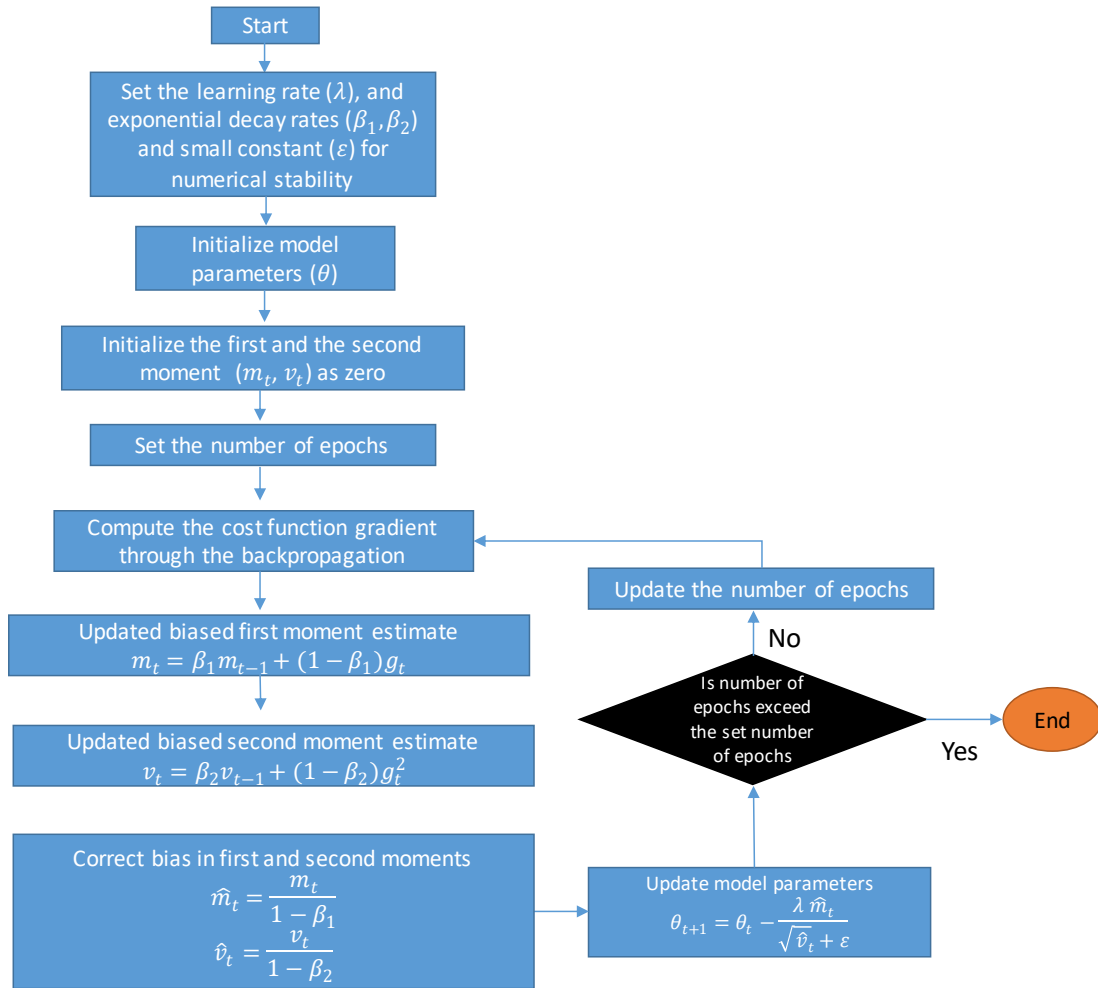


Figure D-4. Adam optimizer algorithm

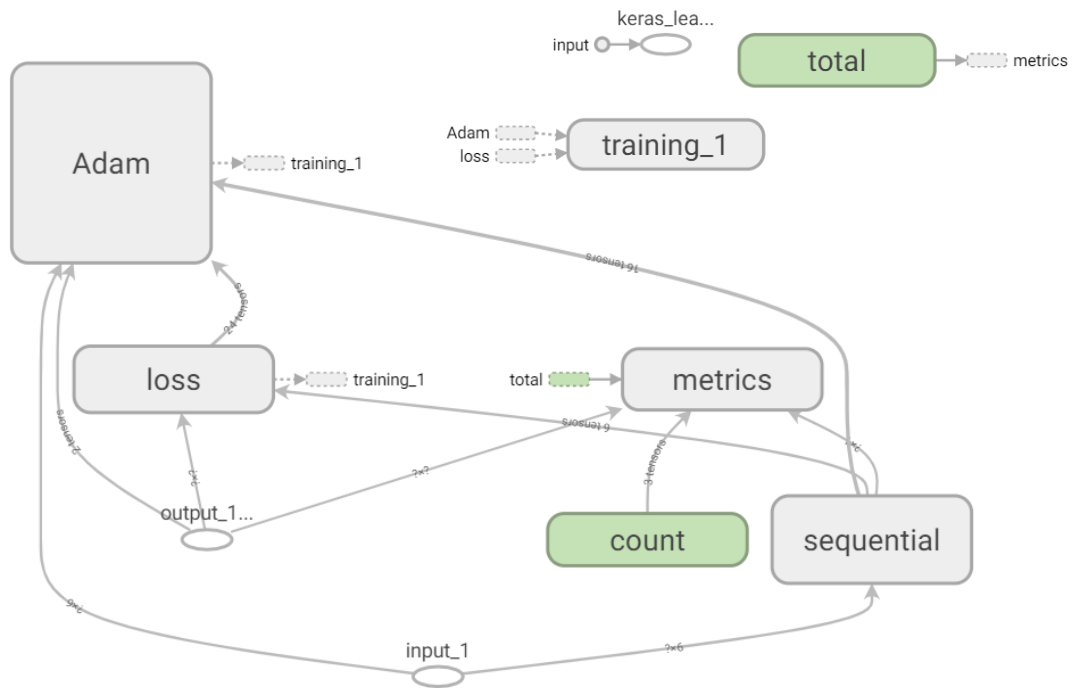


Figure D-5. General graph for ANN classification graph

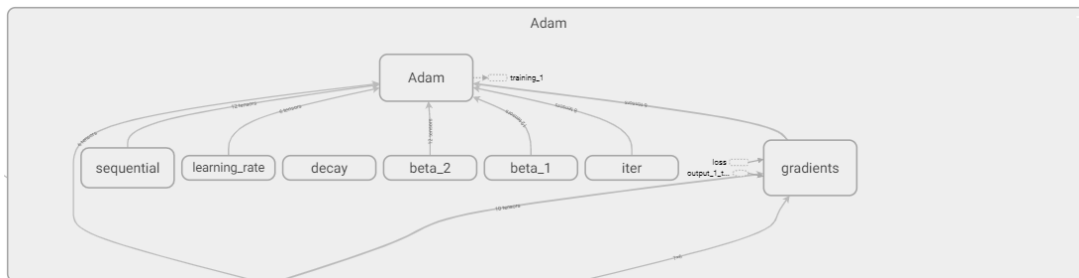


Figure D-6. Adam optimizer structure



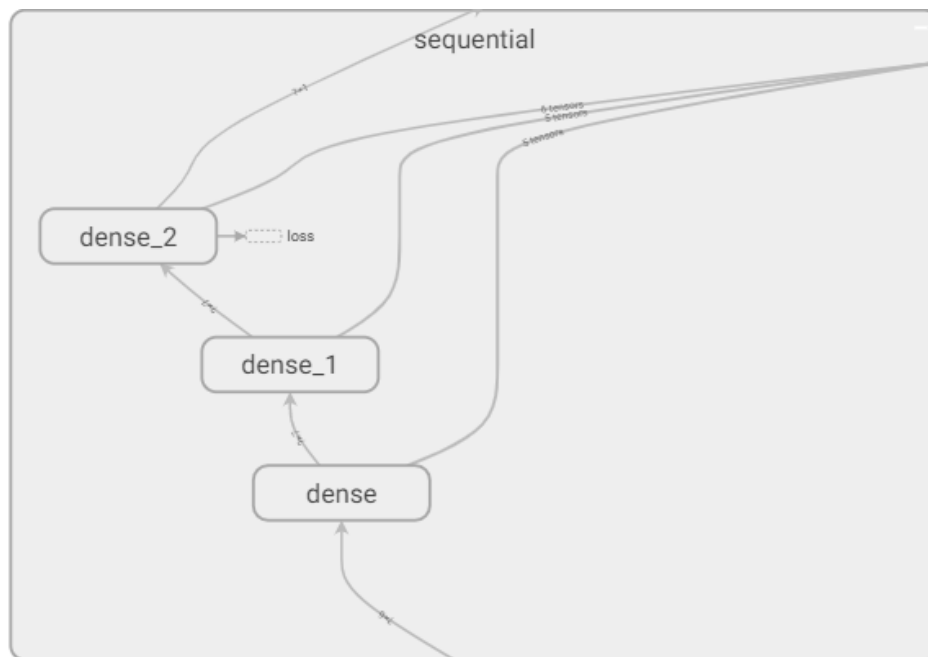


Figure D-7. Structure of Sequential layers



Figure D-8. Loss calculation graph

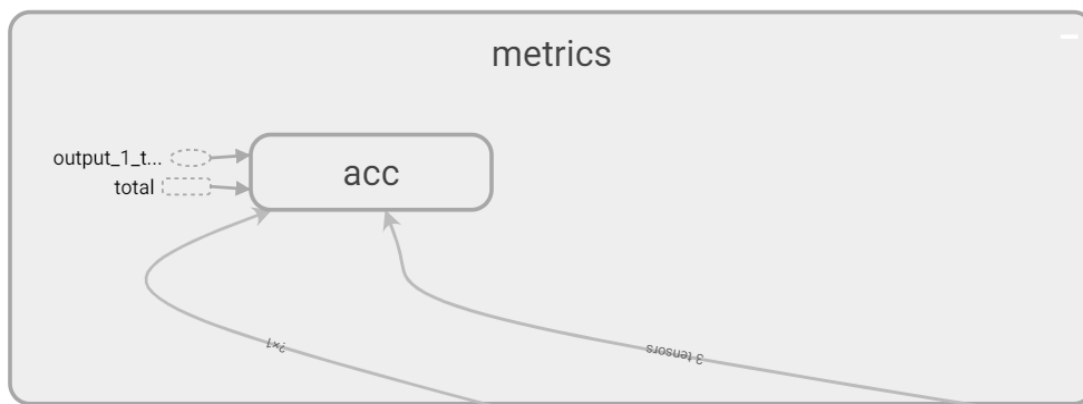


Figure D-9. Metric calculation graph

## Appendix E. Classifier and Regressor Performance Indexes

The performance of classifiers in ML is mainly evaluated based on a confusion matrix. Let's assume that there are two classes of information. We distinguish these classes by labeling them as positive and negative classes. The confusion matrix for such a simple two-class (binary) problem is shown in Figure E-1.

		Predicted class	
		+	-
Actual class	+	True positive (TP)	False negative (FN)
	-	False positive (FP)	True negative (TN)

Figure E-1. Confusion matrix for a binary class

The elements in the confusion matrix are listed as follows [86]:

- True positives (TP): The number of data points that correctly labeled as the positive class
- True negatives (TN): The number of data points that correctly labeled as the negative class
- False positive (FP): The number of data points that incorrectly labeled as the positive class
- False negative (FN): The number of data points that incorrectly labeled as the negative class

The performance indexes are defined as follows [86]:

- $Accuracy = \frac{TP+TN}{TP+FP+FN+TN}$ , Accuracy is the proportion of total correct predictions and represents the overall performance of the classifier.
- Recall / True positive rate =  $\frac{TP}{TP+FN}$ , Recall measures the fraction of positive examples that the classifier can capture. The recall index is important in cases that

capturing one class is extremely important. As an example, we can refer to data for healthy and cancerous cells.

- *True negative rate* =  $\frac{TN}{TN+FP}$ , This index measures the fraction of negative examples that the classifier can capture.
- *Precision* =  $\frac{TP}{TP+FP}$ , Precision is a proportion of the records that were positive from the group that the classifier predicted to be positive
- *F<sub>1</sub> score* =  $\frac{2precision \cdot recall}{precision+recall}$ , F1-score is a measure that evaluates the performance of classifiers based on both precision and recall criteria.

Performance of regressors are obtained based on the following performance indexes [86]:

- $MSE = \frac{1}{N} \sum_{i=1}^N |(y_i - \hat{y}_i)^2|$ , where N is the number of samples,  $y_i$  is the exact value and  $\hat{y}$  is the predicted value.
- $MAE = \frac{1}{N} \sum_{i=1}^N |(y_i - \hat{y}_i)|$
- $R^2 \text{ score} = 1 - \frac{\sum_{i=1}^N |(y_i - \hat{y}_i)^2|}{\sum_{i=1}^N |(y_i - \bar{y})^2|}$ , where  $\bar{y}$  is the mean value of y samples.